ALUMINATE SPINELS FOR USE AS CATALYST ENHANCEMENT OF SOLID OXIDE FUEL CELLS

by

Marley Sarria Zachariasen

A thesis submitted in partial fulfillment
of the requirements for the degree

of

Master of Science

in

Mechanical Engineering

MONTANA STATE UNIVERSITY
Bozeman, Montana

November 2019

c COPYRIGHT

by

Marley Sarria Zachariasen

2019

All Rights Reserved

DEDICATION

I dedicate this work to my friends and family who have accompanied and supported me during this long and arduous journey. There were many who embarked by my side, and many more joined along the way. You celebrated with me during the best of times, and lifted me out of the darkest pits. Always there to lend a hand on a rainy day. Ever present to force this poor shirker forward. Without you I would still be watching the clouds. Without you this work would be nothing but a pipe dream.

ACKNOWLEDGEMENTS

I would like to acknowledge all of the people who have assisted in elevating this research to the level it is at today. My advisor, Dr. Stephen Sofie, provided his knowledge every step of the way. His experience directed me towards my goals, while his wisdom focused my ambition into the work that is presented herein. My predecessors, Dr. Clay Hunt and Dr. David Driscoll, who laid the foundational concepts and methods upon which my work is built. My colleagues in the conductive materials laboratory, ever available for assistance and brainstorming. Particular thanks should be given to John Kent, Kyle Allemeier, Nate Johnson, and Stephen Heywood. My collaborators in the Chemistry Department, Dr. Robert Walker and Märtha Welander, who allowed me the privilege of assisting with their research and granting me the honor of co-authorship on their papers. My committee members, Dr. Ryan Anderson and Dr. Stephan Warnat, who endured my scientific ramblings and unanswered questions. The administrators and members of the ICAL division of the Montana Nanotechnology Facility for their assistance in the collection of many of the chemical analyses and images presented within this work. Finally, the members of the Department of Energy who assisted in funding this research under award numbers DE-FE0031125 and DE-FE0026192.

TABLE OF CONTENTS

1. INTRODUCTION 1

2. BACKGROUND 4

2.1 Fuel Cell Technology 4
History 5
Types and Applications 6
Electrochemistry 9
2.2 Solid Oxide Fuel Cells 15
Operation and Design 15
Materials 19
Anode Resiliency 29
2.3 Aluminum Titanate 36
2.4 Aluminate Spinels 40

3. MOTIVATION 42

4. EXPERIMENTAL METHODS 44

4.1 Materials 44
Ceramic Powders 44
Metallic Salts 44
Surfactants 45
Binders and Plasticizers 45
Solvents 45
4.2 Fuel Cell Manufacturing 46
Electrode Processing 46
Infiltration 49
4.3 Fuel Cell Testing 50
Performance 52
Degradation 52
4.4 Fracture Resistance Measurement 53
Sample Preparation 53
Microhardness Testing 54
4.5 Aluminate Spinel Synthesis and Characterization 54
Synthesis 54
Characterization 55

TABLE OF CONTENTS – CONTINUED

5. RESULTS AND DISCUSSION 57

5.1 NiO/GDC Anode System 57
Hardness and Fracture Resistance 57
Electrochemistry 60
FESEM 69
5.2 Aluminate Spinel Materials 74
Synthesis 75
Reduction 81

6. CONCLUSION 87

6.1 Pertinent Results 87
Future Directions 89

REFERENCES CITED 90

LIST OF TABLES

Table Page

5.1 Average values for Vicker's hardness, crack length and K_{ifr} for ALT and Alumina doped NiO/GDC anode precursor materials. 57

LIST OF FIGURES

Figure Page

1.1 Scanning Electron Microscopy image of Cermet anode with regions identified. 2

2.1 Schematic of the basic operation of a proton exchange membrane fuel cell. 10

2.2 Relationship between OCV and operating temperature for several common fuel cell constructions 12

2.3 General polarization curve for an electrochemical device with primary regions of loss labeled 13

2.4 Schematic of the basic operation of a solid oxide fuel cell. 16

2.5 Various common constructions of fuel cells. 17

2.6 Rough schematic of the anodic triple phase boundary. 18

2.7 Common stack configurations for A) planar SOFCs, and B) tubular SOFCs. 18

2.8 Stack components for tubular and planar SOFC stacks 19

2.9 Material requirements for each of the three SOFC components 19

2.10 Unit cell of the ABO_3 perovskite structure 21

2.11 Ionic conductivities of commonly used electrolyte materials 22

2.12 Effects of alloying zirconia with stabilizing oxides resulting in the formation of oxygen vacancies. 24

2.13 Schematic diagram of a more complex SOFC system including steam reforming. 27

2.14 Rough schematic of MIEC anode materials. 29

2.15 A cracked member and its associated plastic deformation zone. 31

2.16 Two tables representing data reported for the mechanical properties of NiO/YSZ anode materials 32

2.17 Results of indentation fracture resistance studies on NiO/YSZ anode materials. 34

LIST OF FIGURES – CONTINUED

Figure Page

2.18 SOFC degradation mechanism scheme 35

2.19 Side by side images of a reduced Ni/YSZ cermet before and after annealing 36

2.20 Damage to nickel metal foam caused by exposure to H_2S 37

2.21 Schematic of diffusion caging mechanism with AFM overlay 39

2.22 Atomic structure of an aluminate spinel 41

4.1 Block diagram of the possible electrode processing methods 48

4.2 Schematic of components used for fuel cell testing 51

5.1 Statistical distributions of K_{ifr} 59

5.2 Degradation of 2, 4, and 10 w% ALT doped Ni/GDC anode SOFCs 60

5.3 Degradation of 1, 2, and 5 w% alumina doped Ni/GDC anode SOFCs 62

5.4 Degradation of 10, 15, and 20 w% alumina doped Ni/GDC anode SOFCs 62

5.5 Power density and current density curves for 2, 4, and 10 w% ALT doped Ni/GDC anode SOFCs 63

5.6 Power density and current density curves for 2, 4, and 10 w% ALT doped Ni/GDC anode SOFCs 65

5.7 Power density and current density curves for 1, 2, and 5 w% alumina doped Ni/GDC anode SOFCs 66

5.8 Power density and current density curves for 10, 15, and 20 w% alumina doped Ni/GDC anode SOFCs 67

5.9 Schematic representations of the hypothesized deleterious mechanisms associated with ALT and alumina doping of Ni/GDC anodes. 68

5.10 FESEM images of Ni/GDC anodes without dopant before and after operation 70

LIST OF FIGURES – CONTINUED

Figure Page

5.11 FESEM images of various microstructural differences associated with ALT and alumina doping 72

5.12 FESEM images of various microstructural differences associated with high concentration alumina doping 73

5.13 Cobalt aluminate powders formed at various treatment temperatures 76

5.14 Copper aluminate powders formed at various treatment temperatures 77

5.15 Powder XRD diffraction pattern for solid-state synthesized copper aluminate 78

5.16 Powder XRD diffraction pattern for co-precipitate synthesized copper aluminate 79

5.17 Powder XRD diffraction pattern for solid-state synthesized cobalt aluminate 80

5.18 Powder XRD diffraction pattern for co-precipitate synthesized cobalt aluminate 81

5.19 Cobalt based sample pellets before and after reduction 82

5.20 Copper based sample pellets before and after reduction 83

5.21 Micrographs of the fracture surface of a reduced copper aluminate sample 85

5.22 Fractured surface of a sintered copper aluminate after reduction 86

ABSTRACT

The growing necessity to find clean, efficient power sources has led to the advancement of technology in various fields of renewable energy. The field of electrochemical energy conversion, better known has Hydrogen Fuel Cell energy, has shown promise in replacing fossil fuels. This technology is fuel flexible, emits no harmful products, and generates power at efficiencies double or triple that of the Carnot combustion cycle widely used in automotive propulsion and large scale combustion power generation. However, the power production is limited by the short life expectancy of the components used to convert the chemical energy of the fuel into an electrical current. Two mechanisms work simultaneously during fuel cell operation to degrade the anodic electrode of the cell. The coarsening of the catalyst metal particles reduces the total active area of the anode while contaminants from the fuel deposit on the anodes remaining active areas, blocking fuel from the locations where the reaction takes place.

Recent studies have shown that doping the industry standard fuel cell anode, Ni/YSZ, with a compound known as Aluminum Titanate (ALT) increases the overall resiliency of the cell. When heat-treated, ALT disassociates in to aluminum and titanium oxides which are then able to go into solution with the material components of the anode. These new secondary phases were shown to increase the strength and overall power output of the cell while decreasing the rate at which the catalyst coarsens. The electrochemical enhancements were attributed to the aluminum based secondary phase, known as nickel aluminate, a spinel structured compound which undergoes unusual reduction and catalytic transport kinetics.

This work assesses the viability of transferring these enhancement effects to various other cermet anode systems by individually exchanging the ceramic ion conductor and metal electrocatalyst. The electrochemical performance and degradation, as well as mechanical properties, were evaluated for Ni/GDC anodes doped with ALT and alumina. In addition, synthesis and reduction behavior of cobalt and copper aluminate spinels were analyzed for similarities with nickel aluminate.

1

INTRODUCTION

As society reduces dependence on fossil fuels and petroleum-based products for power generation, renewable energy technologies must advance at an increased rate in order to maintain the capacities currently supplied by coal and gas. Solid Oxide fuel cells (SOFCs), a technology involving the electrochemical energy conversion of hydrogen-based fuels, have shown promise in the production of large scale grid power. The technology is largely limited by the resiliency of the materials needed to complete the reactions. Current cell constructions utilize a metal catalyst in conjunction with a ceramic ion conductor to form a ceramic-metal composite (Cermet) for use as the reaction site. The junction of these two components, when exposed to the supplied fuel, forms the active area of the anode, known as the Triple Phase Boundary (TPB) as shown in figure 1.1. These cermets are prone to degradation in two ways. Electrochemically, the metal catalysts have the propensity to agglomerate by a mechanism known as Ostwald Ripening, reducing the active area of the cell and interrupting the flow of electrons. In addition, the breakdown of impure and carbonaceous fuels leads to the deposit of carbon and sulfur at the active sites, blocking fuel transport and inhibiting further catalysis. Mechanically, the brittle nature of the ceramic materials often results in the formation of cracks and the eventual fracture of the cell. This is particularly evident while the metal catalyst is still in its oxide precursor phase, prior to reduction during operation.

Significant progress has been achieved in finding alternative materials for use in SOFC anodes, however, for effective implementation, their processing capabilities and compatibility with other components must be evaluated. Dispersive properties

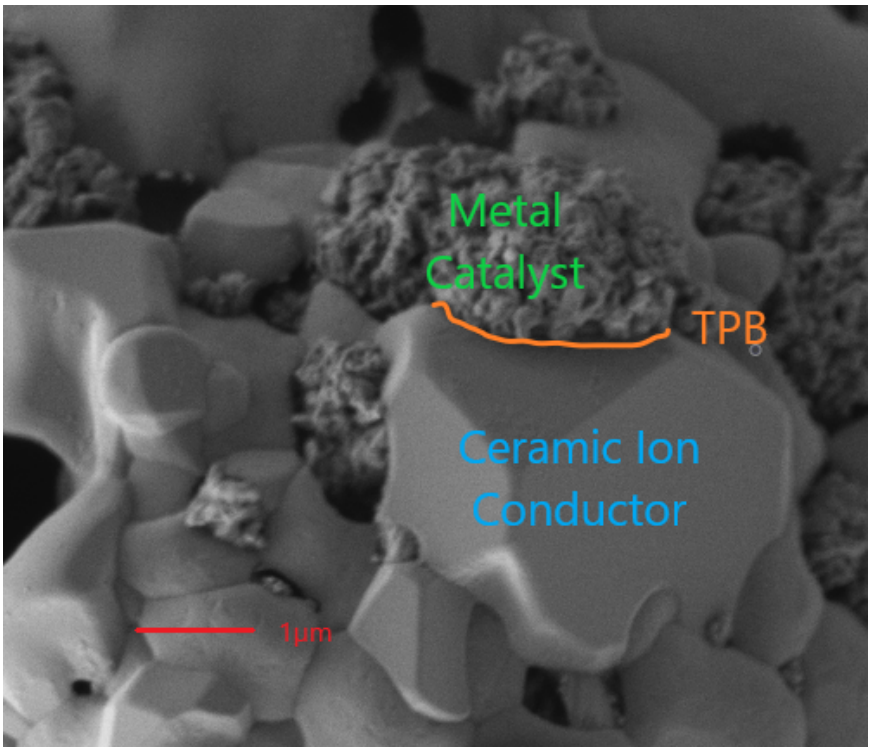


Figure 1.1: Scanning Electron Microscopy image of Cermet anode with regions identified.

(i.e. solubility, viscosity, and surface tension) of the material in suspension can establish the relevance of solution-based processing methods such as airbrushing, slip casting, or screen printing already in use throughout the SOFC industry. If there are issues with industry-standard processes, new methods would be required. With completed anodes, heat treatment parameters must be determined to effectively coalesce the material and adhere it to the electrolyte. This may include treatment under an inert or reducing atmosphere or specific ramp rates and dwells to facilitate off-gassing. These sintering parameters must be carefully chosen to avoid deleterious chemical interactions between the constituents of the co-processed components. In addition, these new materials may not be compatible with existing electrolyte materials purely because of thermal expansion mismatch. Overall, the approach to

developing a new anode material expands far beyond simply producing a material with the necessary characteristics.

Therefore, the most practical and inexpensive method of producing viable SOFC technology is to improve upon the nickel-based cermet anodes that have already become the industry standard. Recent studies have shown that including small concentrations of aluminum oxide and titanium oxide improved the mechanical properties and thermal stability of Nickel/yttrium-stabilized zirconia (YSZ) cermet anodes [1–9]. Enhancements due to dopant oxides were shown to improve despite oxidation and reduction cycling and mitigates possible poisoning due to impurities found in carbonaceous fuels [4, 7–9]. In order to fully investigate the effects these dopant compounds have on SOFC operation, they must be implemented in various anode systems. This will determine compatibility with commonly used anode and electrolyte materials, as well as narrow down the exact mechanisms by which these enhancements occur.

The primary functional modifier involved with the various enhancements discussed above is believed to be a result of the formation of a secondary phase from the alumina dopant and the nickel oxide catalyst precursor of the anode. This combination results in a spinel structured oxide known as nickel aluminate and has been directly associated with the mitigation of various degradation mechanisms in the anode during operation. The experimentation reported herein hopes to elucidate the mechanisms by which this material affects anode resiliency and investigate the aluminate spinel oxides that appear to possess interesting thermal and catalytic properties.

4

BACKGROUND

Fuel Cell Technology

A fuel cell is any device that utilizes a series of chemical reactions to produce a current without the use of moving parts or combustion. Without the need for combustion, the energy generated by these devices is not limited by the gradient between a hot and cold temperature reservoir, as the Carnot cycle dictates. This and the lack of friction associated with moving parts allows fuel cells to achieve efficiencies 3 or 4 times those of the most efficient combustion engines. The governing equations for these efficiencies are detailed in equation (2.1).

$$\eta_{Carnot} = \frac{1 - T_{Cold}}{T_{Hot}}$$
$$\eta_{EChem} = \frac{\Delta G}{\Delta T} \tag{2.1}$$

Batteries also fall under this definition, however, the inherent difference lies in the use of external fuel to fulfill the required chemical reactions. Fuel cells utilize hydrogen or hydrogen-rich compounds such as hydrocarbons and an oxidant, usually air, while batteries contain all required components for the reactions within their enclosure. In general, fuel cells share a common construction: two electrodes, the anode and the cathode, are separated by a permeable electrolyte. The electrodes are primarily made from electronically conducting metals (e.g. platinum, nickel, iron, etc.) while the electrolyte material largely depends on the type of fuel cell. In some cases, this is an acidic solution in which the two electrodes are submerged, other times it may be a ceramic or polymer membrane. The dependence relies on the ion that must be conducted. This chapter discusses the origins of this technology, common types of

fuel cells and their applications, and the general operation of fuel cells. Solid oxide fuel cells (SOFCs) will be discussed in great depth in section 2.2.

History

The first mention of a device resembling an electrochemical fuel cell appears in 1839 by Ser William Grove. Grove discovered that when a dilute solution of sulfuric acid was suspended between an iron plate and a copper plate, each separated by porous porcelain plates of the same size and shape, a noticeable shock was experienced [10]. Across a series of several papers he wrote to the London and Edinborough Journal of Science, Grove detailed his observations of the use of various materials for both the metallic plates and the electrolyte solution in what he came to call a gaseous voltaic battery [11–13]. After Grove, the technology sat for nearly a century before the English engineer, Francis Thomas Bacon, utilized the concept to develop the Alkaline Fuel Cell (AFC) in 1932. This design, utilizing a dissolved alkaline solution in place of an acid, was later commandeered by NASA scientists in the 1960s to supply electricity and drinking water for their spacecraft [14]. About the same time, General Electric scientists were experimenting with polymer electrolytes to create the first Proton Exchange Membrane Fuel Cells (PEMFCs), later becoming the first commercially produced fuel cell technology. Since then, manufacturers have been attempting to implement fuel cell technologies into transportation and agricultural vehicles, and are currently being used to generate power for small areas of the electrical grid.

Between the time when Grove developed his gaseous voltaic batteries and when Bacon built his first AFC, Walther Nernst was investigating a series of solid-state electrolytes made of ceramic materials. His discovery of the transport of oxygen ions through these ceramic materials formed the basis for SOFC electrolytes used

today. Nernst's research was picked up in the 1930s by Swiss researcher Emile Baur who developed his first SOFC using many of the materials used in current SOFC production, but with little success [14, 15]. In the decades following, the technology passed into the hands of many researchers of various nationalities and even now research is continuing towards the hope for a sustainable energy source.

Types and Applications

A plethora of fuel cell constructions exist, each with their own specific set of electrode and electrolyte materials, operating conditions, and associated applications. Several of the most common fuel cell constructions are discussed below (with the exception of SOFCs which will be discussed in greater detail in the following section).

Alkaline Fuel Cells One of the first fuel cell technologies to be used in practical application, AFCs are capable of producing competitive current densities at low operating temperatures (between ambient and 150 °C). Like other fuel cell technologies, AFCs operate by a redox reaction between hydrogen and oxygen, as shown in the half-reactions described by equation (2.2). Hydrogen supplied through the anode reacts with the aqueous potassium hydroxide electrolyte to produce electrons and form water. The electrons pass through an external load and into the cathode where they assist in reducing oxygen to replenish the electrolyte hydroxide ions. The potassium in the electrolyte is used purely as a carrier for these hydroxide ions.

$$\begin{aligned} \text{Anode:} \quad & 2\ H_2 + 4\ OH^- \longrightarrow 4\ H_2O + 4\ e^- \\ \text{Cathode:} \quad & O_2 + 2\ H_2O + 4\ e^- \longrightarrow 4\ OH^- \\ \text{Overall:} \quad & 2\ H_2 + O_2 \longrightarrow 2\ H_2O + \text{electric energy} + \text{heat} \end{aligned} \tag{2.2}$$

The electrodes consist of a catalytic active layer and a hydrophobic layer used to prevent electrolyte solution leakage. Both layers are made of a mixture of carbon black, catalyst (Ni, Ag, Pt, etc.), and PTFE, however, the active layer is more heavily concentrated with catalyst and carbon black, while the hydrophobic layer is primarily PTFE [16]. To further enhance the electronic conductivity, this double layer is pressed onto a nickel metal mesh. Most notably, AFCs have been used by NASA to produce power and drinking water for use in the Apollo and Gemini missions as well as on the ISS.

Phosphoric Acid Fuel Cells Phosphoric Acid Fuel Cells (PAFCs) are most akin to the devices that Grove experimented with during the mid-1800s. Today's PAFC technology utilizes electrodes of a platinum catalyst supported on a carbon or graphite substrate and backed with PTFE. Phosphoric acid suspended in a silicon carbide matrix is used as the electrolyte and connected to the two electrodes. To maximize the

$$\begin{aligned} \text{Anode:} \quad & 2\ H_2 \longrightarrow 4H^+ + 4e^- \\ \text{Cathode:} \quad & 2\ O_2 + 4H^+ + 4\ e^- \longrightarrow 2\ H_2O \\ \text{Overall:} \quad & 4\ H_2 + 2\ O_2 \longrightarrow 2\ H_2O + \text{electric energy} + \text{heat} \end{aligned} \tag{2.3}$$

conductance of the phosphoric acid while minimizing the degradation of the cell, an operating temperature between 150 and 200°C is used [17]. These types of fuel cells are used primarily for stationary applications such as large scale or remote power generation but have also been employed to power a fleet of buses for transit in and around Georgetown University [18].

Molten Carbonate Fuel Cells One of the more recently developed fuel cell technologies, Molten Carbonate fuel cells (MCFCs) utilize a combination of alkali

metal carbonates as the electrolyte material. Operating between 600 and 700°C, the carbonate ions act as the primary charge carrier between the electrodes. Differing heavily from other types of fuel cells, MCFCs operate with practically any hydrogen based fuels (including fossil fuels) at the anode and a combination of oxygen and carbon dioxide at the cathode. The flows of these gases, and by affiliation the operation of the cell, depends greatly on the capillary pressure within the pores of the electrodes.

$$\begin{aligned} \text{Anode:} \quad & 2\ H_2 + 2\ CO_3^{2-} \longrightarrow 2\ H_2O + 2\ CO_2 + 4\ e^- \\ \text{Cathode:} \quad & O_2 + 2\ CO_2 + 4\ e^- \longrightarrow 2\ CO_3^{2-} \\ \text{Overall:} \quad & 2\ H_2 + O_2 \longrightarrow 2\ H_2O + \text{electric energy} + \text{heat} \end{aligned} \tag{2.4}$$

While many combinations of carbonates have been investigated for use as an electrolyte, the most effective combination seems to be of Li/Na carbonates. The most common cathode constructions all utilize nickel oxide due to its conductive nature, however, its propensity to dissolve in the lithium carbonate solution has necessitated the development of more advanced material combinations [19]. On the other hand, the anode is primarily made of nickel metal, however, its tendency to agglomerate due to a phenomenon called Ostwald ripening is forcing further investigation [20]. The required operation temperatures restrict the applications of MCFCs to primarily large scale and remote power generation.

Proton Exchange Membrane Fuel Cells Arguably one of the most commercially produced and researched fuel cell technologies, second only to SOFCs, Proton Exchange Membrane fuel cells (PEMFCs), shown if figure 2.5 (D), utilize a polymer film electrolyte to facilitate the transfer of hydrogen ions from the anode to the cathode, the operation of which is detailed in figure 2.1. The most widely

produced PEM electrolytes are made of high molecular weight sulfonated aromatic polymers [21]. Such materials require a much lower operating temperature relative to most other fuel cell technologies, being operated between 50 and 80 °C [14, 22, 23].

$$\begin{aligned} \text{Anode:} \quad & 2\ H_2 \longrightarrow 4H^+ + 4e^- \\ \text{Cathode:} \quad & 2\ O_2 + 4H^+ + 4\ e^- \longrightarrow 2\ H_2O \\ \text{Overall:} \quad & 4\ H_2 + 2\ O_2 \longrightarrow 2\ H_2O + \text{electric energy} + \text{heat} \end{aligned} \tag{2.5}$$

Low temperature operation requires less expensive equipment to isolate the system from its surroundings but also requires more expensive catalysts to facilitate the oxidation of hydrogen at the anode. In addition, liquid water byproducts become an issue contrary to high temperature systems where the anode products are primarily vaporous. The removal of liquid water must occur constantly in PEM cells in order for the system to operate at peak efficiency.

PEMFC electrodes utilize a bi-layer construction of a catalytic active layer and a gas diffusion layer. The active layer is composed of primarily PTFE deposited with a platinum catalyst. Platinum is sensitive to poisoning by carbon monoxide, therefore, pure hydrogen is necessary for optimal performance. The gas diffusion layer is primarily made of a porous carbon cloth or paper to allow gases to flow freely through it as well as assist in the conduction of electrons. This layer is often coated in PTFE to facilitate the removal of liquid water from the system [22, 24–26]. Because of their flexible materials and low operating temperatures, PEMFCs are the most promising fuel cell technology for use in transportation applications.

Electrochemistry

The field of electrochemistry covers all phenomena by which electric forces drive a chemical reaction or vice versa a chemical reaction generates an electrical current.

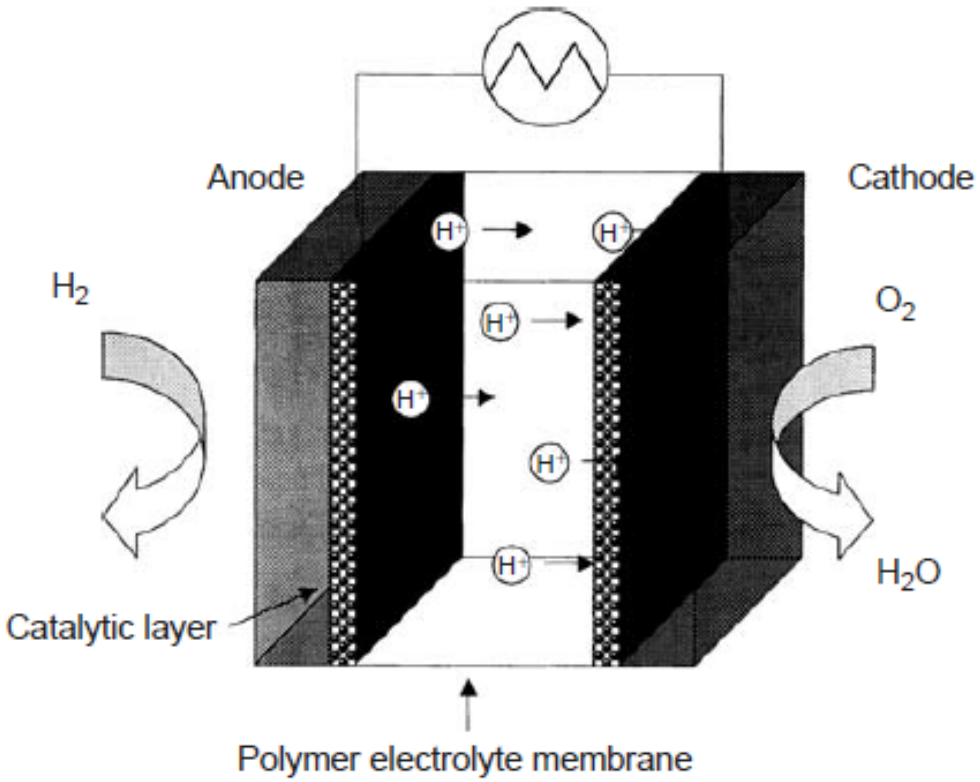


Figure 2.1: Schematic of the basic operation of a proton exchange membrane fuel cell.

This includes the charge and discharge of consumer batteries and the conversion of chemical energy into electricity by way of hydrogen fuel cells. In both cases, an oxidation reaction occurs at one electrode, known as the anode, and an entirely separate reduction reaction occurs at an opposite electrode, called the cathode. When these two reactions are combined, the resulting reduction-oxidation (redox) reaction drives the flow of electrons to an external load or to charge a drained battery if the reaction is reversed. In general, a battery operates by the oxidation and reduction of solid-state chemical species within the construction. Fuel cells, on the other hand, all rely on the oxidation of a hydrogen-rich fuel and the reduction of oxygen, which ultimately results in the release of electrons and the formation of water (vaporized or

liquid).

The theoretical performance for an electrochemical system is determined by the Nernst equation, defined by equation (2.6) which is derived from the thermodynamic quantity of Gibb's Free Energy. In this equation, R is the universal gas constant (8.3145 $\frac{J}{Mol*K}$), T is operating temperature (or the temperature of the system), n is the number of electrons generated, F is Faraday's constant (96485.3329 $\frac{A*s}{mol}$), and $a_{red/ox}$ is the activity of the species present in the reduction and oxidation reactions respectively. The Nernst potential is the hypothetical maximum voltage available to the device at equilibrium, when no reactions are occurring at the electrodes and no current is flowing. This is known as open-circuit voltage (OCV).

$$E = E^{\circ} + \frac{RT}{nF} \ln \frac{a_{red}}{a_{ox}} \tag{2.6}$$

From OCV, an overpotential can be applied to the system by way of an external load or source. This overpotential polarizes the electrodes, initiates the chemical reactions, and dictates the flow of electrons. Polarization of the device can be either positive (anodic polarization), which will force electrons from the anode towards the cathode, or negative (cathodic polarization), which can be used to reverse the reaction.

The Nernst potential is based largely on the standard potential (E°) of the reversible reduction reaction for which the electrochemical system is based. Many lists of these standard reaction potentials exist, the most notable being the NIST-JANAF thermochemical tables published by joint operating naval and airforce scientists. These standards are based on a reference electrode known as the standard hydrogen electrode (SHE). The basis of the SHE is a single platinum electrode supplied with pure hydrogen and submerged in a bath rich with hydrogen ions (an acidic bath for example). As a reference, the SHE is considered to have a null reduction potential.

Since the reduction reaction for the SHE is the reduction of hydrogen, the standard reduction potential for all fuel cells utilizing a hydrogen-rich fuel is zero. Two additional factors should be noted about equation (2.6). First, this potential is highly dependent on temperature. For example, two identical fuel cells operating at two different temperatures will not produce the same voltage despite all other factors being equivalent. This relationship can be seen in figure 2.2 for the fuel cell constructions discussed in the next section. Second, the primary reactants and products in most fuel cell technologies are gases flowing at relatively low pressures, therefore, the activities of these species are assumed to be equal to the partial pressures of the gases.

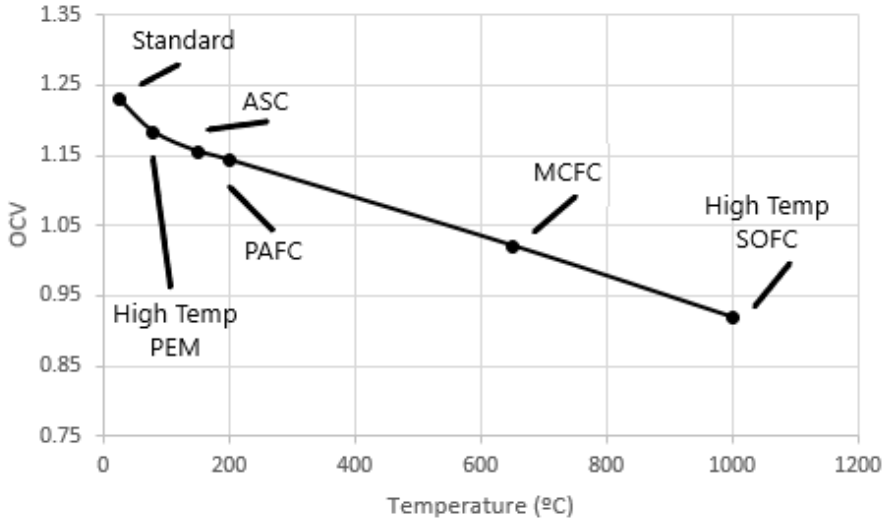


Figure 2.2: Relationship between OCV and operating temperature for several common fuel cell constructions

If thermodynamics determines the maximum potential of these devices, then kinetics limits their performance and describes the mechanisms by which this occurs in application. These effects are most accurately depicted by a polarization curve, represented in figure 2.3.

Polarization curves are produced by generating a range of currents and analyzing

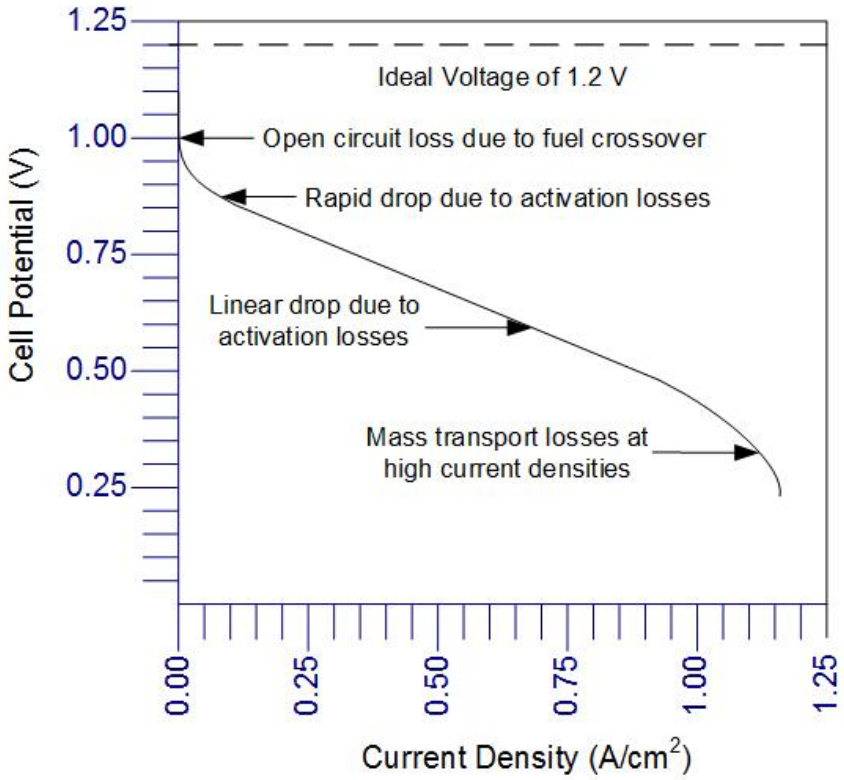


Figure 2.3: General polarization curve for an electrochemical device with primary regions of loss labeled [27]

how the voltage reacts across the range. Alternatively, a range of overpotentials can be applied to observe the opposite effect. If the latter is performed, the applied overpotentials are subtracted from OCV to generate an accurate graphical representation. The regions of interest in figure 2.3 are the initial activation losses, the large linear region of ohmic losses, and the final transport losses. Additionally, from this V-I data, a power curve can be extrapolated by the equation $P = V * I$ and demonstrates the general output and performance of the cell. Maximum power output is often related to a cell potential between 0.5 and 0.7V. While the losses associated with electrochemical devices are often unavoidable, apprehension of the mechanisms behind the losses has led to the design of more efficient battery and fuel

cell technologies.

Activation Losses At the top of the curve, an initial overpotential is required before the polarization of the cell is adequate to begin the chemical reaction process. The losses associated with this are known as capacitive or activation losses and represent the natural electronic storage of the cell. These initial losses are unwanted and can be diminished by increasing the temperature, and by extension, the energy in the system, or by utilizing enhanced catalytic materials to lower the energy required to drive the chemical reaction [28, 29]. Exchanging the catalyst of either the anodic or cathodic half-reaction can alleviate the effects of these losses but cannot eliminate them entirely. The directionality of electrochemical devices ensures that polarization must be induced in one direction or the other in order to initiate the chemical processes [29, 30].

Ohmic Losses The largest region of the polarization curve is related to ohmic losses in the cell. This region is linear, with voltage depreciating as current increases, and represents the natural resistivity of the cell. The exact resistance of the device is calculated as the slope of this region. Therefore, a steep ohmic loss region represents a system with high resistance and vice versa. To mitigate ohmic losses in an electrochemical device the electrodes are composed of materials with high electrical conductivity, ensuring that electron transport occurs as rapidly as possible [30, 31]. The second mitigation strategy is to decrease the thickness of the electrolyte layer. Reducing the distance over which the conducted species must travel increases the rate at which the primary electron generating reaction can occur [29, 32].

Transport Loss As current densities increase further, cell potential experiences a sharp drop off. At this point, fuel cannot be supplied fast enough to facilitate

the rate at which the cell is being driven. Losses of this kind are known as mass transport losses and are caused by a lack of chemically active area, a build-up of the products of the chemical reaction (usually liquid or vaporized water), or an inadequate supply of fuel. Transport losses are most pronounced after a period of degradation when the anode has undergone significant microstructural evolution [1]. These effects can be reduced by optimizing the concentration of active area in the electrodes or enhancing the stability of the active area to persist for longer operation period [29,30]. The former method will mostly effect the device during initialization while the latter reduces the affect of structural degradation of the active areas, allowing the cell to run more effectively over longer time periods.

Solid Oxide Fuel Cells

Operation and Design

SOFCs are fundamentally different from all other fuel cell technologies because all components of the cell are made of solid-state metals and ceramics. In order to facilitate the diffusion of large oxygen ions through a ceramic membrane, SOFCs must operate at elevated temperatures between 600-1000 °C. This requires the use of sophisticated furnace and insulated equipment but does have some benefits. First, it allows for the catalysis of certain carbonaceous fuels within the anode, increasing the variety of fuels that can be used. Second, energy from the heat being expelled can be harvested and utilized in other systems such as steam turbine generators, overall increasing the efficiency of the fuel cell system.

SOFCs operate by flowing hydrogen-rich fuel over the porous anode and air over the cathode. The oxygen in the air is catalysed into ions by the cathode materials and adsorbed into the electrolyte. These oxygen ions then hop through defects in the electrolyte material's lattice to the anode. At this point, the hydrogen from the fuel

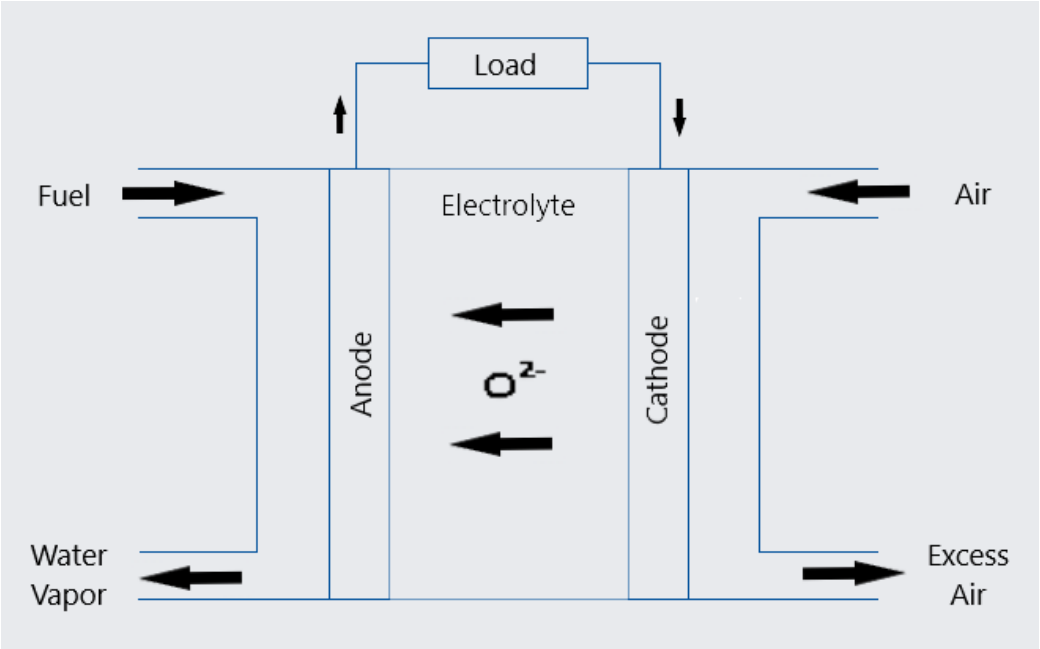


Figure 2.4: Schematic of the basic operation of a solid oxide fuel cell.

reacts with the conducted oxygen ions to release electrons and produce water vapor. The electrons are conducted out of the anode, through an external load, and into the cathode where they assist in the catalysis of oxygen. The reactions that occur at each of the electrodes are described by equation (2.7). These reactions occur in areas of the electrodes where fuel/oxidant (porosity), catalyst, and ion conductor intersect. This active area is known as a triple phase boundary (TPB, depicted in figure 2.6) and the overall performance of the cell is directly related to the concentration of TPB in the anode.

$$\begin{aligned} \text{Anode:} \quad & 4\ H_2 + 2\ O^{2-} \longrightarrow 4\ H_2O + +4e^- \\ \text{Cathode:} \quad & O_2 + 4\ e^- \longrightarrow 2\ O^{2-} \\ \text{Overall:} \quad & 4\ H_2 + 2\ O_2 \longrightarrow 2\ H_2O + \text{electric energy} + \text{heat} \end{aligned} \tag{2.7}$$

Two main categories of SOFC exist: Anode supported (ASC) and electrolyte

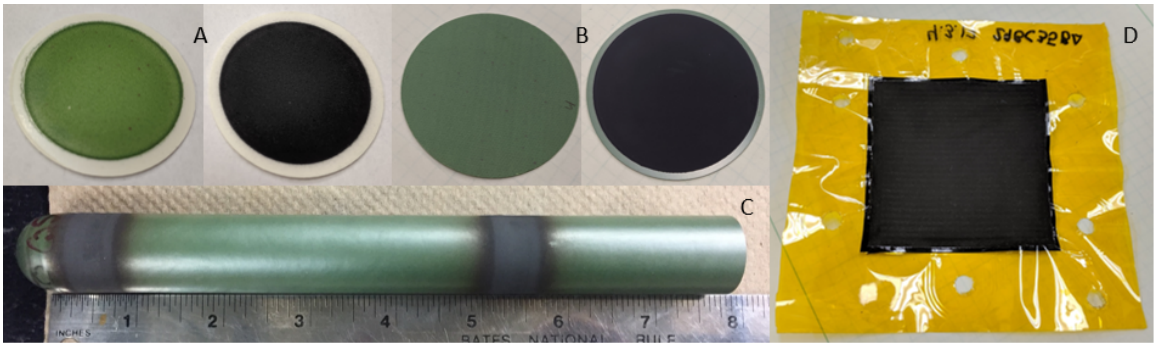


Figure 2.5: Various common constructions of fuel cells. A) Electrolyte supported SOFC anode (left) and cathode (right), B) Anode supported SOFC anode (left) and cathode (right), C) Tubular SOFC with electrolyte and cathode strips visible (anode material on interior), and D) PEMFC with Nafion electrolyte (yellow film) and electrode (black) visible.

supported (ESC) cells. Additionally, there have been reports of the use of cathode supported cells, but they are rare and almost never utilized in industry. This designation refers to the component that primarily supports any loads introduced to the system and largely determines the mechanical properties of the cell. ASCs can achieve excellent current densities in application because electrolytes of thickness on the order of tens of microns can be attained. Thin electrolyte layers are favored because it reduces the distance for oxygen ions to travel from the cathode to the anode. ASCs come in two designs: tubular and planar. Tubular ASCs were some of the first commercially produced SOFCs while planar cells are more recently becoming the industry standard due to their ease of manufacture compared with tubular designs [33]. ESCs are not capable of producing current densities comparable to ASCs because of their thick electrolyte (usually about 300 μm) but are more easily manufactured and tend to be more consistent in both power production and electrochemical resiliency. ESCs are primarily designed to be planar. Examples of these SOFC constructions are shown in figure 2.5 (A-C).

Regardless of designation or design, SOFCs must be grouped, connected, and

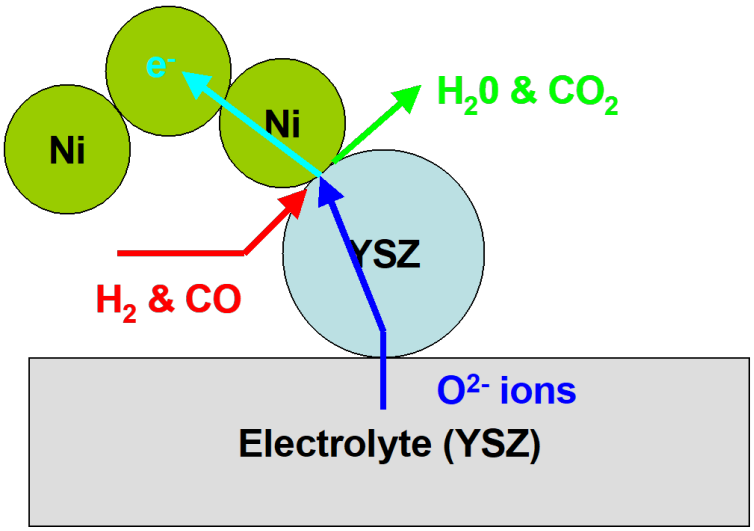


Figure 2.6: Rough schematic of the anodic triple phase boundary.

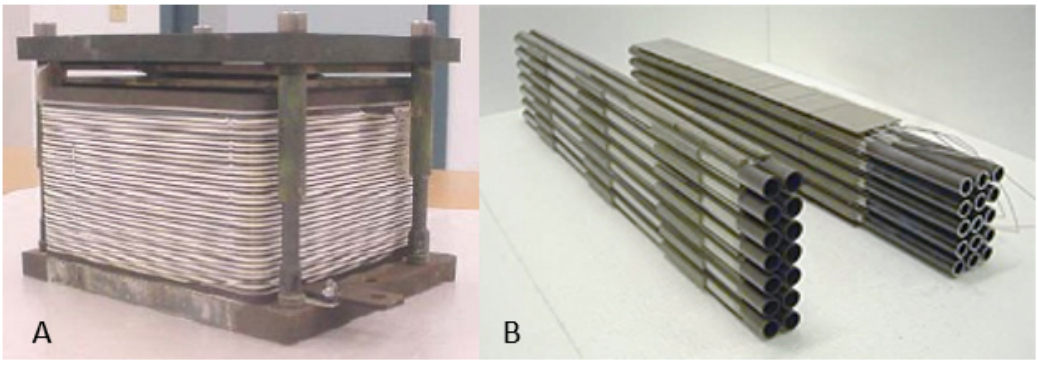


Figure 2.7: Common stack configurations for A) planar SOFCs, and B) tubular SOFCs.

sealed together in order to produce an appreciable amount of power. These groupings are called arrays or stacks and include a metallic interconnect, a sealing braze, and an outer casing. Common configurations of these stacks are shown in figure 2.7, while the components of a planar stack are shown in figure 2.8. The interconnects provide current collection and gas channels to supply fuel and oxidant to their respective electrodes. The sealing braze is necessary to restrict the flow of gases and keep electrical contact between all components. The outer casing protects the interior

components (primarily the fuel cells themselves) from physical shock and exterior environmental impacts, thermally insulates from the environment, and provides adequate clamping force to ensure proper contact between cells and interconnects.

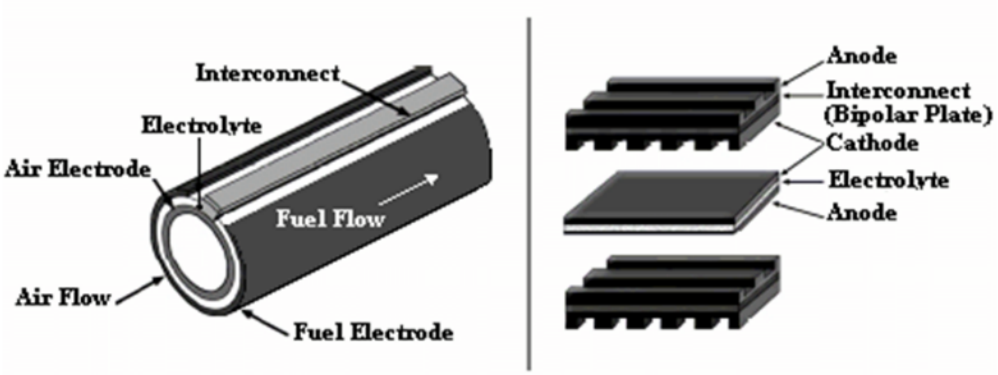


Figure 2.8: Necessary stack components for tubular SOFC arrays (left) and planar SOFC stacks (right). The latter applies to both ESCs and ASCs [34]

Materials

Each component in the SOFC system must fill a specific role in order to operate effectively. Therefore, each component must be made of equally specific materials to fill that role. The following discusses the classes of materials appropriate for each component, specific materials currently employed in SOFC designs, and various materials being researched for the replacement of these currently employed materials.

Anode	Electrolyte	Cathode
• Electronic conducting • Catalyze the dissociation of fuels • Allow for transport of fuels and oxygen Ions	• Ion conducting • Electronic insulating • Robust within operating conditions	• Electronic Conducting • Stable under highly oxidizing conditions • Allows for the transport of air and Oxygen ions

Figure 2.9: Material requirements for each of the three SOFC components

Cathode The cathodic electrode facilitates the adsorption of oxygen ions into the electrolyte and aids in the conduction of electrons through the circuit. To perform effectively this electrode must be composed of an electronically conducting material, remain stable under highly oxidizing environments, catalyze oxygen, and is manufactured to be porous to allow oxygen gas to flow freely throughout. These constraints rule out many common engineering materials: transition metals oxidize readily under such atmospheres; noble metals, which do not oxidize readily, are expensive and rapidly degrade at elevated temperatures; and metal oxides do not possess the electronic conduction necessary to complete the circuit. Therefore, to meet such unusual requirements, a class of engineered ceramic materials known as perovskites must be utilized. Perovskites are combinations of various transition metal oxides to form the stoichiometry of ABO_3, where A and B are metal cations of 2+ and 4+ valence states respectively. The structure, a cubic of cations surrounded by an octohedron of anions (shown in figure 2.10), along with the varying cation valence states, grant this class of material interesting mixed electronic and ionic (MEIC) properties. The most common cathode perovskite materials are composed of some combination of lanthanum, strontium, calcium, manganese, iron, cobalt or nickel. Commercially manufactured SOFCs most often utilize lanthanum strontium manganite (LSM) or lanthanum calcium mangantite (LCM) cathodes because these materials share close thermal expansion properties with YSZ [14]. However, studies have shown that substituting cobalt for some percentage of manganese increases both electronic and ionic conductivity [35]. In addition, composite materials of these perovskites and electrolyte materials enhances adherence of the cathode to the electrolyte as well as the overall adsorption of oxygen ions. The development of double perovskite materials (perovskites containing two different B site cations) has led to studies into these oxides as cathode materials. However, these materials are

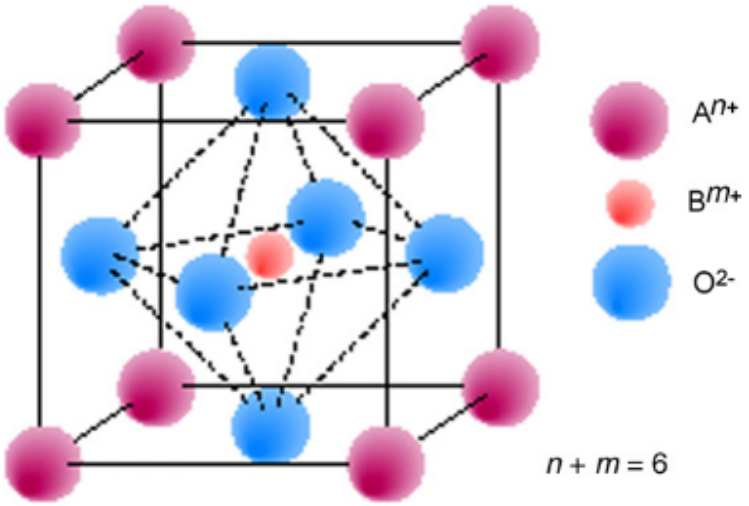


Figure 2.10: Unit cell of the ABO_3 perovskite structure [31]

difficult to produce, are composed of expensive constituents, and their bulk properties have not been investigated in-depth as of yet [36, 37].

Electrolyte The electrolyte is central to the function of fuel cells, acting as an insulating layer between the two electrodes, and facilitating the conduction of oxygen ions from the cathode to the anode. In addition, the electrolyte material must be stable in both oxidizing and reducing atmospheres. In most fuel cell technologies, the electrolyte is made of an aqueous mixture of the ions to be conducted, however, in SOFCs all components are made of solid-state materials that are less conducive to ion conduction than solutions. Solid-state ion conductors operate by exploiting a concept from defect chemistry known as an oxygen vacancy. Essentially, when the lattice of a ceramic material is formed, various factors cause a lack of oxygen atoms at randomly distributed locations. The lattice defect naturally possesses a positive charge which attracts any stray negatively charged oxygen ions. This mechanism allows an oxygen ion to jump from vacancy to vacancy through a ceramic film of considerable thickness.

This also forms the basis of metallic corrosion through an oxide film.

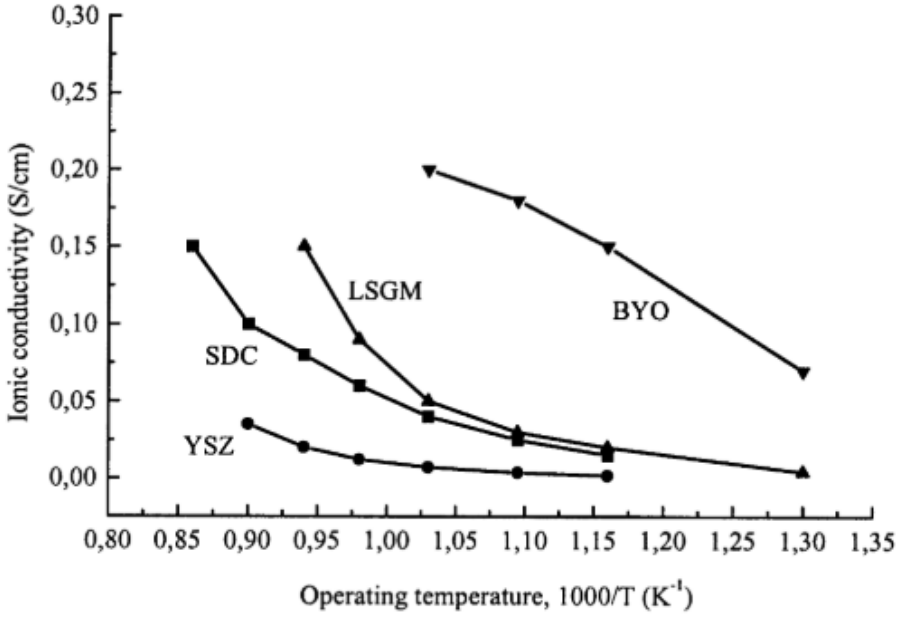


Figure 2.11: Ionic conductivities of commonly used electrolyte materials [14]

Most, if not all, ceramic materials are afflicted with oxygen vacancy defects, but few naturally occurring metal oxides contain adequate concentrations to be used as an ion conductor in SOFCs. To alleviate this issue, ion-conducting materials are engineered by alloying two metal oxides of varying stoichiometries to force the formation of oxygen vacancies in more significant distributions. The most common among these engineered ceramics used in SOFCs are cubic structured zirconium oxide and cerium oxide, with or without various mineral dopants.

Zirconium dioxide (ZrO_2, zirconia) exhibits polymorphic behavior at elevated temperatures, undergoing two phase transformations between room temperature and its melting temperature at 2690 °C. Each of these phase changes is accompanied by a change in volume associated with the structural evolution of the material. The stresses inherent to such volumetric changes make processing zirconia at high temperatures

difficult. Despite this, the widely varying properties evident in each of the three phases makes zirconia one of the most versatile engineering ceramics. The monoclinic phase, which is stable at room temperature, functions similarly to most other ceramics, possessing excellent thermal properties but virtually no structural integrity. At 1170 °C zirconia transitions to a tetragonal structure, drastically increasing strength and toughness but is considered metastable and decomposes at temperatures above 300 °C. Finally, above 2370 °C (until it melts at 2690 °C), the previously stable tetragonal phase restructures into a perfectly cubic fluorite structure. As with the first transformation, a noticeable strength enhancement is observed from cubic zirconia as well as changes in optical properties and a propensity to conduct oxygen ions. The latter, attributed primarily to the symmetric nature of the lattice, is most interesting from the perspective of SOFC technology [38].

The development of methods to preserve these phases revolutionized its use as an engineering material. These processes involve the alloying of zirconium with stabilizing agents such as calcium oxide (CaO), magnesium oxide (MgO), or yttrium oxide (Y_2O_3). Small concentrations of about 2 to 5 m% of these dopant oxides are adequate to stabilize the tetragonal phase while increasing to between 8 and 12 m% can stabilize the cubic phase. The processing of stabilized-zirconia materials produced a secondary result benefiting the field of SOFCs. The varying stoichiometries between zirconia and the stabilizing oxides created increased concentrations of oxygen vacancy defects necessary for oxygen ion mobility. This was particularly evident in yttria stabilized zirconia (YSZ), which has since become the industry standard for electrolyte materials in SOFCs. These effects are depicted in figure 2.12. YSZ can be used in either the tetragonal (3YSZ, doped with 3 m% Y_2O_3) or the cubic (8YSZ, doped with 8 m% Y_2O_3) phase. 3YSZ has a significantly greater mechanical strength inherent to the tetragonal structure while 8YSZ possesses a greater proficiency for conducting

ions [14, 35, 36, 38, 39]. Due to its thermal and chemical stability, there are few other materials in contention with YSZ, however, recent studies with various rare earth metals has shown that a scandia-stabilized zirconia (SSZ, 8-9 m% Sc_2O_3) possesses greater ionic conductivity and mechanical strength, but the cost and availability of scandium is of concern [35, 36]. Other research has noted the possibility of using complex zirconate perovskite materials composited with carbonates, but the effects are associated primarily with the formation of a continuous solid carbonate phase rather than the zirconia-based material [36].

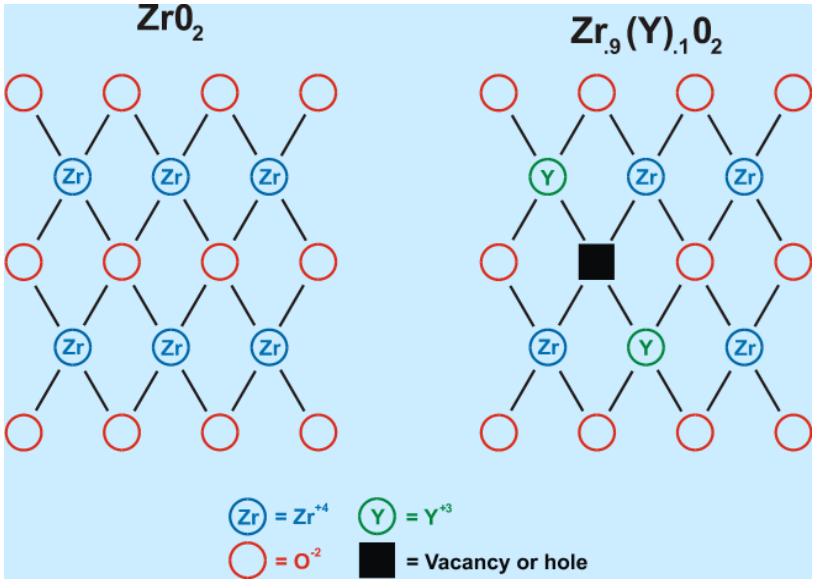


Figure 2.12: Effects of alloying zirconia with stabilizing oxides resulting in the formation of oxygen vacancies.

Cerium oxide (CeO_2, Ceria), also possessing a cubic fluorite structure, inherently exhibits considerable ionic conductivity without the detrimental effects of polymorphism associated with zirconia. While initially not as conductive as tetragonal stabilized zirconia, when doped (between 10 and 20 m%) with a secondary oxide component such as calcium oxide, gadolinium oxide (Gd_2O3), or samarium oxide (Sm_2O_3) ceria electrolytes often surpass 8YSZ, as can be seen in figure 2.11. The

effect of these dopant materials on the ceria lattice is similar to that of yttria doping in the zirconia system. The mismatch in stoichiometries, particularly between AO_2 and A_2O_3 structures, causes anion voids which can later be exploited by oxygen ions traversing the electrolyte. Ceria based electrolytes are most often employed in low and intermediate temperature SOFCs which operate between 500 and 700 °C. Within this range, doped ceria electrolytes far surpass all known ceramic ion conductors [14, 32, 40]. An issue arises when ceria electrolytes are exposed to highly reducing atmospheres, as would be experienced on the anode side of a SOFC. Various researchers have discovered the tendency to develop substantial electrical conductivity during operation, in effect shorting the cell across the electrically insulating layer and causing a drop in OCV [32, 35]. This phenomenon is derived from the reduction of CeO_2 (Ce^{4+}) to Ce_2O_3 (Ce^{3+}), resulting in charge carriers that increase the electronic conductivity across the electrolyte. This has been counteracted by coating the anode side of the electrolyte in a thin layer of electrically insulating material, usually YSZ [32]. The necessity of this coating only increases the cost of processing ceria based electrolytes, disrupting its viability for large scale commercialization. More recent research has investigated the effects of co-doping ceria with rare-earth and alkali metals, resulting in an adaptable material that could exhibit ionic, electronic, or mixed conductivity [32, 37].

Other classes of ceramics have been shown to be effective in conducting oxygen ions, but with little interest from the SOFC industry. Certain perovskites designed with primarily ion conductivity have shown promise as electrolyte materials. Lanthanum gallate doped with strontium and manganese (LSGM) has shown exceptional ionic conductivity at intermediate and high-temperature operation [35]. LSGM is also the standard electrolyte chosen for use with newly developed MEIC anode materials which will be discussed in the following section. Like ceria, however, LSGM exhibits a

tendency to break down under reducing conditions, causing the rapid evaporation of gallium on the anode side of the cell. Newly developed, fluorite structured, rare earth molybdenum oxides are one of the newest editions to the growing family of electrolyte materials. Reports indicate these new materials surpass 8YSZ ionic conductivity by a factor of four [37]. However, beyond these initial tests, very little is known about these materials. Further testing of mechanical properties, reduction kinetics, and component interactions must be performed prior to implementation for SOFCs.

Anode Truly the powerhouse of the SOFC, the anode is the location of the primary electron generating chemical reaction. This reaction occurs exclusively at the TPB where the fuel (provided through open porosity) interacts with oxygen ions, which have traversed the electrolyte, to generate electrons and produce water in the form of steam. To facilitate this reaction, the anode structure must be porous, made of an electronic conducting component and an ion-conducting component, and be thermally and chemically stable in highly reducing conditions. The necessity of both electronic and ionic conduction in this electrode requires the use of either Cermet composite or an engineered MEIC material. Cermets, while difficult to process and ultimately possess inadequate thermal stability, are inexpensive and have formed the basis of the industry standard for SOFC anode materials. MEIC materials, on the other hand, have the advantage of a single phase, making processing nearly irrelevant. However, these materials are expensive to manufacture and are still being investigated to determine their exact material properties, both mechanically and electrochemically.

As stated previously, the current industry standard for SOFC anode materials is a cermet composite of nickel metal electro-catalyst and YSZ ion conductor. Most transition metals possess adequate electrical conduction for use as the metal component in these cermets, but nickel has the unique attribute of being able to catalyze

carbonaceous fuels (CH_4, syngas, etc.) during normal SOFC operation [31, 41]. This internal reformation process drastically increases the fuel flexibility of SOFC anodes. Internal reformation is still a possibility without a capable material but requires secondary apparatus in line with the fuel reserves to break down carbonaceous fuels and extract the usable hydrogen, as shown in figure 2.13. Platinum-based anodes are an example of such a system requiring internal reformation equipment. The

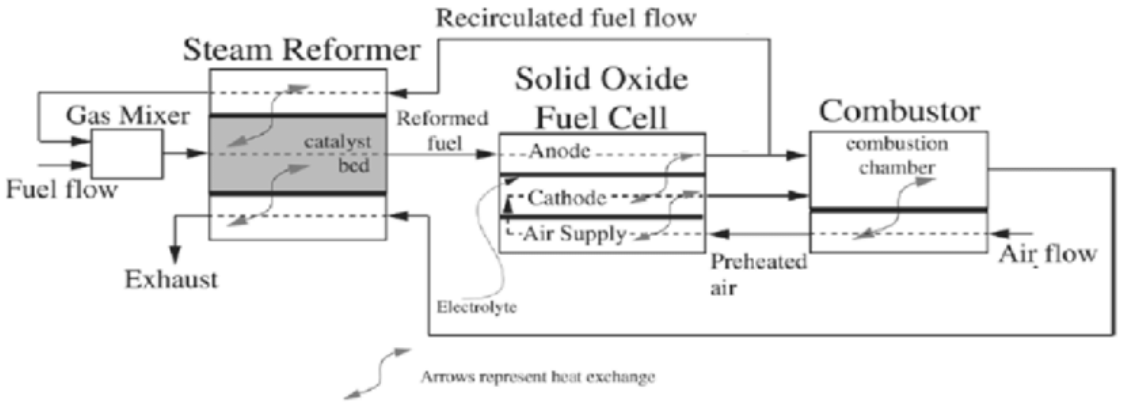


Figure 2.13: Schematic diagram of a more complex SOFC system including steam reforming apparatus and external combustion turbine for heat recovery [42].

exceptional electrical conductivity of platinum far exceeds that of nickel but anodes made from platinum catalysts degrade rapidly in the presence of carbon monoxide. While not considered industry standards for SOFC anodes, both copper and cobalt are known to be internally reforming and capable of producing current densities on par with identical nickel-based anodes [31, 43]. However, because of cost, toxicity, or difficulty of processing, these materials have fallen far behind nickel in their use in anodes. The other advantage to nickel in SOFC anodes is ease of processing with the ceramic component of the composite. No matter what metal is used, it is difficult to effectively conjoin a metal component with a ceramic component. To avoid this issue, the metal material is processed in its oxide phase. Nickel is especially effective for this

because its oxide phase readily reduces at optimum SOFC operating conditions. The ceramic component, on the other hand, may be any number of effective ion conductors and is usually chosen to match the electrolyte material, therefore, YSZ is the most common. While this is not entirely necessary, it does create less resistance as ions are passing from the electrolyte to the anode system, more effectively matches thermal expansion coefficients between anode and electrolyte, and guarantees good adhesion. Doped ceria compounds seem to be the most common alternative to YSZ because of their similarity [37, 40, 44–48]

MEIC materials are still in the early development phase for implementation in SOFCs and often require the use of specific electrolyte materials to enable proper function. These materials possess the sole advantage of carrying both ions and electrons by using a single phase, reducing processing incompatibilities within the anode, and eliminating the need for TPB active sites. Instead, the active area of an MEIC anode is the entire area of material that is exposed to fuel and adhered to the electrolyte. This effect is visualized in figure 2.14. Depending on the macrostructure and porosity contained within an anode made with these materials, the area of the electrode at which chemical reactions occur increases dramatically. The most common MEIC materials are derived from perovskites, similar to those used as cathode materials. Lanthanide (La, Nd, and Sm) based perovskites doped with titanium, strontium, and manganese are the most popular perovskites for use as anode materials and have been shown to have little deleterious effects on both YSZ and GDC electrolytes at or below normal operating temperatures [31, 37]. Others have suggested that replacing titanium with chromium performs more similarly to Ni/YSZ cermet anodes [28, 31]. Many combinations of alkali metals, transition metals, and lanthanides exist that produce perovskite structured materials exhibiting varying levels of MEIC behavior. The issue becomes discovering a combination that

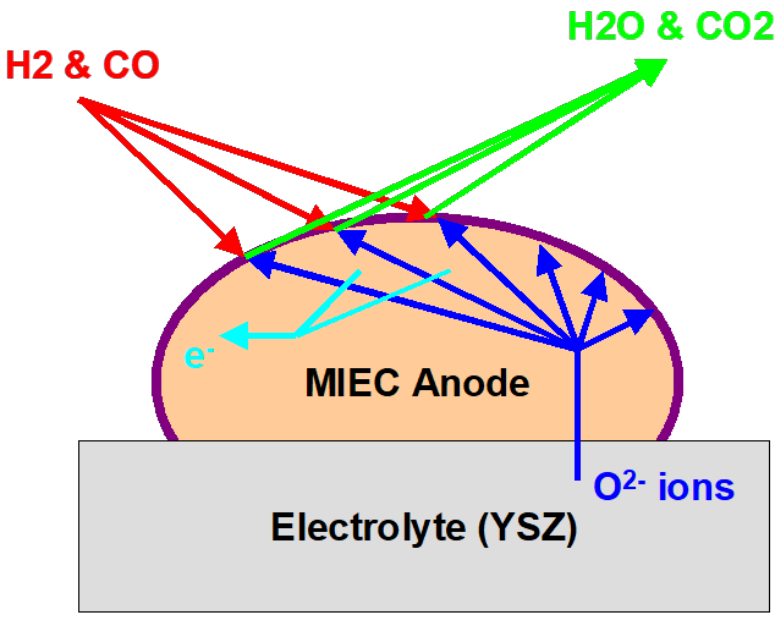


Figure 2.14: Rough schematic of MIEC anode materials.

is both inexpensive to manufacture and effectively replaces current Ni/YSZ cermet anodes. More recent development of perovskite materials has led to the discovery of an alternating, but still repeating, double perovskite structure. Initial studies of these materials have predicted their ability to surpass all other materials for use as MEIC anodes but due to difficulty processing fully dense samples, their full potential is yet to be realized [37].

Anode Resiliency

The cermet materials utilized for the anode electrode of SOFCs are prone to failure or degradation in several ways. These sources are primarily associated with the acceleration of thermodynamic driving forces by the operating conditions, however, the lack of physical resiliency or mechanical strength of the cell is often a contributor to failure as well. A single fuel cell wafer, only being able to produce about 1 volt, can generate roughly enough current to power a single light bulb. Therefore, in order to

produce any sort of appreciable power, a number of these cells must be connected in series and sealed together in what is called a stack (depicted in figure 2.7). Optimum clamping pressures in these stacks are between 60 and 75 kPa based on computational modeling of contact resistances [49]. The stresses experienced by the cell from these clamping pressures, as well as thermal stresses caused by operating conditions, can easily exceed the flexural strength of the supporting component (electrolyte or electrode). In addition, any defect, crack or otherwise, in the supporting component causes a stress concentration at that location, exponentially increasing the chance for failure.

Mechanical Strength A material's response to stress varies with each class of material. For example, the hardness of a metal directly relates to its resistance to plastic deformation and scales proportionally with the yield strength of the material. For ceramics, this is a different story. Based on their hardness, ceramic materials theoretically should possess a yield strength an order of magnitude greater than that of the strongest metals. However, the inherent brittle nature of the ionically and covalently bonded ceramic materials causes cracks to form, propagate, and fracture at loads significantly lower than theoretically predicted. Concepts such as these fall under the field of fracture mechanics and determine how and why a material will fail. While hardness and strength are good metrics for designing with metals, the toughness of a given material must be understood in order to effectively design against failure with any material. Toughness is ultimately representative of the resistance to crack propagation. The toughest materials, commonly ductile metals, have one thing in common; as a crack propagates through the material, the area directly in front of the crack tip undergoes plastic deformation (yielding), causing a drastic increase in strength (depicted in figure 2.15). At this point, unless the load is increased, the

crack cannot progress further. Ceramics, as mentioned before, possess incredible yield strength, therefore, the material usually does not yield to plastic deformation and the crack propagates freely through the material. This is known as brittle fracture and is the most likely method of failure in ceramic materials.

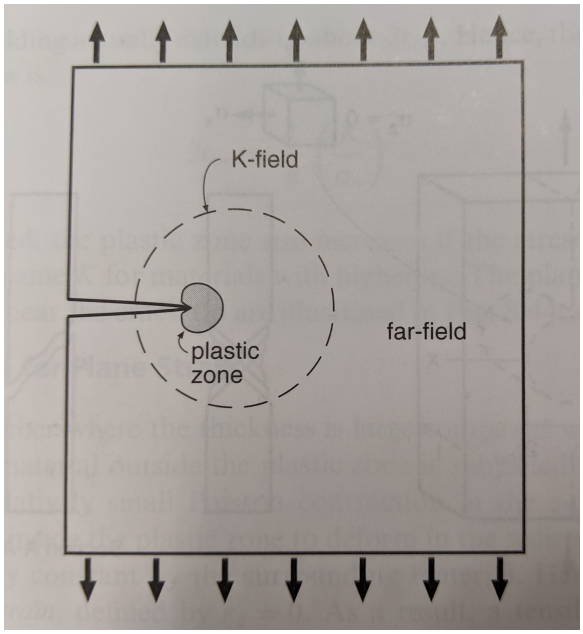


Figure 2.15: A cracked member and its associated plastic deformation zone. The K-field region is utilized for linear elastic fracture mechanics [50]

To investigate the toughness of a metal, a notched sample is placed under a tensile load, either in true uniaxial tension or by a bending method (3-point, 4-point, or concentric ring). Since the notch size is known, fracture toughness (K_{Ic})can be calculated from the failure stress using equation (2.8). Due to their brittle nature

$$K_{Ic} = \sigma\sqrt{\pi c} \tag{2.8}$$

Due to their brittle nature and inherently flawed microstructures, ceramics must be handled statistically. A notched sample is not necessary but the sample is still loaded

in one of the bending methods mentioned above. The natural distribution of flaws within a ceramic body requires a statistically significant sample population in order to fully define the toughness of the material. The values of fracture strength are compared against a reference stress for which there is a survival probability equal to 1/e and the strength of each sample will fall above or below this value, creating what is called a Weibull distribution [51]. From this distribution a Weibull modulus is calculated that describes the variability of the data. The combination of ASTM C1161 and ASTM C1239 active standards describe a common method of evaluating the flexural strength, also known as modulus of rupture, for ceramic materials [52,53]. This is a widely used method of analyzing the fracture mechanics of new materials as was used by McCleary et al. and Driscoll et al. to evaluate the strength of NiO/YSZ anode materials doped with aluminum titanate [3, 4], shown in figure 2.16.

	P-1400C-10h	P-1550C-5h	A-1400C-10h
Low Flexure Strength (MPa)	66.01	82.36	116.68
Mean Flexure Strength (MPa)	102.43	119.84	157.76
High Flexure Strength (MPa)	138.36	155.73	218.49
Standard Deviation (MPa)	15.95	17.94	32.51

	0% ALT	1% ALT	5% ALT	10% ALT
Oxidized (NiO/YSZ)				
Average strength σ/MPa	100	136	226	150
V_{eff}/mm^3	1.8	3.2	1.1	0.9
Scaled Characteristic strength σ_0'/MPa	137	213	234	156
Strength Increase/%	N/A	55	71	14
Reduced (Ni/YSZ)				
Average strength σ/MPa	120	151	164	187
V_{eff}/mm^3	0.9	1.5	0.7	0.5
Scaled Characteristic strength σ_0'/MPa	120	175	168	186
Strength Increase/%	N/A	46	40	55

Figure 2.16: Two tables representing data reported for the mechanical properties of NiO/YSZ anode materials. The table on the left represents ring-on-ring testing for undoped samples treated at 1400 and 1550 °C and ALT doped samples treated at 1400 °C [3]. The table on the right represents mechanical properties data gathered from modulus of rupture experiments [4]

For the experimental methods described above, an incredible number of samples must be manufactured and destructively tested in order to form a statistically significant relationship. This is not conducive to short term projects where testing

may take the entire allotted time period just to determine one material property. Therefore, new experimental methods are being developed that utilize non-destructive testing to acquire similar results with fewer samples. One such method employs the use of a Vicker's hardness micro indenter to extrapolate a form of K_{Ic} referred to as indentation fracture resistance (K_{ifr}). An indentation on the surface of a polished ceramic sample results in a plastic deformation region beneath the impression and causes cracks to form and propagate radially from the indentation. Using the average of these crack lengths along with the cross length of the indentation, measured hardness for the indentation and the elastic modulus, a value of K_{ifr} can be calculated by either of the equations in (2.9) [54].

$$\begin{aligned} &\text{a)} \qquad K_{ifr} = 10.4\ E^{0.4}\ P^{0.6}\ \frac{a^{0.8}}{c^{1.5}} \\ &\text{b)} \qquad K_{ifr} = 0.0334 \frac{E}{H}^{0.4}\ \frac{P}{c^{1.5}} \end{aligned} \tag{2.9}$$

While there is some disagreement among researchers on this topic, the trend of values gathered from this equation seem to agree with modulus of rupture experimentation described above, as shown in figure 2.17 [3, 4, 7].

Electrode Degradation During operation, thermodynamic driving forces are accelerated due to the elevated operating temperature (600-1000 °C). These forces cause microstructural evolution within the anode resulting in the depreciation of active sites and ultimately the degradation of cell performance. A summary of these mechanisms is depicted in figure 2.18. This evolution is attributed to the coarsening of nickel particles by a diffusion mechanism known as Ostwald Ripening. In attempts to reduce the overall energy of the system, mass transfers through a diffusion process

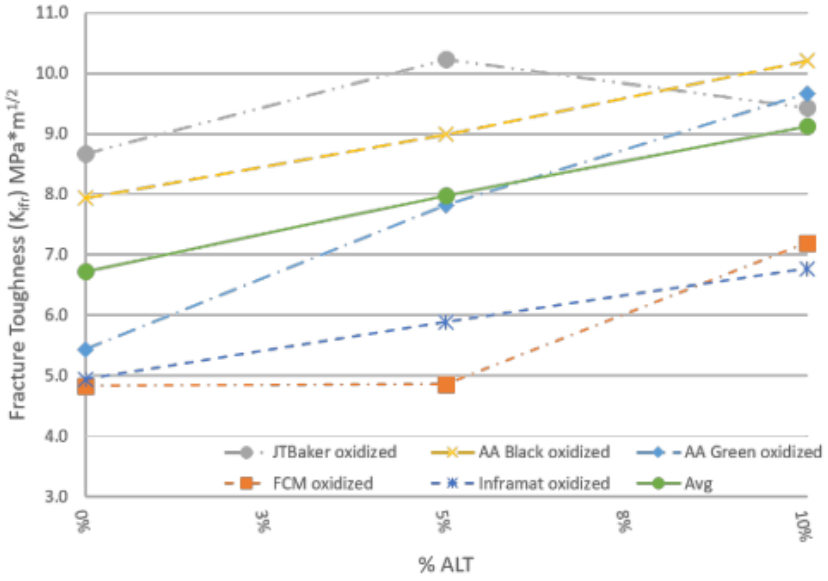


Figure 2.17: Results of indentation fracture resistance studies on NiO/YSZ anode materials using powders from various suppliers [7].

from particles of high interfacial energy to particles of low interfacial energy [20]. In other words, from small particles to large ones. This process, coupled with a poor inter-connectivity between the nickel and ceramic particles, causes large scale migration and agglomeration of nickel metal throughout the cell [37, 55–57]. This process is represented in figure 2.19 within a bi-layer anode-supported SOFC utilizing a functional layer and a support layer. Agglomerates of nickel metal are not inherently detrimental as it helps foster electronic conduction pathways through the anode. However, after many hours of coarsening, these agglomerates often fill in open porosity necessary to form the TPB that facilitates the chemical reaction between the fuel and the oxidant.

The second mechanism to the loss of anode functionality stems from the use of impure carbon-containing fuels such as methane or syngas. Although many of the catalytic materials used in SOFCs are considered to be internally reforming, the

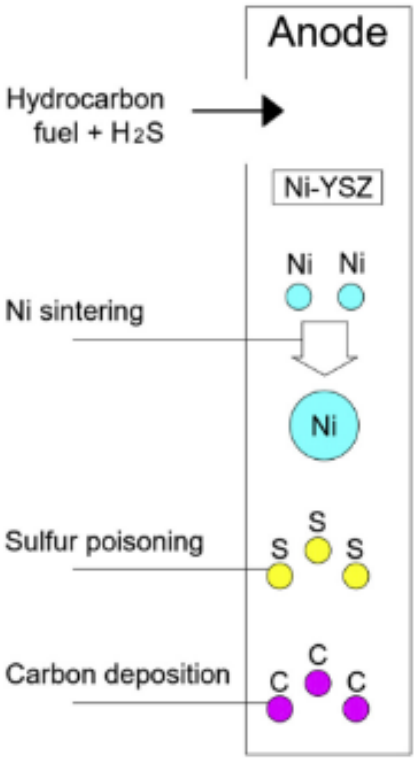


Figure 2.18: SOFC degradation mechanism scheme [37]

byproducts of using such fuels are often harmful to the anode. Carbonaceous fuels, while being hydrogen-rich, also deposit the leftover carbon on the surface of the catalysing material. Better known as coking, carbon deposition clogs the active areas of the anode, hampering its ability to further catalyze fuel, and slowing the production of electrons. In addition to carbon, these fuels (particularly fuels like syngas) often contain other contaminants such as hydrogen sulfide (H_2S). At operating temperatures hydrogen sulfide reacts with oxygen to form water vapor and pure sulfur which subsequently reacts with nickel to form Ni_3S_2 [55, 58]. This compound volatilizes at SOFC operating temperatures resulting in the reduction of overall nickel content in the anode. The extent of damage caused by this volatilization can be seen in figure 2.20. Understanding, modeling, and preventing these degradation mechanisms

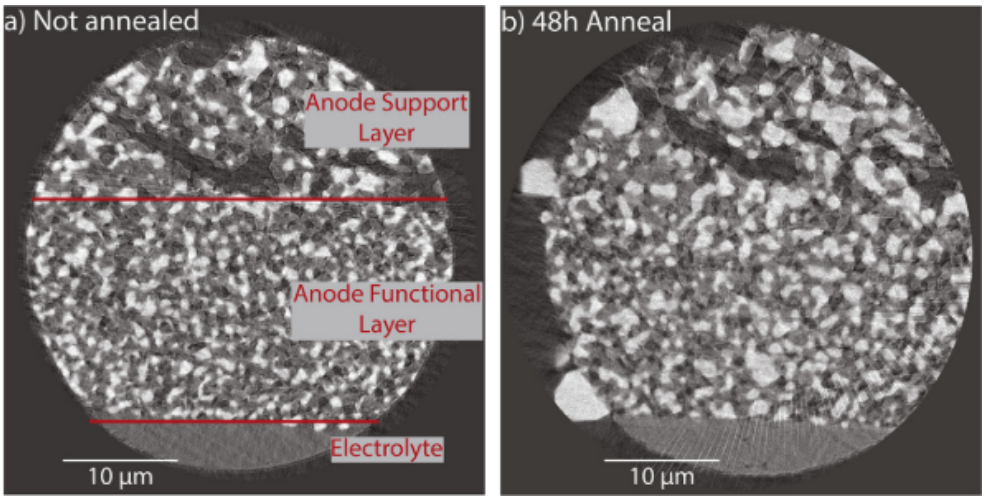


Figure 2.19: Side by side images of a reduced Ni/YSZ cermet (a) before annealing and (b) after 48 hours annealing at 1050 °C. Nickel is given by the white areas, YSZ by the gray, and porosity by the black [56].

is the focus of extensive research in the field of SOFCs and fuel cells in general.

Aluminum Titanate

A combination of aluminum and titanium oxides to form the Al_2TiO_5 stoichiometry, Aluminum Titanate (ALT) has been shown in recent studies to enhance the resiliency, both mechanically and electrochemically, of NiO-YSZ anode materials [1–6, 8, 9]. These effects have been attributed to the formation of several secondary phases when the constituents of ALT go into solution with the material components of the anode. At temperatures in excess of 800°C, ALT disassociates into Al_2O_3 and TiO. Subsequently, the alumina goes into solution with the nickel oxide to form a spinel structured nickel aluminate ($NiAl_2O_4$) while the titania forms a zirconium titanate superstructure ($Zr_5Ti_7O_{24}$) with zirconia from the YSZ [2]. Others suggest the titania may also go into solution with nickel oxide to form a nickel titanate ($NiTiO_3$) secondary phase [9]. According to the the above mentioned

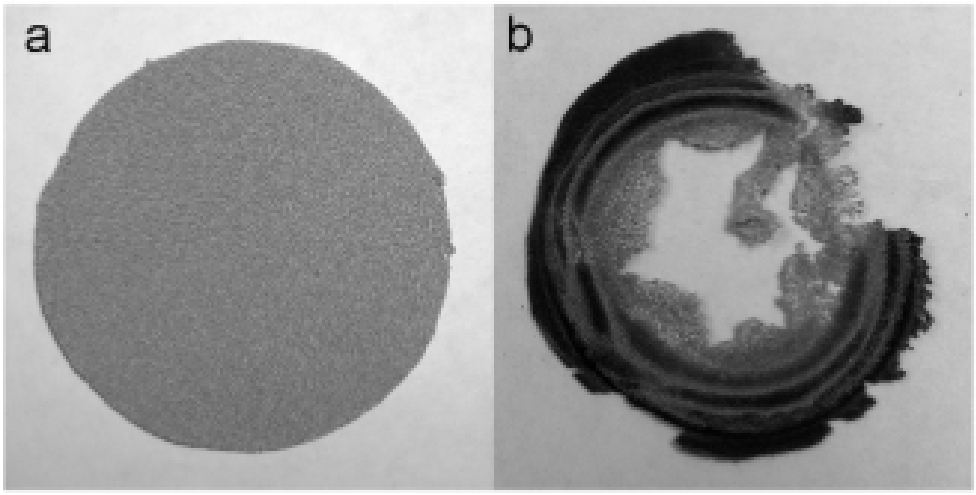


Figure 2.20: Open cell reticulated nickel metal foam used as an interconnect for fuel cell testing a) as prepared and b) after exposure to H_2S during testing [58]

studies, the formation of nickel aluminate in the NiO/YSZ anode system acts as a multi-functioning modifier: inhibiting agglomeration of nickel particles by Ostwald Ripening, enhancing reduction/oxidation resilience, and mitigating the collection of carbon on the surface of active sites. Additionally, zirconium titanate has been shown to enhance mechanical strength of these anode materials and may also exhibit mix electronic and ionic conduction (MEIC) behavior, as can be seen from the data in figures 2.16 and 2.17.

Initial investigation of the effects of ALT on nickel infiltrated YSZ scaffold SOFCs showed a marked decrease in the overall output of the cell but a significant increase in the longevity of the cell [1, 5, 6]. A separate study into the effects of alumina and tin doping of Ni/YSZ anode materials confirmed these findings [59]. Based on this, some mechanism associated with the introduction of alumina and/or titania to the system initially blocked active sites of the anode but ultimately reduced the rate of degradation over the lifetime of the cell. Further tests with both nickel infiltrated scaffolds and Ni/YSZ cermet anodes led to the discovery of the strange

reduction behavior of nickel aluminate. Under operating conditions (850 °C with highly reducing atmosphere) nickel aluminate reduces into nickel metal particles decorated with nano-sized alumina particulate. These particulates became the basis for a thermodynamic diffusion barrier acting by two simultaneous mechanisms. First, the alumina particles form a region that is considered to be immune to diffusion because it is impossible for the nickel to diffuse through the alumina. This forces any diffusing nickel atoms to travel the further distance around the boundary of the particle, slowing the process. Second, nickel atoms can only diffuse from the areas between the alumina decoration, eventually forming a concave region in the surface of the nickel particle. This region continues to recede until further diffusion would cause a significant increase in surface area, halting any additional mass transfer. Therefore, the alumina particles form a cage that not only slows the process of diffusion outward, but also causes Ostwald Ripening to result in thermodynamic equilibrium prior to the total absorption of nickel particles [2]. Thus, forming the basis of "diffusion caging". This mechanism is roughly depicted in figure 2.21

Other studies utilizing vibration RAMAN spectroscopy, a chemical analysis technique involving the interaction of monochromatic light on molecular bonds, have investigated the various additional degradation mechanisms that have afflicted SOFC anode materials. In reduction/oxidation studies with ALT doped Ni/YSZ cermet anodes, only moderate concentrations of ALT (about 4 wt%) were necessary to improve performance of redox cycled cells by 53% across 14 cycles [8]. Similar studies were used to investigate the coking behavior of ALT doped Ni/YSZ anode materials operating under methane. RAMAN experiments showed that ALT doped cells were subjected to a lower amount of carbon accumulation within the anode and were able to slough the carbon away with a simple cleansing oxidation to retain a greater percentage of maximum performance than undoped cells. These

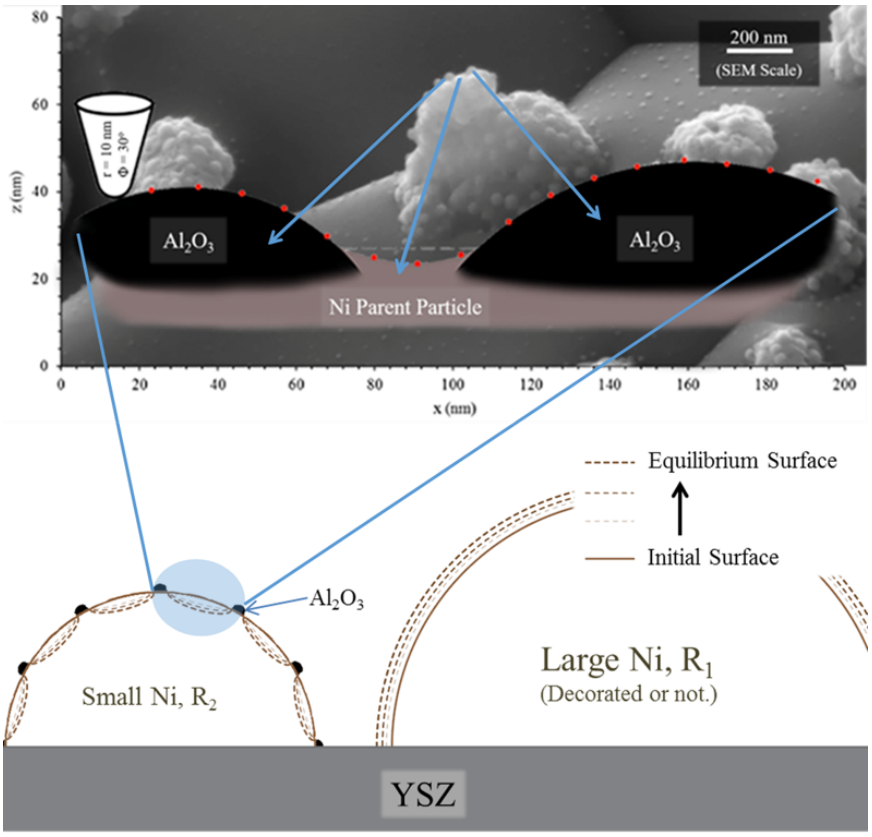


Figure 2.21: Schematic of diffusion caging mechanism with AFM overlay [60]

results were attributed to the inability of carbon adherence to alumina versus pure nickel metal as well as the assistance of MEIC behavior from the zirconium titanate superstructure [9].

The effects of ALT introduction to the Ni/YSZ anode system and its precursors materials (NiO/YSZ), have been investigated using modulus of rupture and indentation fracture resistance experiments described in the Anode Resiliency portion of section 2.2. The results from these experiments have shown consistent trends of continual mechanical property enhancement with increasing concentrations of ALT for both NiO/YSZ anode precursor materials, as well as operational Ni/YSZ cermets [4, 7]. However, after a number of redox cycles, as may be seen when a

SOFC power generation system goes offline, the samples underwent catastrophic degradation. When the same redox experiment was performed with pure alumina doped anode materials, destruction of the samples did not occur leading to the assumption that zirconium titanate was the culprit [7]. This is understandable when considering volumetric expansions of zirconia during phase changes from tetragonal to monoclinic structures.

Aluminate Spinels

Aluminate spinel structured oxides are a relatively new class of ceramic materials reported to possess thermal and chemical stability, moderate mechanical properties, refractory and magnetic behavior, and catalytic activity in various applications. These spinels are characterized by their AB_2O_4 stoichiometry where, for aluminate spinels in particular, A site cations are occupied by a transition metal (Ni, Co, Cu, etc.) or alkaline earth metal (Mg, Na, Li, etc.), and the B site is occupied by aluminum. The effects of the inclusion of nickel aluminates in Ni based SOFCs has been discussed extensively, but has also been shown to be an effective catalyst for phase reformation of glycerol [61]. Cobalt-based aluminate spinels have also been shown to be an active catalyst in glycerol phase reformation as well as an oxygen carrier catalyst for dry reforming of methane [62, 63]. Copper aluminate has been proven as catalysts for the oxidation of benzyl alcohol (as well as various other alcohols into olefins) and the degradation of various organic compounds [64, 65].

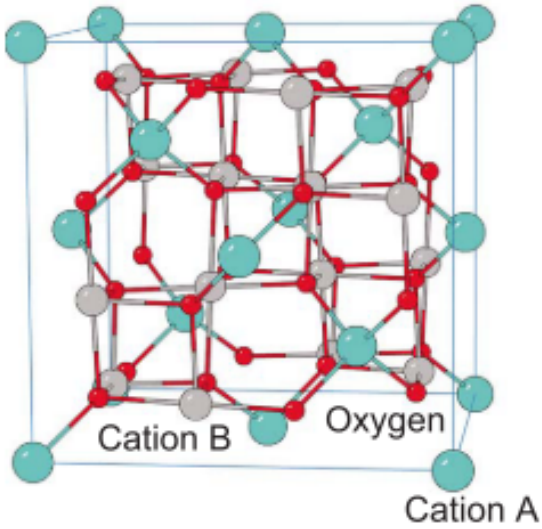


Figure 2.22: Atomic structure of an aluminate spinel where A site cations are occupied by a transition metal and B site cations are occupied by aluminum [66]

MOTIVATION

The primary functional modifier involved with the various enhancements discussed previously is believed to be a result of the formation of a secondary phase from the alumina dopant and the nickel oxide catalyst precursor of the anode. This combination results in a spinel structured oxide known as nickel aluminate and has been directly associated with the mitigation of various degradation mechanisms in the anode during operation. The experimentation reported herein hopes to elucidate the mechanisms by which ALT and its constituents affect anode resiliency by introducing it to various SOFC anode systems. This is completed in two phases. The first phase replaces the YSZ ceramic phase of the anode cermet with another commonly used ion conductor, GDC. The second phase focuses on the possibility of using similar dopant methods to increase viability of less commonly implemented electro-catalysts by utilizing aluminate spinels.

Replacing the YSZ ion conductor with GDC institutes various differences in the expected result of ALT doping, while nickel aluminate formation remains a primary outcome. This brings into question the role titanium plays in the doping scheme. Previously, titanium was expected to be forming a solid solution with zirconium from the YSZ, overall enhancing the mechanical properties of the anode. In the new system, without access to zirconium, titanium may form various secondary phases with the gadolinium or cerium from the GDC. How this effects the mechanical properties and electrochemical stability of the anode is pivotal in understanding the enhancements of ALT doping and the necessity of titanium in this doping scheme. Additionally, aluminum from the ALT may also form secondary phases with the constituents of GDC. If this is the case, it could determine the viability of doping GDC based anode systems with ALT. These aspects were explored using indentation fracture

toughness measurements to estimate mechanical strength and various electrochemical performance and degradation experiments to elucidate operational mechanisms.

The secondary objective of this research involves the investigation of the aluminate spinel class of ceramic oxides as potential replacement of the metal electrocatalyst in SOFC anodes. Until recently, these materials have primarily been used as pigments in dyes and for various optical emission applications. However, as has been shown extensively for the case of nickel aluminate, these spinels also appear to possess interesting thermal and catalytic properties. In addition to nickel, two other SOFC catalysts are known to readily form aluminate spinels: copper and cobalt. Evaluation of the synthesis methods and reduction behavior of these two spinel materials should elucidate the practicality of implementation into respective SOFC anode systems with the ultimate goal of producing technology that could potentially compete with nickel based anodes. Similarities between these aluminate spinels and nickel aluminate were identified by indirectly observing operational reduction phenomena visually and using SEM imaging techniques.

EXPERIMENTAL METHODS

Materials

The types of materials used during the following experiments include: Ceramic powders, metallic salts, surfactants, polymer-based binders and plasticizers, and a number of different solvents. All products were used as supplied unless otherwise noted.

Ceramic Powders

Ceramic powders are the building blocks of the components used in the following experiments and come in a multitude of compositions, sizes, and shapes. The powders used herein include: Nickel Oxide (NiO, Alfa Aesar), Copper Oxide (CuO, Alfa Aesar), spinel structured Cobalt Oxide (Co_3O_4, Advanced Materials), α-alumina (Al_2O_3, Inframat) Yttria stabilized Zirconia (YSZ, Tosoh Corp.), Gadolinium doped Ceria (GDC, Fuel Cell Materials), and Lanthanum Strontium Manganite (LSM, Fuel Cell Materials).

Metallic Salts

Metallic salts are metal cations dissolved in an acid or base to form a soluble crystal. These salts are especially useful in producing pure ceramic compounds when used as a component in either co-precipitation or combustion synthesis methods. The metallic salts used in the following experiments include: Aluminum Nitrate ($Al(NO_3)_3$, Alfa Aesar), Titanium Ammonia Lactate (Alfa Aesar), Copper Nitrate ($Cu(NO_3)_2$, Alfa Aesar), and Cobalt Nitrate ($Co(NO_3)_2$, Alfa Aesar).

Surfactants

Surface active agents, or surfactants for short, are additives that influence the various ways that particles act while in solution. Depending on the type of surfactant used, they may alter surface energy, charge, or tension; or assist in particle dispersion or stabilization. The surfactants used in the following experiments are the two dispersing agents KD-1 (TCW Inc.) and Darvan C-N (Bayville Chemical Supply Inc.). Two different dispersing agents are necessary to cover all solvents used in the experiments. Darvan C-N is used to disperse particles in aqueous solutions while KD-1 is needed to disperse particles in non-polar solvents.

Binders and Plasticizers

Prior to sintering, ceramic compacts are incredibly fragile due to the lack of inter-connectivity between particles. This lack of structural integrity often results in failure of the sample during handling in the "green" state. Polymer-based binders and plasticizers are used to ameliorate this issue. Long polymer chain binders are introduced to ceramic slurries to effectively lock the individual particles in place upon drying, allowing the part to be handled more extensively. Shorter chain polymers are included to increase the flexibility of the ceramic compact. The binders and plasticizers used in the following experiments include: 200 and 20000 MW polyethylene glycol (PEG, Alfa Aesar), Polyvinyl Butyral (B98, TCW Inc.), and Butyl Benzyl Phthalate (S-160, TCW Inc.).

Solvents

Every solution contains two parts: the solute and the solvent. For the solutions used in the following experiments, the solute is almost exclusively ceramic powders, however, the solvent used will be varied based on the application. Three solvents

will be used herein: Deionized water (DI water), ethanol, and xylol. DI water has undergone specialized processing to remove any contaminates. This ultra-pure water is useful in scientific processes where even the smallest contamination may skew results. Ethanol is a non-polar solvent with a high vapor pressure allowing it to be rapidly evaporated, even at room temperature. Xylol, another non-polar solvent, is primarily used to stabilize ethanol-based solutions, reducing their propensity to volatilize during storage.

Fuel Cell Manufacturing

The electrochemical experiments discussed in section 4.3 involve the operation of electrolyte-supported SOFCs (ESCs). Fabrication of an ESC is a multi-step process involving the layering of several components and subsequent heat treatments. The processing of a single batch of cells may take 2-3 days. First, an anode solution was airbrushed onto a commercial YSZ electrolyte wafer (Fuel Cell Materials) and sintered. The anode was infiltrated using one of the two dopant solutions and heat treated to form the necessary secondary phases. Finally, the cathode was airbrushed onto the blank side of the electrolyte wafer and sintered.

Electrode Processing

The solutions used to produce the two electrodes are based around the reaction that must occur in that particular electrode. The primary function of the anode is the oxidation of the fuel and collection of electrons. For this, a ceramic-metal composite composed of GDC and nickel metal was chosen, however, metallic materials are difficult to process simultaneously with ceramic materials. To avoid this issue, Nickel oxide was used as a precursor material as the oxide will reduce under normal fuel cell operating conditions. The cathode, on the other hand, must also conduct

ions and electrons just as the anode does, but it must also reduce oxygen while remaining stable in a highly oxidizing environment. The latter constraint excludes all electronically conducting metals and due to their lack of electronic conductivity, most oxides are also eliminated. Instead, an engineered ceramic known as a perovskite was chosen. Perovskite structured ceramics contain multiple transition metal cations, each at different valence states. This gives the bulk material mixed electronic and ionic conductance (MEICs). Many different perovskites are used as cathode materials, but for the following experiments LSM was chosen as the primary component. YSZ was also included in the cathode mixture in order to provide extra ionic conductivity and to form a strong bond with the electrolyte.

To produce a high functioning fuel cell, the active area of the electrodes must be optimized. The active area of the anode is governed by the total effective area of TPB. The TPB is made of ion conductor, electron conductor, and fuel. In this system the ion conductor is GDC, the electron conductor is nickel metal, and the fuel is provided through open porosity. Therefore, to optimize the area of TPB, the anode solution must result an equal volume ratio of nickel metal, YSZ, and pore former after reduction during operation. This results in a solution of 62 w% nickel oxide, 33 w% GDC, and 5 w% pore former (in this case corn starch). The cathodic reaction is less dependent on total active area and primarily requires LSM active sites for the reduction of oxygen to occur as well as a direct ionically conducting network for the transport of oxygen ions to the electrolyte. Therefore, a solution of 47.5 w% LSM, 47.5 w% YSZ, and 5 w% pore former was chosen.

The electrode slurries were made by first dissolving 1 w% KD-1 dispersant in a mixture of 35 w% of both ethanol and xylol (weight percent is based on total mass of powder). Each of the above powders were added individually to the solvent mixture and ultrasonically mixed using a Branson Sonifier 450. Once fully mixed, 1.5 w%

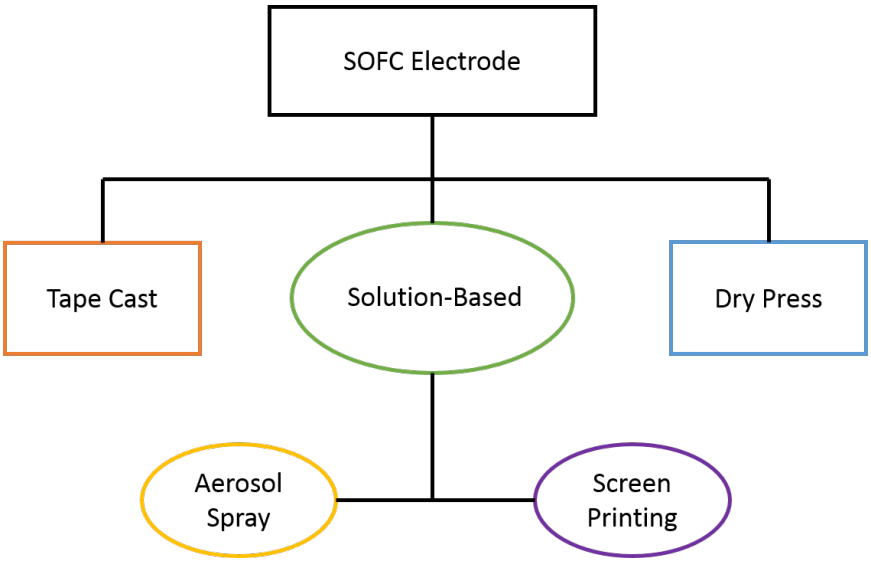


Figure 4.1: Block diagram of the possible electrode processing methods

Butyl Benzyl Phthalate, 2 w% PEG-200, and 3 w% Polyvinyl Butyral were added to the solution and well mixed. With all components in solution, between 5 and 10 small, cylindrical and spherical YSZ milling media were added to the slurry and placed on a rotary ball mill for 48 hours. The ball milling process is primarily used to reduce particle size in a slurry but with the small amount of milling media used in this case, mixing was the primary outcome.

The electrodes were applied via an airbrushing technique using a Badger Model 105 handheld airbrush. First, a 1 inch circular template was adhered to one side of a YSZ electrolyte wafer. A thin layer of the electrode solution was sprayed at about 25 psi air pressure. The resulting particle deposition was dried using the compressed air from the airbrush. These two steps were repeated at various angles until the entire surface of the electrolyte, within the template, was covered with electrode solution. If performed correctly, this technique should result in electrodes with a thickness between 30 and 50 μm. The finished electrodes were left to dry for 3 hours before being sintered.

Predetermined deleterious interactions occur within this fuel cell system that forces a certain order of operations to be applied. Specifically this interaction occurs between the Lanthanum in the LSM cathode component and the YSZ of the electrolyte. At 1100 °C a perovskite secondary phase begins to form called Lanthanum Zirconate [67]. This material possesses excellent mechanical and thermal properties but significantly inhibits ionic conductivity. To avoid this formation, the cathode was sintered at a much lower temperature than the anode, and therefore, was applied and sintered last. The anode must be sintered at a minimum of 1200 °C, dictated primarily by the nickel oxide. For the following studies, the anode was sintered at 1250 °C for 2 hours in air at heating and cooling rates of 10 °C/min and the cathode was sintered at 1000 °C for two hours in air with the same heating and cooling rates.

Infiltration

Manufacturing a doped fuel cell adds one additional processing step and one additional heat treatment. The process also requires that the mass of the electrolyte and the anode are known. This was done by weighing the electrolyte wafer prior to spraying the anode and subsequently weighing the anodic half cell after sintering. Dopant solutions were produced by first dissolving an adequate amount of aluminum nitrate in DI water to form a 0.1 molarity solution. This forms the alumina dopant solution. A second solution was formed by diluting ammonium titanium lactate with DI water to a molarity of 0.05. The mixing of this solution with the 0.1 M aluminum nitrate solution forms a stoichiometric solution of aluminum titanate. Using a dropper, one of the two solutions was applied to the anode one drop at a time and allowed to fully dry. When the anode was visibly dry, the cell was placed in a box furnace at 400 °C for 30 to 60 seconds to remove any remaining organics. These two steps were repeated until the desired concentration of dopant was reached.

To form the desired secondary phases, the half cell was heat treated in air at 1400 °C for 1 hour with heating rate of 5 °C/min and cooling rate of 10 °C/min.

Fuel Cell Testing

The fuel cells produced by the methods described in the previous section were tested using an in-house planar SOFC test rig operated by a LABView program. The test rig is composed of a clamshell furnace modified with two hollow inconel platens which are used to simultaneously collect current from the system and supply gases to the electrodes. The platens are connected to a DC power supply (6651A #J01, Agilent) and a DC load generator (N3301A, Agilent) which simulate the applied load and measure outputs from the cell. The gases (hydrogen, nitrogen, and air) are individually controlled via a series of flow controllers (Flo Controller, MKS) and can be directly adjusted using inputs within the LABView program. During operation, each platen supplies a different gas which dictates the directionality of the cell. The top platen was supplied with nitrogen and hydrogen (anode side), and the bottom platen was supplied with dry air (cathode side).

To load a fuel cell for testing, a silver wire screen (Alfa Aesar) was applied to the surface of the bottom platen with a thick slurry of silver oxide powder dispersed in xylol using KD-1 dispersant. During ramp up, this silver oxide paste reduces to silver metal to form an electronic interconnect between the platen and the silver screen. The silver oxide paste was then gently painted to the surface of both fuel cell electrodes and the cell was place cathode side down on the silver mesh. Finally, a foamed nickel metal mesh was cut to the size and shape of the anode and painted with silver paste. The nickel mesh (Alfa Aesar) was placed on the surface of the anode and the top platen was used to sandwich the three components. Figure 4.2 gives a visual of this setup.

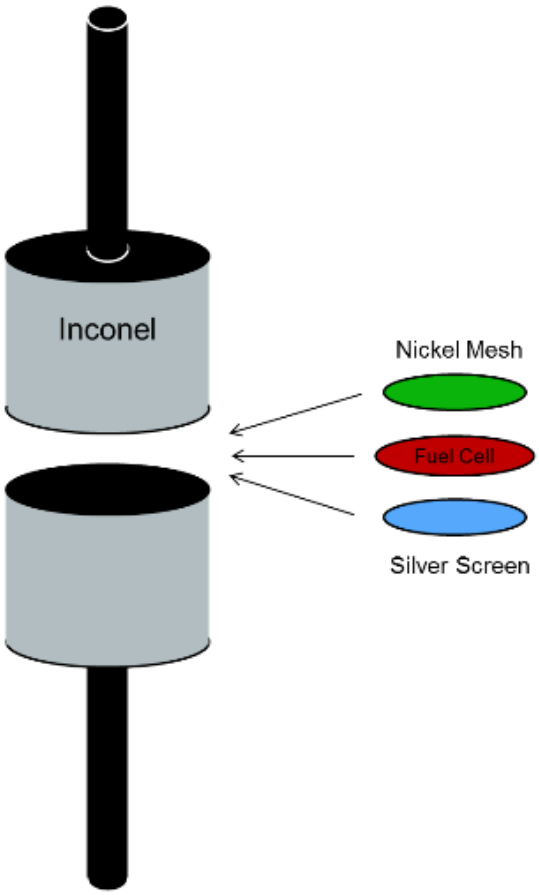


Figure 4.2: Schematic of components used for fuel cell testing

With the components in place, the clamshell furnace was closed and heated to 850 °C at a rate of 5 °C/min. During ramp, the LABView program was initiated and nitrogen was flowed over the anode at a rate of 50 sccm to prime the cell. The reducing environment produced by this flow initializes the reduction of the nickel oxide, however, full reduction does not occur until hydrogen is introduced. During this time, the applied load was set to 1.2 V. This potential is greater than the theoretical open-circuit voltage (OCV) of the fuel cell, therefore, the system will remain in equilibrium during ramp. Once at max temperature, air and hydrogen

were flowed over the respective electrodes starting at rates of 25 sccm and increasing in 25 sccm increments every few minutes to a maximum flow rate of 100 sccm. After a few moments at max flow rates, OCV approaches the theoretical threshold for the oxidation of hydrogen (about 1.13 V). In most cases, the cell does not reach this threshold and the OCV achieved is recorded as a measure of performance. Once operating at peak OCV, an overpotential of 0.5 V was applied to the system (relating to a generated load of 0.7 V) and after approximately 30 minutes the system will reach maximum performance. From this point, either a performance or a degradation experiment can be performed. The microstructures of select samples were investigated using field emission scanning electron microscopy (FESEM) after testing.

Performance

The performance of a fuel cell is based on a few factors: max open circuit voltage, max current output, and max power production. Generally, the greater the OCV of the cell the greater the output and so, OCV is usually overshadowed by the current and power generation metrics. To measure these aspects of the cell, a scan over the range of achievable voltage potentials was performed. This is known as a VI scan. Starting from the point left off in the previous section, the applied overpotential was reduced to zero, returning the cell to OCV. Then, the applied overpotential was increased in increments of 0.1 V. At each increment, the output was allowed to equilibrate over a period of 30 seconds. VI scans were performed at peak cell performance and after 24-hour operation at an overpotential of 0.5 V.

Degradation

To measure degradation, the cell was held at the operating conditions noted previously for 24 hours. This data was then analyzed using a MATLab algorithm designed specifically for this application. The algorithm fits either an arctangent

function or a logistics function to the degradation data, depending on the overall shape of the curve. The algorithm then takes the derivative of the curve fit function. Using this derivative, the algorithm calculates the rate of degradation of the cell for every five hours of data.

Fracture Resistance Measurement

Sample Preparation

Anode material powders were produced using a solid-state mixing method. Nickel oxide, GDC, and appropriate amounts of homemade ALT powder or alumina were dispersed in DI water using 1 w% Darvan C-N (based on powder mass) to produce the anode compositions described in section 4.2 earlier in this chapter with 5 w% and 10 w% additions of ALT and alumina. YSZ milling media were introduced to the slurry and the solution was mixed on a rotary ball mill for 48 hours. The combination of the ultra-hard milling media and the rotational motion causes the ceramic powder to be ground down into smaller particles and ensures close integration of all components [7]. After ball milling, the slurry was flash-frozen using liquid nitrogen and placed in a Virtis Advantage vacuum freeze dryer. The pressure in the chamber was reduced below the triple point of water and the temperature was increased to 50 °C. Over the next 48 hours the water in the slurry was sublimated out of the system leaving a thoroughly mixed powder containing all components.

0.5 grams of each of the five powders were uniaxially pressed in a 1/2 inch die to 250 MPa and sintered to 1400 °C for 1 hour with heating and cooling rates of 5 °C/min. The resulting sample pellets were hand polished on a Buehler Ecomet 3 polishing wheel using silicon carbide sandpaper at grits between 260 and 1200.

Microhardness Testing

Polished sample pellets were tested using a Leco LM 700AT microhardness tester utilizing a pyramid diamond indenter. First, an indentation was made and the resultant hardness was recorded. The indentation should cause several cracks to propagate from the corners of the indentation. If this does not occur, greater force is required for the indentation. The lengths of the cracks formed were measured and recorded. Cracks propagating from the sides of the indentation were not recorded.

Aluminate Spinel Synthesis and Characterization

Two methods were utilized in an attempt to produce phase pure cobalt aluminate and copper aluminate powders: solid-state mixing (described in the previous section) and Co-precipitation. In a solid state process, pure oxides of the materials required to form the desired stoichiometry are mixed thoroughly and heat-treated to form the new phase. Co-Precipitation involves the mixing of dissolved metallic salts in the correct stoichiometries, drying the resulting liquid, calcining to precipitate the metal cations (in the form of oxides), and a final heat treatment to form the new phase. X-ray diffraction (XRD) was performed on completed powders to verify phase purity and compare particle size between synthesis methods. Thermogravimetric analysis was also employed to understand the materials' reduction kinetics and catalytic activity along with simultaneous differential thermal analysis (DTA) and mass spectroscopy.

Synthesis

Solid-State Synthesis In the solid-state method, adequate amounts of α-alumina and the appropriate transition metal oxide were dispersed in DI water using 1 w% Darvan C-N (based on powder mass). YSZ milling media were introduced to the slurry and the solution was mixed on a rotary ball mill for 48 hours [68]. After

ball milling, the slurry was flash-frozen using liquid nitrogen and placed in a Virtis Advantage vacuum freeze dryer. The pressure in the chamber was reduced below the triple point of water and the temperature was increased to 50 °C. Over the next 48 hours, the water in the slurry was sublimated out of the system leaving a closely related powder of the transition metal oxide and alumina. After hand grinding to remove large chunks, the freeze-dried powders were heat-treated in air at various temperatures between 900 °C and 1100 °C at increments of 50° for dwell times of 6 hours.

Co-Precipitation Synthesis For the co-precipitation method, adequate amounts of aluminum nitrate, copper nitrate, and cobalt nitrate metallic salts were dissolved in ethanol and combined to form the proper stoichiometries for the final materials. The well-mixed solutions were dried in air at 80 °C for 48 hrs. The resulting solids were then calcined at 500 °C for 6 hours in air to fully remove all organic constituents (primarily nitric acid) and precipitate the alumina and desired transition metal oxide [69]. The calcined ashes were hand ground to reduce particle size and heat-treated in air at various temperatures between 650 °C and 950 °C at increments of 50° for dwell times of 6 hours.

Characterization

The crystal structures of the calcined powders synthesized by the processes described above were analyzed by powder X-ray diffraction (Scintag Inc.). Scans were taken over 2θ values of 10 to 80 degrees with step sizes of 0.02 degrees and scan speeds of 4 s. The resulting diffraction patterns were analyzed using MDI JADE software with access to relevant crystallographic databases. Powders exhibiting impurities above the detection limit of the equipment (>3 w%) were excluded from further investigation.

To investigate reduction characteristics, phase pure powders were combined with their appropriate oxides (CuO for copper aluminate and Co_3O_4 for cobalt aluminate) to form an equal volume mixture. Each mixture was then dispersed in ethanol using KD-1 and ball milled for 24 hours. Slurries were subsequently dried in air at 85 °C and hand ground to reduce particle size. 0.5 grams of each of the chosen pure aluminate, pure oxide, and equal volume mixture powders were uniaxially pressed in a 1/2 inch die to 250 MPa. The resulting compacts were measured geometrically to obtain a green density. The six samples were then heat-treated to 850 °C under a reducing atmosphere (Forming gas: 5% hydrogen/95% Argon) for 12 hours using a Lindberg Blue tube furnace equipped with a 1-inch diameter quartz tube. Heat-treated samples were visually inspected and measured geometrically to determine physical changes in the material. The fracture surfaces of select samples were investigated using FESEM.

RESULTS AND DISCUSSION

NiO/GDC Anode System

Hardness and Fracture Resistance

The strength of SOFC support materials is important to design robust devices that can withstand the stresses caused by extreme thermal conditions and clamping within stacks. This is particularly pertinent for anode precursor materials used in ASC where all loads are being carried by brittle ceramic materials. Indentation fracture resistance (K_{ifr}) has recently been showed to accurately predict trends in mechanical properties with non-destructive testing [54], and has been specifically proven to be a viable metric for the mechanical strength in the NiO/YSZ anode system [7]. Table 5.1 gives averaged values for results of fracture resistance experimentation on NiO/GDC anode precursor materials. From this data, it would seem there is

Table 5.1: Average values for Vicker's hardness, crack length and K_{ifr} for ALT and Alumina doped NiO/GDC anode precursor materials.

		Hardness (HV)	Crack Length (μm)	Indentation Fracture Resistance (MPa$\sqrt{m}$)
	Control	853.2	85.6	12.5
ALT	5w%	824.4	87.1	11.6
	10w%	851	73.1	14.6
Al2O3	5w%	982.3	74.5	17.5
	10w%	1097.4	61.8	20.0

little effect of ALT doping of these anode materials. This confirms the previous

theories of mechanical strength enhancement attributed to a solid solution between zirconia and titanium in the Ni/YSZ anode system. Alumina doping, on the other hand, shows excellent strength enhancement, increasing 40% with only 5 w% alumina concentration and another 20% at 10 w% dopant concentration. These results far exceed those collected by Kent, McCleary et al. and Driscoll et al. for ALT doped NiO/YSZ anode precursors, shown in figure 2.17 [3, 4, 7]. It should be noted that all fracture resistance values were calculated from equation (2.9)a. If equation (2.9)b. is used, values generated are approximately 15% higher, as was reported by Quinn [54].

Looking at this data from a compositional perspective, 5 w% ALT contains 2.8 w% alumina and 10 w% ALT contains 5.6 w% alumina. Since low concentrations of ALT appear to be deleterious to the strength of this system and pure alumina doping has the opposite effect, titanium is hypothesized to be the culprit. The slight enhancement at 10 w% ALT (5.6 w% alumina concentration) suggests these adverse effects are not cumulative and can be overcome by the enhancement from alumina when the concentration of aluminum exceeds a certain threshold. It is possible, but unlikely, that extraneous titanium oxide dispersed through the system would exhibit a pronounced detrimental effect, therefore, titanium-based secondary phases must be the issue. Titanium is known to form several phases with the materials present in the system. Nickel titanate ($NiTiO_3$, NT) has been suggested as a possible participant in the enhancement of the carbon coking resistance of Ni/YSZ anodes [9]. This material has been proven as an effective solid lubricant, possesses advantageous electrical and catalytic properties, and is reported to have high hardness (940 HV) relative to ceramic materials [70]. Gadolinium titanate ($Gd_2Ti_2O_7$, GT) pyrocholre structure has been shown to exhibit MEIC properties and displays a sintering aid effect on GDC [71, 72]. Enhanced densification of the GDC structure should, by extension, increase the rigidity and strength of the system. The densification of the

GDC structure would also result in a more continuous network, better facilitating the transfer of electrons and ions. Brannerite phase cerium titanate ($CeTi_2O_6$, CT), a material scrutinized for optical applications, is also known to form under anode processing conditions, but its mechanical properties have not been studied extensively [73].

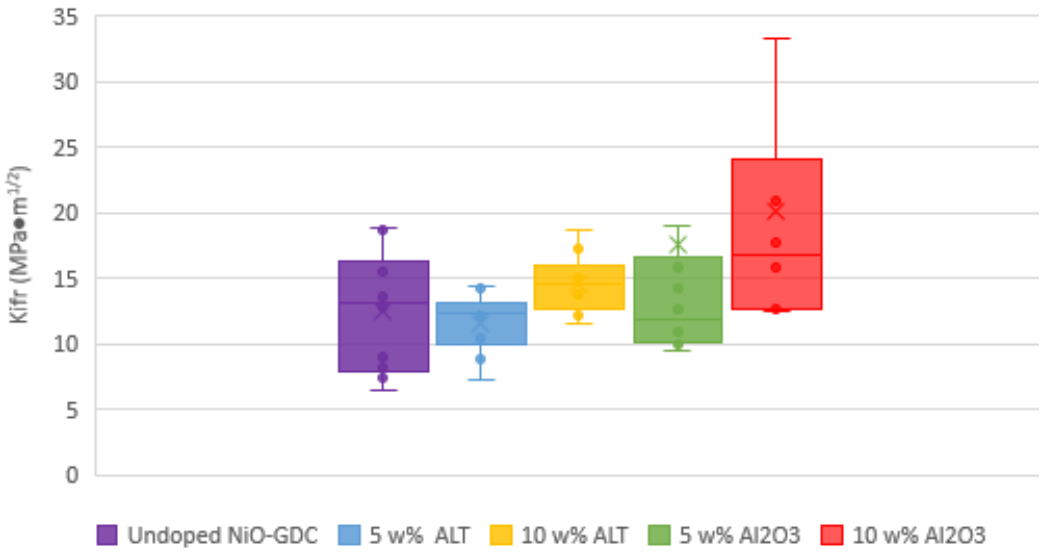


Figure 5.1: Statistical distributions of K_{ifr} calculated by equation (2.9)a. for ALT and alumina doped NiO/GDC anode precursor materials.

Figure 5.1 represents the statistical analysis of indentation fracture resistance experiments. This information depicts the variance in strength across each of the five samples. Despite the average of the control exceeding that of the 5 w% ALT sample, the deviation of the results from the control span the deviations of both the 5 and 10 w% ALT samples. Therefore, aside from overall consistency across the sample, ALT doping does very little to enhance the strength of this anode system, revealing a significant deviation from what has been observed in the Ni/YSZ system [3, 4, 7]. Looking at the alumina results shows a significant increase in deviation of results. This suggests the effects of alumina doping are highly localized.

Electrochemistry

Degradation The rapid degradation of SOFC anodes due to Ostwald Ripening is the largest contributor to their lack of use in major power generation applications, particularly for ultrafine, high surface area nickel particles. Current anode materials require stack replacements every 4000 to 10000 hours. This makes SOFC technologies almost 10 times more expensive than wind, solar, or fossil fuel combustion, despite greater efficiencies [33]. The degradation experiments described herein may seem minuscule compared to life cycles of thousands of hours, but initial effects within the first 24 hours effectively set the stage for the remainder of the life of the cell. These degradation results were calculated based on the derivative of the curve fit for data collected over 24 hours of cell operation at 0.5V overpotential. All calculations were performed using a MATLab algorithm developed and published by Dr. Clay Hunt and co-authored by M. Zachariasen [6].

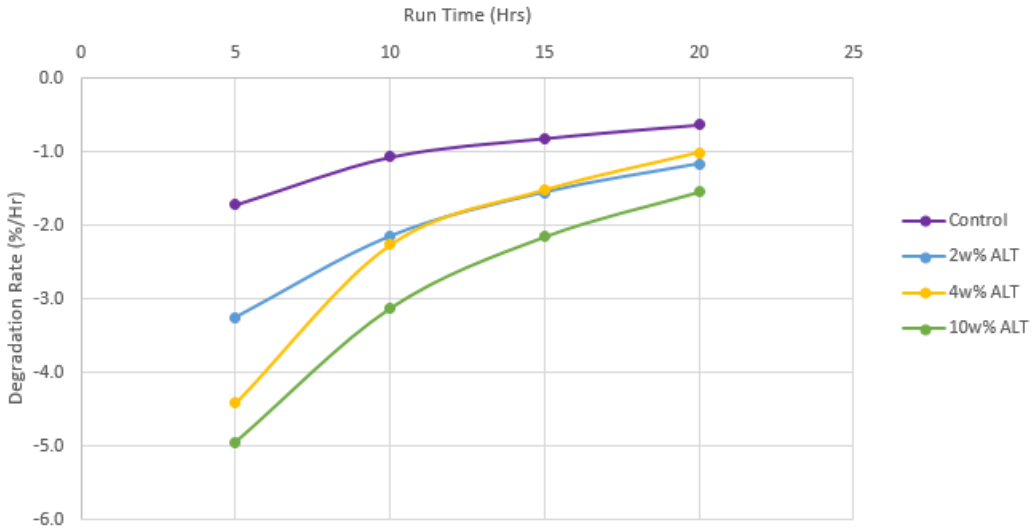


Figure 5.2: Degradation of 2, 4, and 10 w% ALT doped Ni/GDC anode SOFCs over 20 hours of operation at 0.5V overpotential.

ALT doped Ni/GDC anodes degrade almost 100% faster in the first 24 hours

than an undoped cells of the same composition, as shown in figure 5.2. The rapid degeneration of the cell is attributed to deleterious interactions between titanium and GDC, ultimately inhibiting ionic conduction. The formation of GT would be expected to reduce the ionic conductivity of the GDC because of depletion of gadolinium in the lattice which are needed for oxygen ion transport. However, considering its MEIC behavior, GT should act as a proxy for both ion and electron conduction, even compensating for loss of active area due to agglomeration of nickel particles. A similar effect would be observed for the formation of NT. The formation of CT is more fitting for the degradation behavior observed. CT possess no conductive properties, such that the formation of CT would in fact decrease the ionic conductivity of the cell. This, in turn, causes a substantial reduction in the active area of the anode. As the nickel coarsens, the few active sites that do exist are more quickly absorbed and cut off from necessary fuel. A similar effect would be observed if pure titanium oxide remains in the system, effectively blocking active sites. These mechanisms are demonstrated schematically in figure 5.9.

Based on the observed performance losses and mechanical strength with titanium in the Ni/GDC anode system, pure alumina doping was also investigated in this system. Degradation tests shown in figure 5.3 reveals that trace amounts of alumina reduce the rate at which the cell degrades but further doping shows no appreciable benefits. This effect is most evident during the first 15 hours of operation. By the end of the 20-hour run, cell of each concentration of alumina (including the control) reach approximately the same rate of degradation. However, since each of the other cells degenerated rapidly for the first 10 hours, the 1 w% cell retained a more significant portion of its initial performance. With alumina as the only additive to the system, nickel aluminate formation, and eventual reduction during operation, is the hypothesized mechanism behind the slowing of anode degradation. A

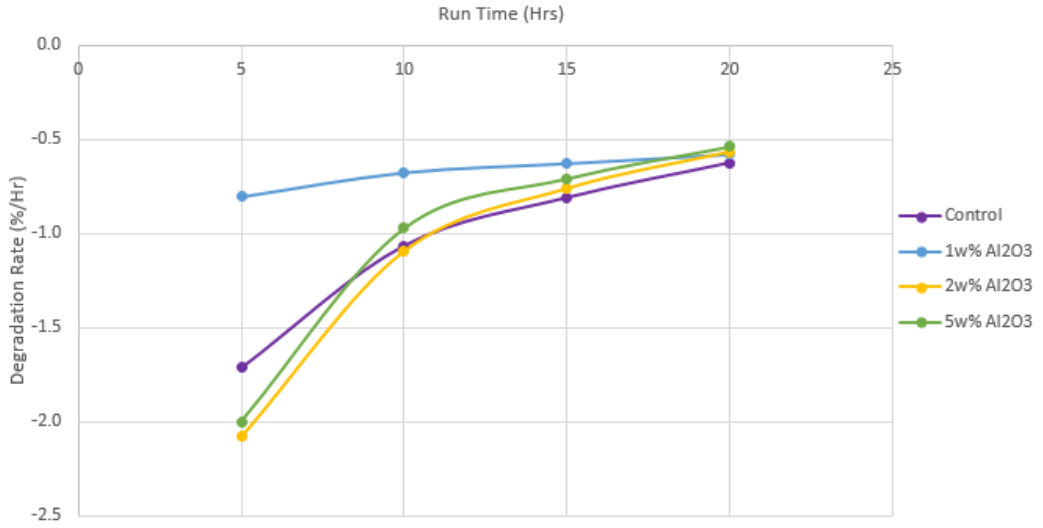


Figure 5.3: Degradation of 1, 2, and 5 w% alumina doped Ni/GDC anode SOFCs over 20 hours of operation at 0.5V overpotential.

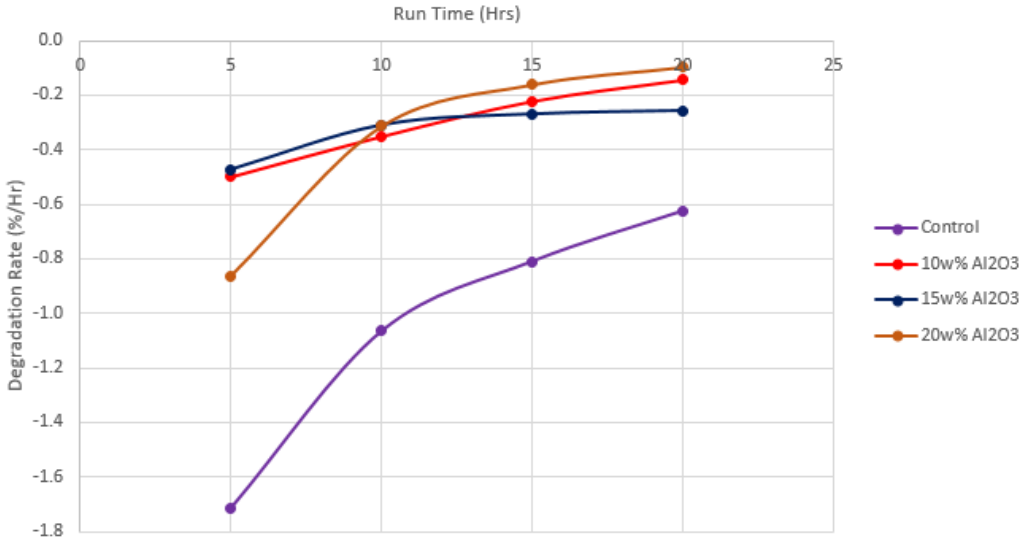


Figure 5.4: Degradation of 10, 15, and 20 w% alumina doped Ni/GDC anode SOFCs over 20 hours of operation at 0.5V overpotential.

cerium aluminate perovskite structure has been reported to form at similar processing temperatures, but full formation of the phase required several days of heat treatment [74]. It is unlikely that the material had formed during the two hours of processing

at 1400 °C. Increasing the concentration of alumina in the cell to the point of being a distinct component (>10 w%) more significantly enhances the resiliency of these anodes as shown in figure 5.4. In all cases and throughout the entire 20 hours of operation, the control cell degraded at double the rate as the doped samples. In addition, all of the doped cells finished the run below 0.25% degradation per hour. Unfortunately, this resiliency enhancement comes at a significant performance cost, as explained in the next section.

Performance Analysis of the degradation of SOFCs is pertinent to lengthening their overall lifetime, but often times this effect is a trade off with performance. Including additional components to the anode increases the probability that active sites are blocked, effectively reducing the concentration of TPB available to facilitate the required reaction. It is important to evaluate both degradation and performance capabilities when introducing new materials to the system.

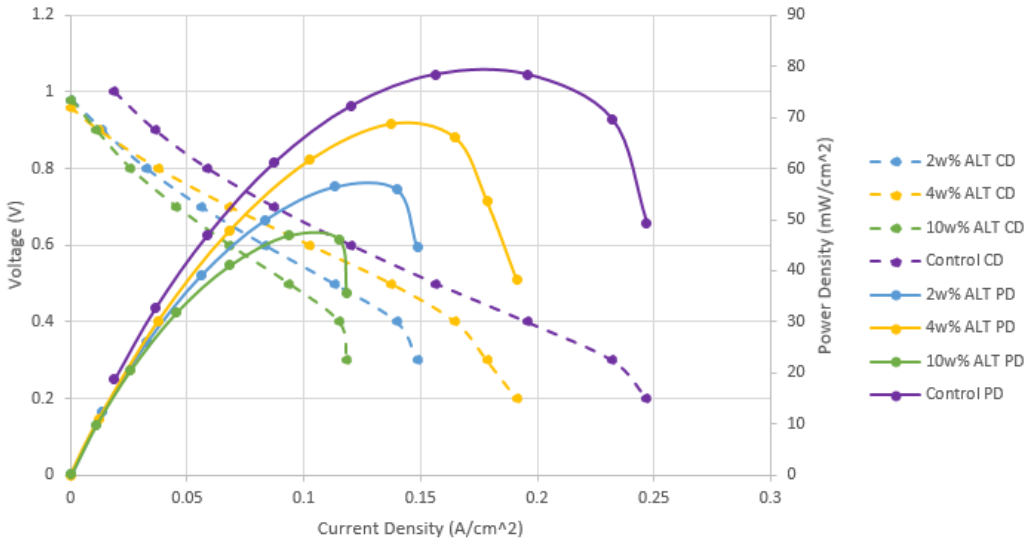


Figure 5.5: Power density (solid) and current density (dashed) curves for 2, 4, and 10 w% ALT doped Ni/GDC anode SOFCs. Curves are based on V-I scans taken at peak performance of each cell's operation.

As with mechanical strength and rate of degradation for these materials, ALT additions appear to be harmful to the performance of this anode system in any concentration, deviating again from what was seen in the doped Ni/YSZ system [5,6]. This is represented by both initial power density and current density shown in figure 5.5. In general, ALT doped cells produced approximately 50% less power than control cells of identical construction. For comparison, 80W of power is required to run an incandescent light bulb. Evaluating the polarization curve (represented by the current density function), none of the ALT doped cells were capable of generating current at a potential of 1 volt (near OCV). This gives the illusion of having low capacitive loses when compared to the example polarization curve given in figure 2.3. In actuality, if these curves were extended to initial OCV limits, extreme losses would be evident in this region. Varying degrees of ohmic losses are observed across the three concentrations of ALT doping with 10w% exhibiting the greatest losses and 4w% showing a more comparable slope to the control cells. This suggests a drop in anode electronic conductance, backing up the theory of CT formation in the system. All cells exhibited unresolved transport losses. After a 24 hour degradation period, two consecutive scans were performed. The results of these scans are shown in figure 5.6 and reveal two distinct phenomena. During the first scan, it was discovered that transport was only minimally inhibiting the reaction and overpotentials nearing 100% OCV could be achieved without excessive losses. This is represented by what seems to be two separate ohmic loss regions in the polarization curve. As these high overpotentials were applied, the cells recovered nearly 100% of the performance lost during the 24 hours of operation, as shown in the second scan. The performance during the first scan proves that the TPB network had almost completely deteriorated over the 24 hour operation period and, by a mechanism not understood or observed in the ALT doped Ni/YSZ anode system, peak performance is returned with little

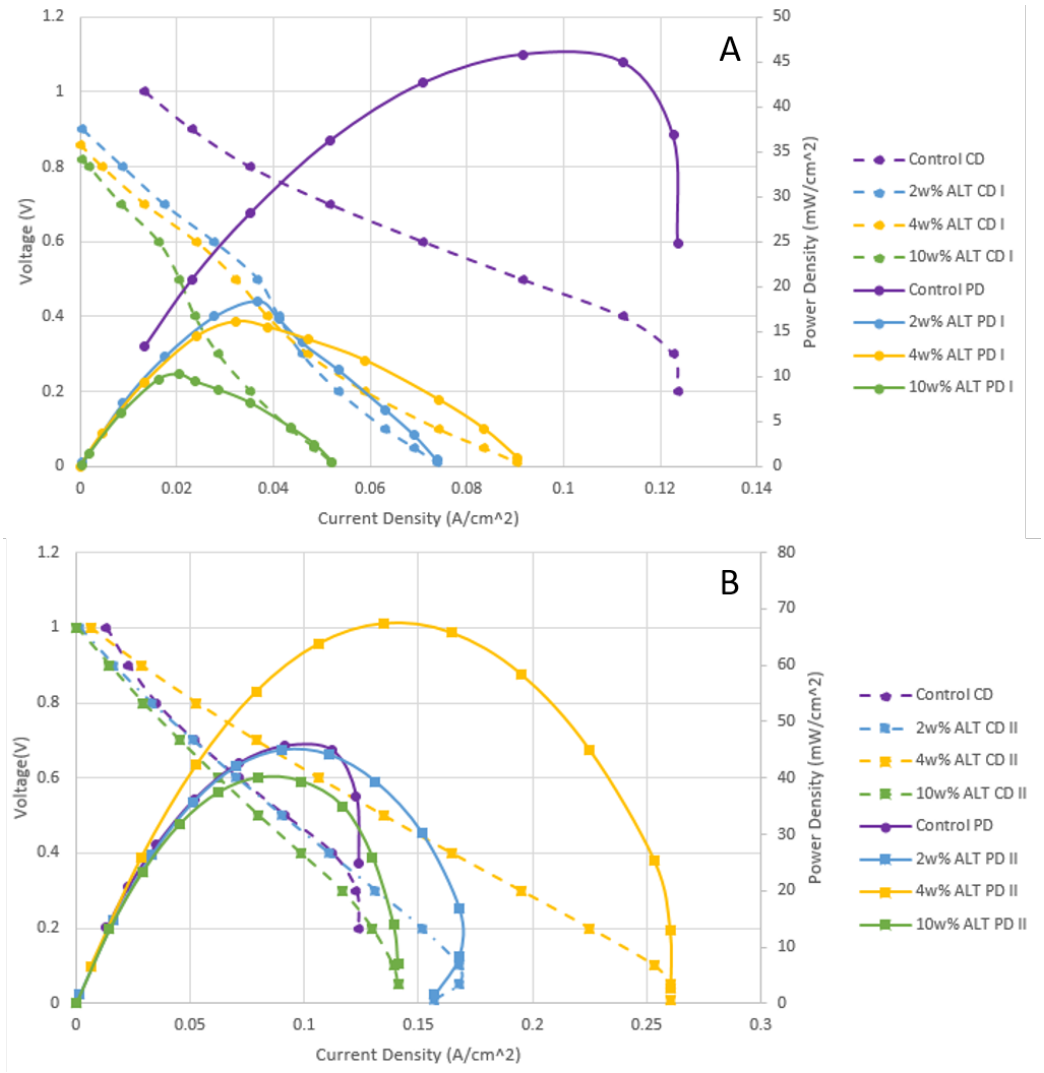


Figure 5.6: Power density (solid) and current density (dashed) curves for 2, 4, and 10 w% ALT doped Ni/GDC anode SOFCs. Curves are based on consecutive V-I scans taken after 24 hours of operation at 0.5V overpotential. Scan presented in (B) was performed seconds after the scan shown in (A).

manipulation.

Performance results for Ni/GDC lightly doped with alumina shows little detrimental changes in all cases, as given in figure 5.7A, with slight enhancements found for 2w% alumina concentration. Power output for these cells range from about $70W/cm^2$ for 1 and 5w% up to $85W/cm^2$ for 2w%. These trace amounts of alumina

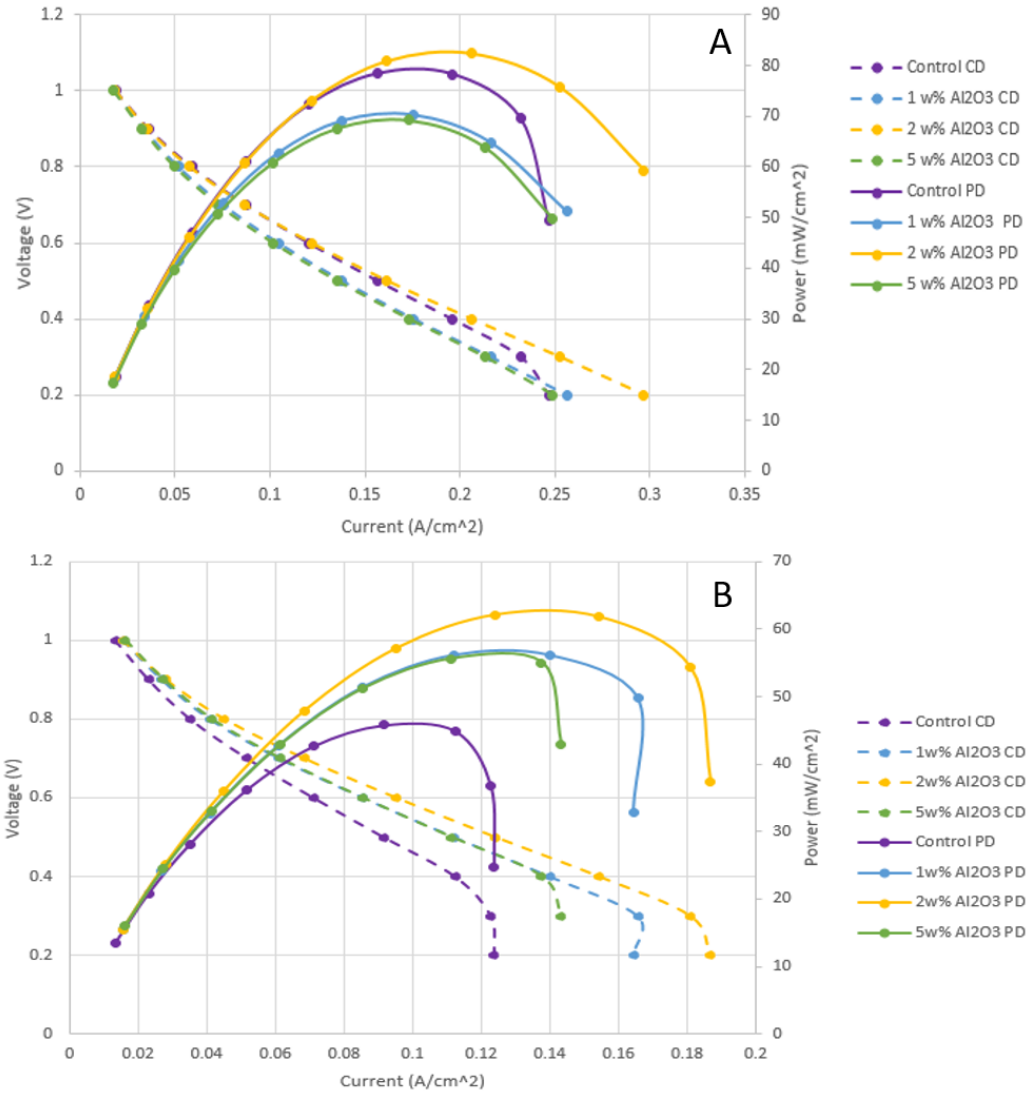


Figure 5.7: Power density (solid) and current density (dashed) curves for 1, 2, and 5 w% alumina doped Ni/GDC anode SOFCs. Curves are based on V-I scans taken at A) peak performance, and B) after 24 hours of operation at 0.5V overpotential.

also appear to reduce the transport losses in the cell for all cases, however, the mechanism by which this occurs is not understood. However, a drastic increase in active area would facilitate fuel transport kinetics that supports the V-I results, but this is not an expected outcome of the formation of nickel aluminate. Nickel aluminate generally possesses no conductive properties and is usually associated with a decrease

of initial performance caused by blocking of the TPB. Only later, after it reduces, does the effect of nickel aluminate begin to alleviate lost TPB. Activation and ohmic

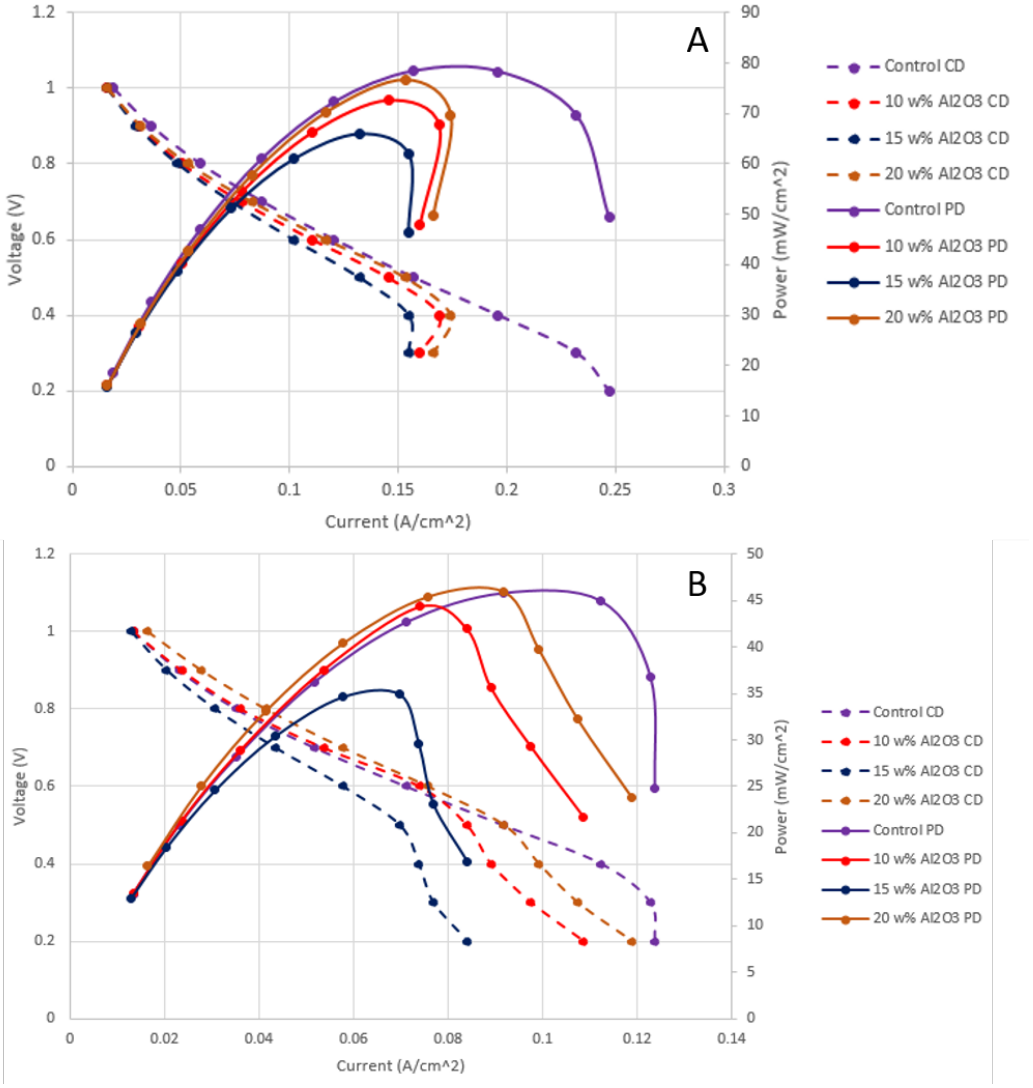


Figure 5.8: Power density (solid) and current density (dashed) curves for 10, 15, and 20 w% alumina doped Ni/GDC anode SOFCs. Curves are based on V-I scans taken at A) peak performance, and B) after 24 hours of operation at 0.5V overpotential.

losses appear to be unchanged as compared to the control cell data. Results from V-I scans of light alumina doped Ni/GDC anodes after 24 hours of operation are given in figure 5.7B. These results confirm the degradation results presented previously as all

alumina concentrations exceeded the performance of the control cells. Ohmic losses in the doped cells appear to have been alleviated slightly compared to the control data while little change to activation losses are observed. The main detriment is observed in the transport loss region of the polarization curve. Despite its absence in the initial performance scan, the cells experienced significant losses associated with the inability of fuel to reach active areas.

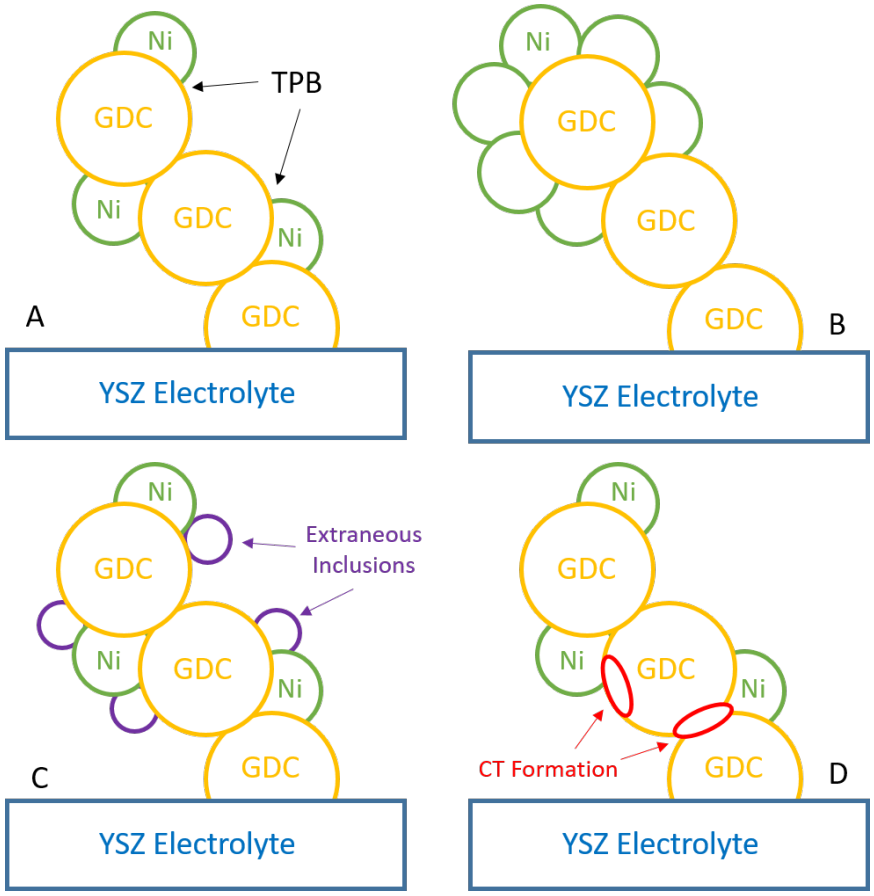


Figure 5.9: Schematic representations of the hypothesized deleterious mechanisms associated with ALT and alumina doping of Ni/GDC anodes. A. depicts an optimum distribution of TPB, B. shows the result of coarsening of nickel metal fully engulfing GDC particles, C. represents the effects of extraneous particles (TiO, Al_2O_3, $NiAl_2O_4$, etc.) clogging TPB regions, and D. gives possible examples of CT formation blocking the path of oxygen ions through the GDC network.

Continuing to increase the concentration of alumina in the anode reverses the

transport kinetic effects found with trace amounts, as seen in figure 5.8A. Suggesting the presence of nickel aluminate, and any unreacted alumina, is clogging active areas of the cell. This effect, however, did not significantly inhibit the power generation of the cell, as was seen with ALT doping. Power produced by these cells ranged from $65W/cm^2$ (for 15w%) to $78W/cm^2$ (for 20w%), just under that of the control cells. Slopes of the ohmic loss regions are comparable across the board and no significant changes in activation polarization were observed. Post operational performance results for the anodes heavily doped with alumina give curves not usually representative of SOFC performance data, as can be seen in figure 5.8B. The two distinct regions of the power curve may represent the appearance of a new mechanism associated with fuel cell operation. With the exception of this behavior and the poor performance of the 15w% cells, power and current generation are comparable to those of the control cells.

FESEM

Scanning Electron Microscopy techniques are pivotal in evaluating systems of materials which are heterogenous at the micro-scale. This assists in evaluating microstructural evolutions as well as devising theories to explain the mechanisms surrounding phenomena that are otherwise undetectable. For example, figure 5.10 depicts the various differences between the microstructure of a Ni/GDC anode before and after operation. A clear distinction can be observed in the location and structure of the nickel oxide (B) and the nickel metal (A) after subsequent reduction during operation. The nickel oxide is distributed across the surface of the GDC and composed of small, uniform particles. After reduction and during operation, the nickel metal particles agglomerate to form large rough formations and can be seen fully engulfing much of the GDC structure. This is an effective representation of the coarsening

effects of Ostwald ripening theory.

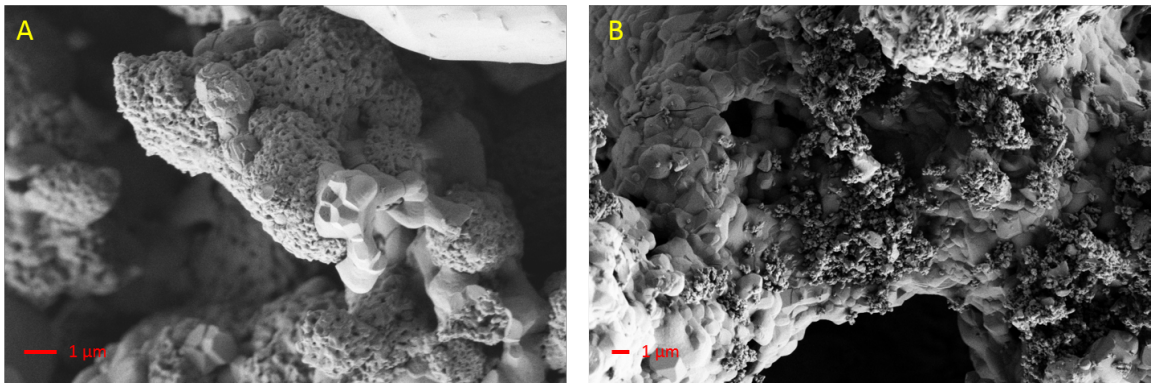


Figure 5.10: Field Emmision Scanning Electron Microscopy images of Ni/GDC anodes without dopant A) after operation and B) before operation. GDC can be seen as the smooth large grain material. The rough regions of (A) are composed of nickel metal while nickel oxide can be seen as the small particles in (B).

The microstructures of the ALT and alumina doped Ni/GDC anodes depicted in figure 5.11 reveal the various structural evolutions occurring in these systems upon introduction of small amounts of secondary elements. Unfortunately, no direct evidence of diffusion caging was witness within any of the tested anodes. However, all of these images show a reduced effect of agglomeration of nickel particles when compared to the control microstructure shown above. Smaller, more interspersed nickel is observed in all doped samples as well as a lessened effect of nickel consuming GDC particles. Two major structural changes are observed in the ALT doped anodes. First, large rods of what appears to be the GDC ceramic material formed in the 2w% ALT doped sample (image A). These rods are distributed across much of the cell and appear to bridge between GDC regions, further strengthening the theory that they are made of GDC. These large GDC rods are not observed in any other cells, ALT or alumina doped. Second, the GDC particles of the 4w% ALT doped cell (Image C) formed an odd wavy roughness that was also not observed in cells of other concentrations of ALT or alumina. The roughness appears to be present on

all GDC particles making it unlikely to be a result of secondary phase formation. Reduction of ceria could also explain such a roughness. As oxygen is released at high temperatures bubbles may form on the surface of the particle. However, if this is the case, there should be evidence of this phenomenon in all GDC based anodes. A major detrimental effect can also be observed in the ALT doped cells but not the alumina doped cells. At many GDC/Ni interfaces, it is apparent that the nickel particle has pulled away from the GDC, most likely as a result of coarsening. In areas where this occurs, the TPB that was once available, is completely disrupted. It should also be noted that the large spherical globules seen on the surface of the 10w% ALT doped cell (Image E) is silver metal used as an electrical interconnect between the anode and the measurement device. It is unlikely to have any effect on the interactions within the cell.

The primary microstructural changes in the alumina doped samples are associated with lessening of the coarsening effect of Ostwald ripening as noted previously. This results in a better distribution of small nickel particles. This is especially evident in the 2 w% alumina image (B) where nickel particles are seen to be as small as about 250 nm. The geometric shape of the GDC particles in this image is also of interest. Normally, ceramic materials like GDC and YSZ form smooth irregularly shaped grains, but these particles have clearly defined, sharp corners. This could simply be attributed to a random processing occurrence when manufacturing the powder or could be a result of secondary phase formation. In the 5 w% alumina image (F), the nickel almost appears to be spread across the surface of the GDC structure in some regions. This is also apparent in the high concentration alumina doped anode images shown in figure 5.12, particularly in the 10 w% image. This could be evidence of secondary phase formation because of its fundamental difference from the other two components of the system. The other images in figure 5.12 (B and

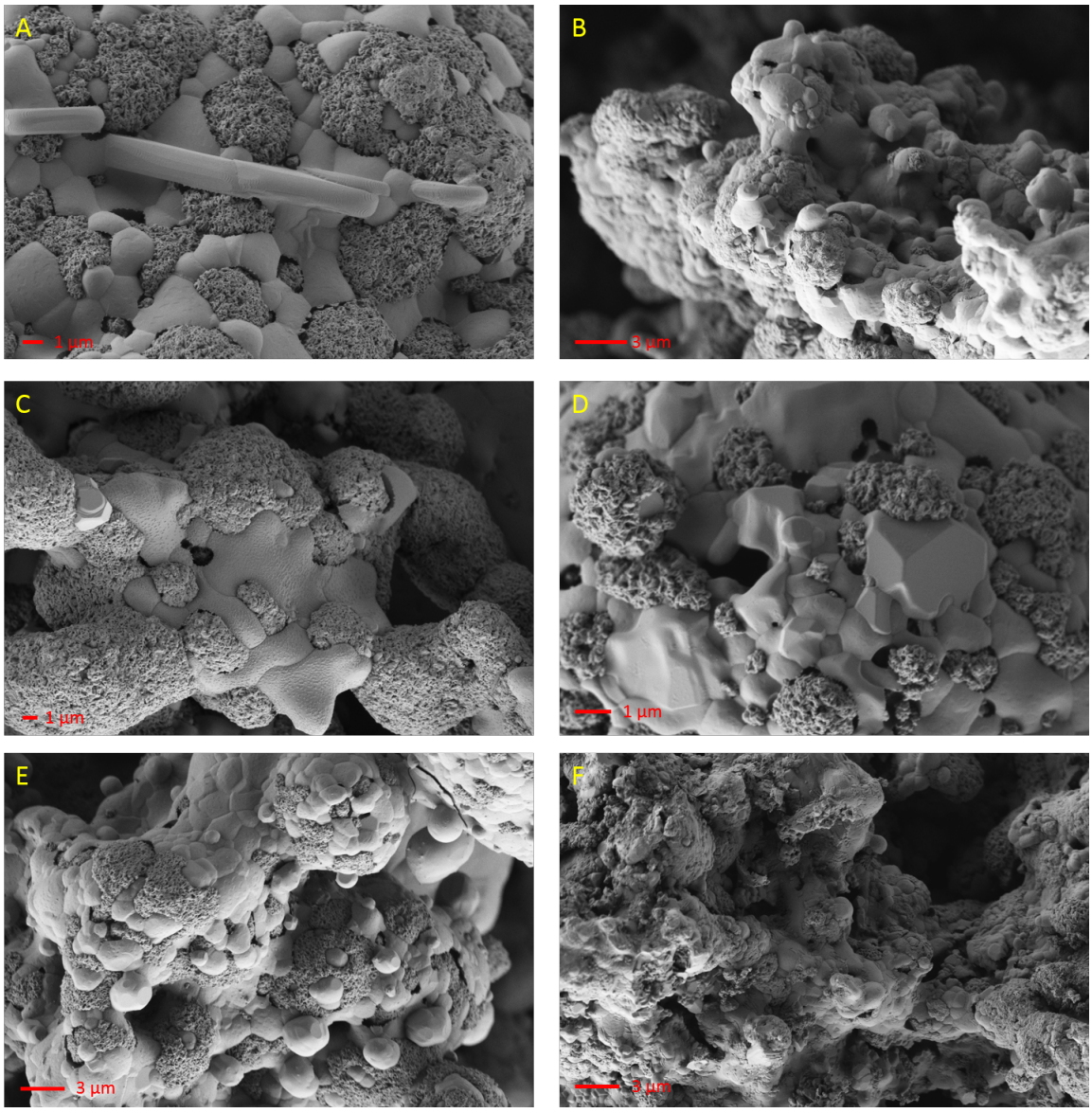


Figure 5.11: FESEM images of various microstructural differences between A) 2w% ALT, B) 1w% alumina, C) 4w% ALT, D) 2w% alumina, E) 10w% ALT, and F) 5w% alumina doped Ni/GDC anodes after operation at 0.5V overpotential.

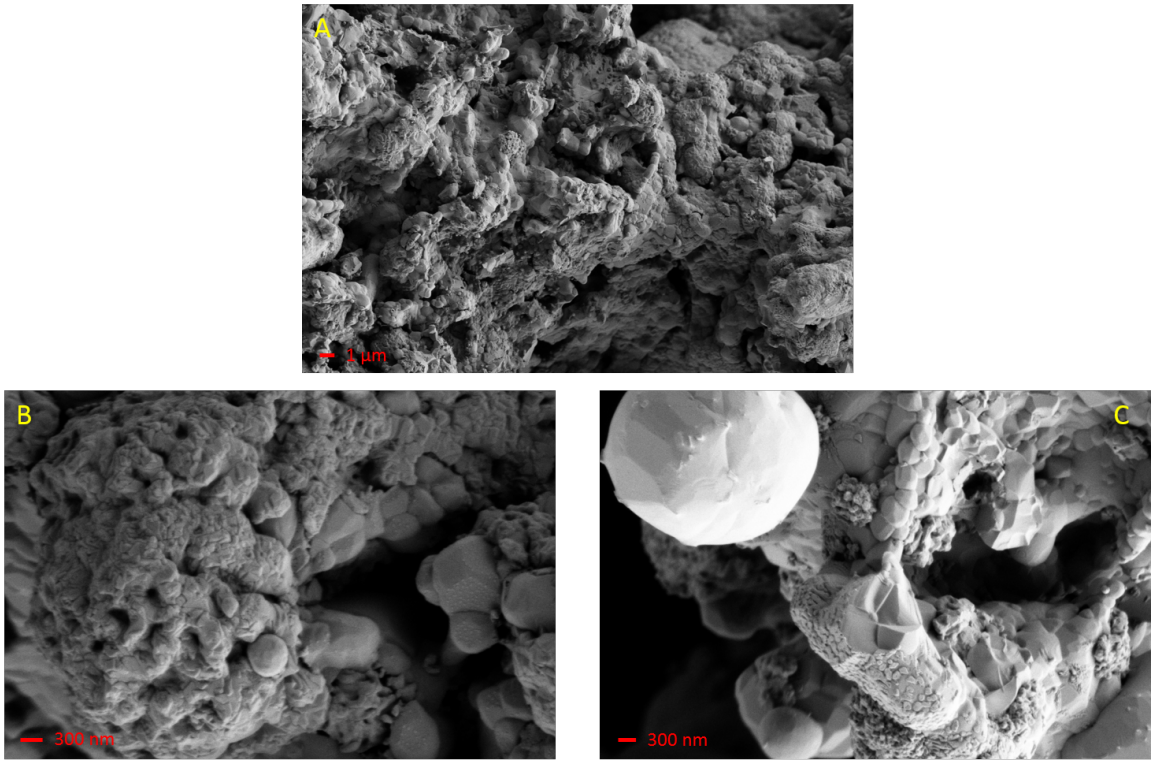


Figure 5.12: FESEM images of various microstructural differences between A) 10w%, B) 15w%, C) 20w% alumina doped Ni/GDC anodes after operation at 0.5V overpotential.

C) odd nano-decoration located entirely on GDC particles. Since it is only present in the two most highly concentrated samples, the material is likely alumina. This suggests a solubility limit exists for alumina dissolved in nickel oxide to form nickel aluminate between 10 and 15w%. It may be possible to increase this limit slightly by processing the doped anodes at an elevated temperature (i.e. $>$ 1400 °C). It should be noted that the large spherical particle in in the corner of figure 5.12C is the silver metal used as electrical interconnect between the cell and the test apparatus.

Despite discovery of the deleterious effects of ALT on the Ni/GDC anode system, both mechanically and electrochemically, further investigations revealed pure alumina to be an equally prominent modifier in this system as ALT was for

the Ni/YSZ anode system. Mechanical enhancement due to alumina inclusion far exceeded those for ALT doped NiO/YSZ anode precursor materials. Trace amounts of alumina in Ni/GDC anodes slightly increased longevity during operation, while high concentrations significantly reduced the rate of degradation of the anode. These trace amounts of alumina effect overall power output of the cell very little, but appear to mitigate transport losses during the initial stages of operation. Heavier concentrations of alumina show an opposite effect however, escalating transport losses initially but alleviating them after 24 hours of degradation. These collective results suggest the issue lies in the presence of titanium in the system, most likely forming secondary phases with the constituents of GDC. These results prove alumina is the primary multi-functional modifier of nickel-based SOFC anodes and warrants further investigation into the aluminate spinel class of ceramics for use as anode materials.

Aluminate Spinel Materials

The success of nickel aluminate enhancement of various SOFC anode systems breeds interest into the unexplored properties of this class of aluminate spinel ceramics. Previous studies of cobalt and copper aluminate show their potential in catalysis applications [62, 63, 65], but have not been considered for use in fuel cell technologies. The thermal stability inherent to these ceramics, along with the reduction phenomena apparent in nickel aluminate, make these materials optimal for use as cermet electrocatalyst precursors.

The optimal method of processing cermet anodes utilizes both components in their oxide phases. This eliminates the difficulty of adhering metal and ceramic materials. Nickel oxide is favored for this method due to its availability and cost, operational performance, and thermal stability at necessary anode processing conditions. Other transition metals, such as copper and cobalt, are considered to

possess equivalent performance capabilities as nickel and have been shown to be more resilient to carbon deposition [43], but cannot be processed by the same methods. Both copper and cobalt oxide reduce readily at or below nominal SOFC operating temperatures but possess low melting points such that they cannot be effectively processed in an anode system. Developing ceramic materials composed of these transition metals but with greater thermal stability is paramount to broadening the base of usable SOFC anode materials. Aluminate spinel oxides possess adequate thermal stability to be processed as anode materials but have largely not been considered for use in SOFC systems. The following evaluates the synthesis of phase pure cobalt and copper aluminate powders, and their basic reduction kinetics, as they pertain to SOFC operation.

Synthesis

The synthesis of phase pure powders is necessary to accurately determine the properties of the material under investigation. In order for these synthesis methods to be viable for production of SOFC anode materials, they must be simple and inexpensive. Solid-state and co-precipitation syntheses embody this as both can be completed in as little as three or four steps over as many days. The constituents required for these methods are also affordable considering there is no need for extraneous organic bonding agents as may be used in more sophisticated techniques such as combustion synthesis or Pechini approach.

The freeze-dried solid-state synthesis was effective in producing light fluffy powder while the co-precipitation method resulted in coarse, tightly packed agglomerates. This is related to the integration of the two components prior to heat treatment to form the final product. In solid-state synthesis (i.e.mechanically mixed oxides), the two materials are closely combined primarily during the freeze-drying process.

During sublimation, ice is evaporated directly from the frozen slurry, therefore, leaving large voids between powder particulate and resulting in an aerated powder. For co-precipitation; the transition metal and alumina are combined in liquid phases, dried, and calcined to form ashes. These ashes are dense in comparison to the resultant powder from freeze-drying, and so, the resulting powder is dense and compact after heat treatment. The difference is visually obvious, as can be seen in figure 5.13 for cobalt aluminate and figure 5.14 for copper aluminate. Both outcomes are useful in their own way. Fluffy powders are easily dispersed in solution while dense powders form robust compacts.

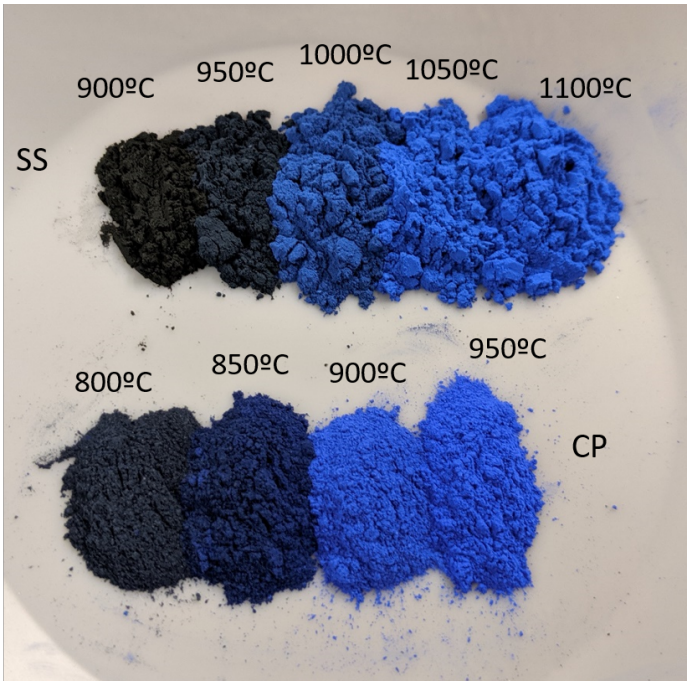


Figure 5.13: Resultant cobalt aluminate powders synthesized from the solid-state method (SS) and co-precipitation method (CP) for various heat treatment temperatures.

A large variance of pigment can also be observed across the range of heat treatment temperatures utilized. Solid-state syntheses resulted in a near-black precursor powder for cobalt aluminate, and a light gray precursor powder for copper

aluminate. The calcined ashes gathered from the co-precipitation method were mostly black with a slight metallic tint for both aluminate precursors. Whichever method was used the cobalt aluminate developed a dull indigo color at first and, upon further increasing temperature, evolved into a vibrant blue often associated with atomic cobalt deposition. Copper aluminate, on the other hand, turns from gray to light brown at intermediate temperatures and to a deep chocolate brown at elevated temperatures. The temperatures at which these shades appear depend upon the synthesis method. The bright blue of cobalt aluminate develops around 1000 °C for the solid-state method or at 850 °C for co-precipitation. A similar effect is observed for copper aluminate with the chocolate brown shade appearing at 1100 °C for solid state and 750 °C for co-precipitate. While these vibrant hues have been reported in the literature [62–65, 75], they are not necessarily indicative of phase purity.



Figure 5.14: Resultant copper aluminate powders synthesized from the solid state method (SS) and co-precipitation method (CP) for various heat treatment temperatures.

Phase Purity As stated previously, phase purity is necessary to accurately predict the various electrical, mechanical, and catalytic properties required for SOFC anode materials. Even minuscule impurities can impede conductivity or initiate crack growth within a sample. To confirm these synthesis methods are capable of producing phase pure aluminate materials, powder XRD was performed on select samples. Because of the lack of color change in the lowest temperature heat-treated samples, further testing was not performed on the 900 °C and 950 °C solid-state cobalt aluminate, 800 °C co-precipitated cobalt aluminate, 950 °C solid-state copper aluminate, or 650 °C co-precipitated copper aluminate.

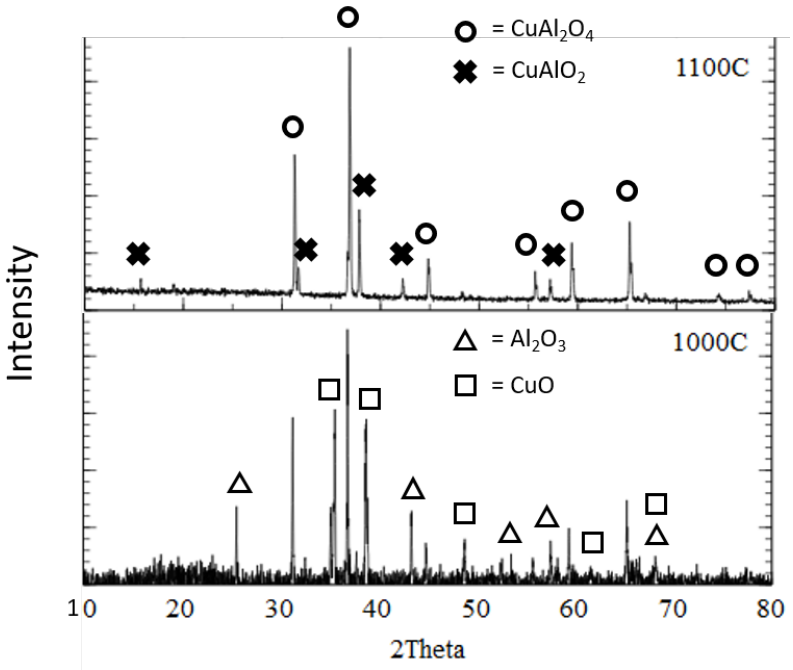


Figure 5.15: Powder XRD diffraction pattern for solid-state synthesized copper aluminate samples heat-treated at 1000 °C and 1100 °C.

The XRD patterns for solid-state synthesized copper aluminate are given in figure 5.15. From this, samples treated at 1000 °C have begun to form the spinel structured aluminate (marked by), but mixed with significant concentrations of

both copper oxide and alumina constituents (marked by □ and △ respectively). Increasing the treatment temperature to 1100 °C removed the unwanted constituents but replaced them with a $CuAlO_2$ oxide structure (denoted by X). Delafossite oxides like this one have been investigated for their semiconductive capabilities and optical transparency. Based on these properties, this class of materials is more conducive to solar photovoltaic systems than SOFC applications [76, 77]. Analyzing

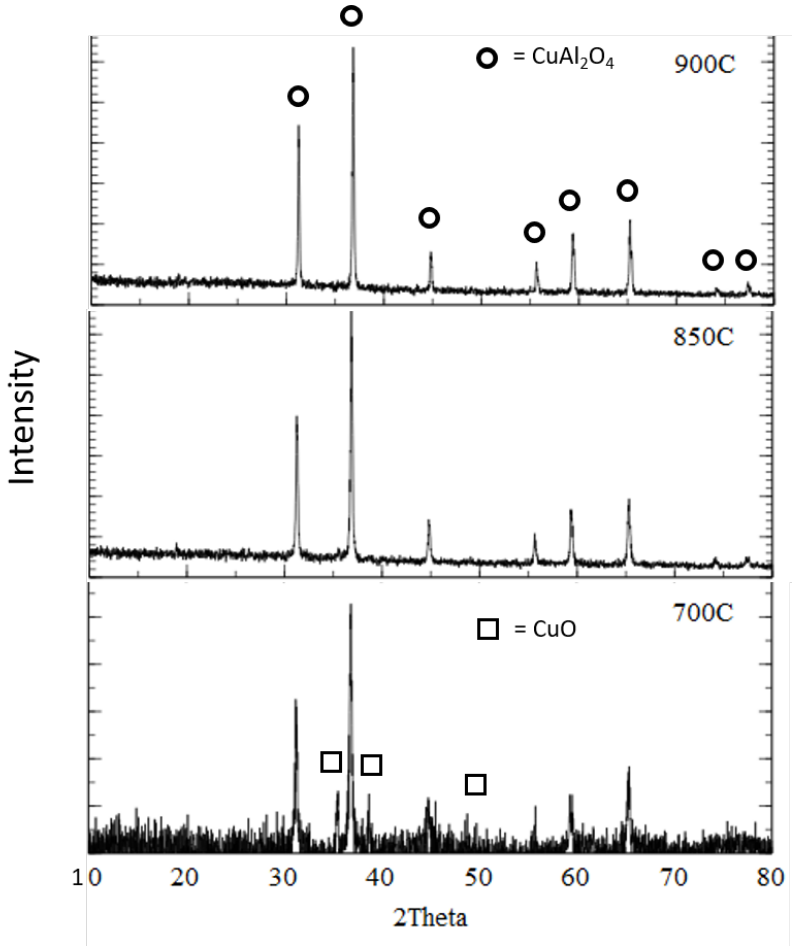


Figure 5.16: Powder XRD diffraction pattern for co-precipitate synthesized copper aluminate samples heat-treated at 700 °C, 850 °C, and 900 °C.

the diffraction patterns of the co-precipitated copper aluminate yields better results, as shown in figure 5.16. At low treatment temperatures, small concentrations of CuO

remain in the system until treatment at 850 °C. Above this temperature only pure copper aluminate is present in the system and persists through higher temperatures. Significant noise can also be observed in the 700 °C XRD data. This could be attributed to the orientation variance of the randomly oriented particulates, which would be representative of high levels of impurities.

Diffraction patterns for the solid-state cobalt aluminate show a nearly phase pure material at 1000 °C, however, there are a few minuscule peaks that are unaccounted for (cobalt aluminate peaks are denoted by in figure 5.15). The Jade phase identification software did not recognize these peaks by themselves. They are most likely associated with remaining cobalt oxide or alumina in concentrations narrowly within the detection limit of the equipment. The Phase purity of cobalt aluminate samples persists to 1100 °C. Co-precipitated cobalt aluminate (shown in figure 5.18)

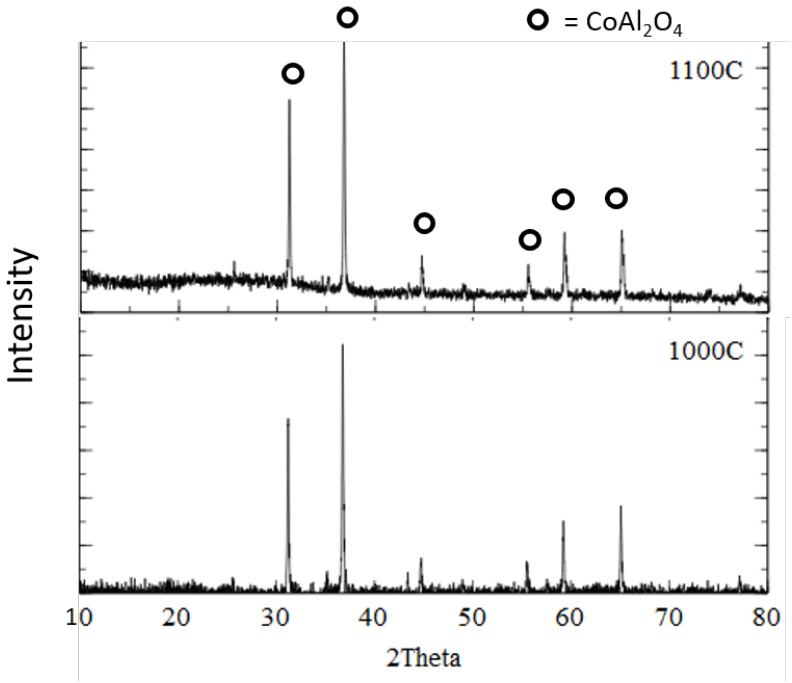


Figure 5.17: Powder XRD diffraction pattern for solid-state synthesized cobalt aluminate samples heat-treated at 1000 °C and 1100 °C.

diffraction patterns reveal the persistence of a phase pure material at and above 850 °C. However, as was seen with the 700 °C co-precipitated copper aluminate, large data variations are observed across the entire scan range, suggesting defects or impurities in the sample. Based on these XRD results, further experimentation

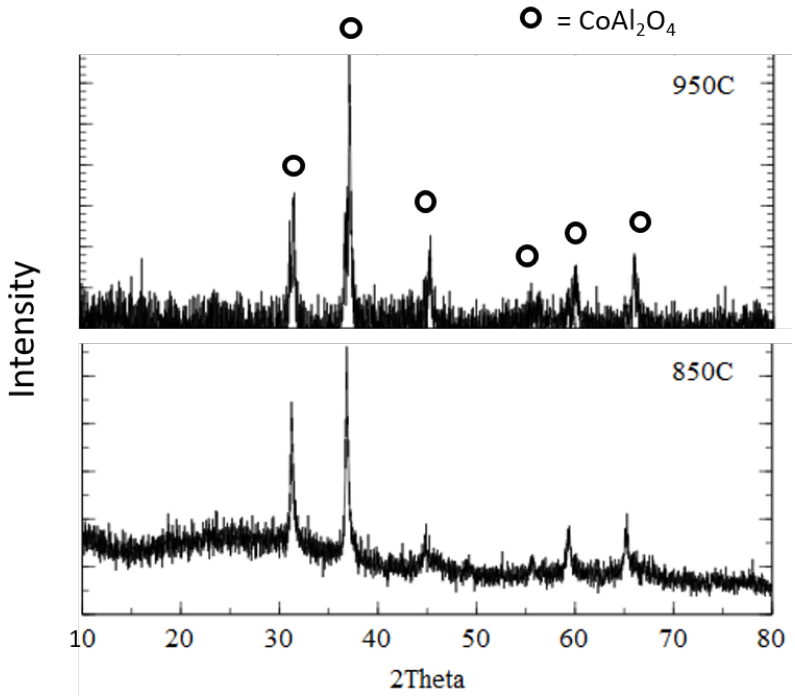


Figure 5.18: Powder XRD diffraction pattern for co-precipitate synthesized cobalt aluminate samples heat-treated at 850 °C, and 950 °C.

proceeded with solid state synthesized cobalt aluminate treated at 1000 °C and co-precipitate synthesized copper aluminate treated at 850 °C.

Reduction

The reduction of nickel aluminate into nickel metal with alumina decoration has been determined to be the primary mechanism behind the electrochemical resiliency enhancement of ALT doped Ni/YSZ SOFC anodes. This preserves the electron-conducting network over longer life cycles, allowing for effective current collection.

Assessing the reduction kinetics of other aluminate materials is pertinent to a better understanding of this mechanism and for the consideration of these materials for use as stabilizing components in SOFC anode systems. Figures 5.19 and 5.20 show the before and after images of the 6 sample pellets (3 cobalt-based and 3 copper-based) used for reduction evaluation. At this reduction temperature both the pure oxide samples (center) underwent full reduction, as expected. The bright blue color disappeared from the cobalt aluminate sample, giving way to a dark gray, suggesting some degree of reduction was achieved. Similarly the 50/50 cobalt oxide/cobalt

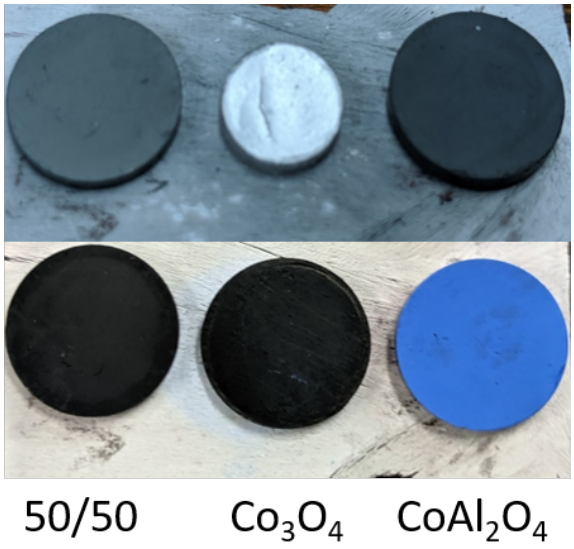


Figure 5.19: Cobalt based sample pellets before reduction (bottom) and after reduction at 850 °C for 12 hours (top).

aluminate sample turned from black to a light gray. The difference in color between this sample and the reduced cobalt aluminate sample indicates that more cobalt metal phase is present in the reduced 50/50 sample. The copper aluminate sample, on the other hand, turned from a light chocolate brown to a dark reddish-brown. This color change is not indicative of reduction to copper metal. This is either a result of the formation of a secondary phase or stabilization of the oxide phase. It is

not unheard of for these aluminate spinels to fully stabilized the oxide phase. It was found that pure nickel aluminate did not reduce readily at nominal SOFC operating temperatures when analyzed using thermogravimetric analysis [7]. Finally, the 50/50 copper oxide/copper aluminate sample turned from a dull olive-gray to a deep brown while simultaneously experiencing significant volumetric expansion. In addition, the reduced sample had practically no particle interconnection and disintegrated upon even light handling. Based on the reduction of the pure copper aluminate sample and the color change, the oxide phase is likely to have fully reduced while the copper aluminate remained. The release of oxygen from the reducing copper oxide could attribute to the increase in porosity as it escapes the system, resulting in poor particle-to-particle connectivity.

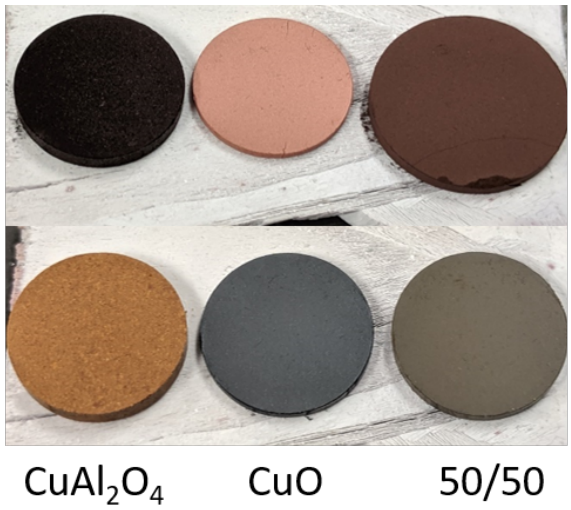


Figure 5.20: Copper-based sample pellets before reduction (bottom) and after reduction at 850 °C for 12 hours (top).

Field Emission Scanning Electron Microscopy (FESEM) performed on these samples gives some insight from a microstructural standpoint. Unfortunately, the surfaces of most of the samples were too unstable to image properly. Only the pure copper aluminate sample was resilient enough to withstand the bombardment of a

1 kV electron beam. These images are given in figure 5.21. The particulate found on the fracture surfaces of the reduced copper aluminate appear to be extensively distributed across this surface and throughout the sample. The particulates take the shape of smooth orbs, short rods or cylinders, and many-sided polygons. Sizes seem to range from 200 nm to 2 μm. Though several orders of magnitude larger than those discovered in the work published by Driscoll et al. [2, 60], with the amount of alumina present in the copper aluminate system, it is expected that small globules would grow and form large uniform shapes as it continues to leach out of the spinel. The electron back-scatter image (figure 5.21 C) shows a stark contrast between the base particle and the particulate decorating it. It is commonly known that heavier elements tend to scatter more electrons making them appear brighter. However, if the target is a solid solution, homogenous on an atomic scale, the effects of each constituent are cumulative [78]. By this law, the back-scattering effect of alumina would be much greater than both copper metal and its oxide. By this reasoning, however, the particulate could also be made of copper aluminate spinel or delafossite phases. Without true elemental analysis, this is merely speculation.

In an attempt to produce more stable samples for FESEM imaging, two additional samples of both copper aluminate and cobalt aluminate were sintered in air to 1100 °C for two hours prior to reducing under identical conditions. Once again, the cobalt aluminate surface was too unstable to image properly. However, investigation of the sintered copper aluminate sample, in figure 5.22, revealed the existence of three distinct phases: A smooth glassy phase, large (>5μm) polygonal structures, and regions of rough, clustered grains. The sample appears to be primarily composed of the glassy phase and clusters of small, rough grains. Based on the interface between the two main phases, the clustered grains seem to melt together to form the large grain, glassy regions, or vice versa. The two regions also exhibit differing fracture

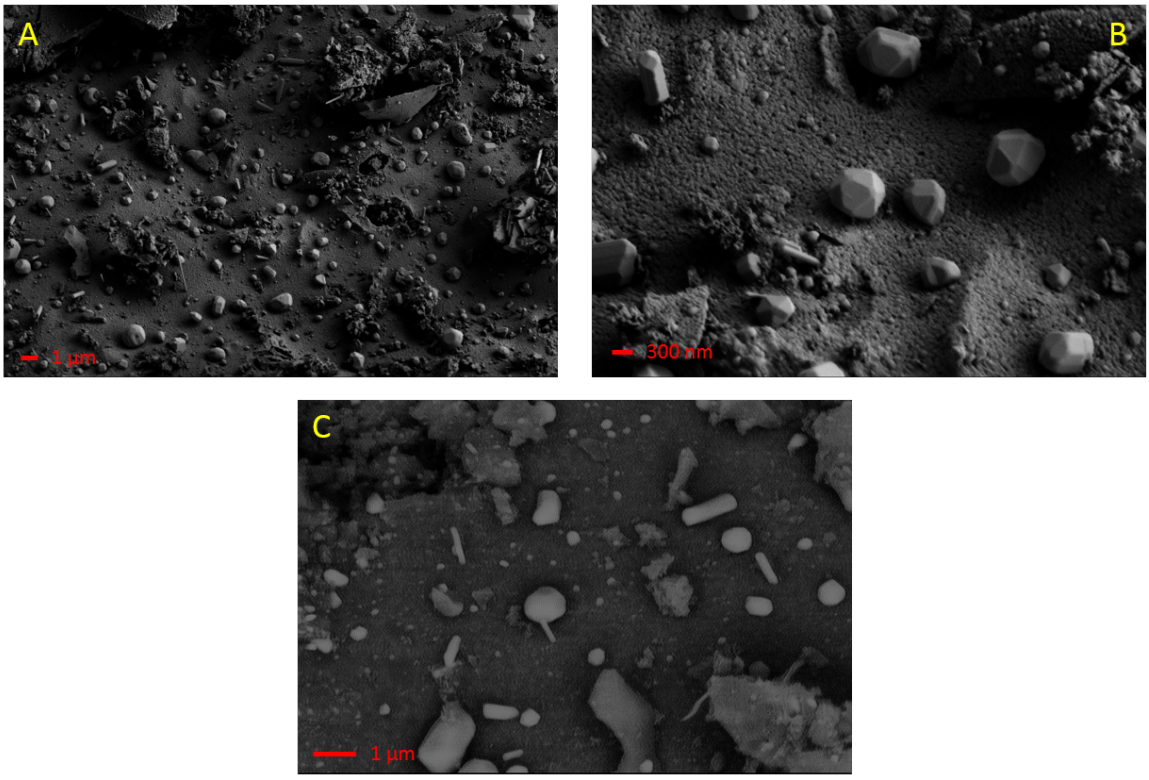


Figure 5.21: Micrographs of the fracture surface of a reduced copper aluminate sample: A) Approximately 100μm area of fracture surface decorated with 1μm particulate, B) Detail view of the microparticulate resting on a large agglomeration of tiny grains, C) Electron back-scatter image depicting the variety of sizes and shapes of the particulate.

mechanisms. The glassy phase appears to fracture in a brittle manner, suggesting it is composed of a ceramic material. The clustered grains, on the other hand, seem to have pulled apart with obvious plastic deformation, suggesting it is composed of soft metal. Again, without proper elemental analysis of these materials, their exact compositions are unknown.

This foundational study of the synthesis and reduction behavior of copper and cobalt aluminate spinels demonstrated similarity with that of nickel aluminate. Both spinels readily reduced at nominal SOFC operating temperatures within 12 hours, based on observable color changes. Microstructural evaluations of reduced copper

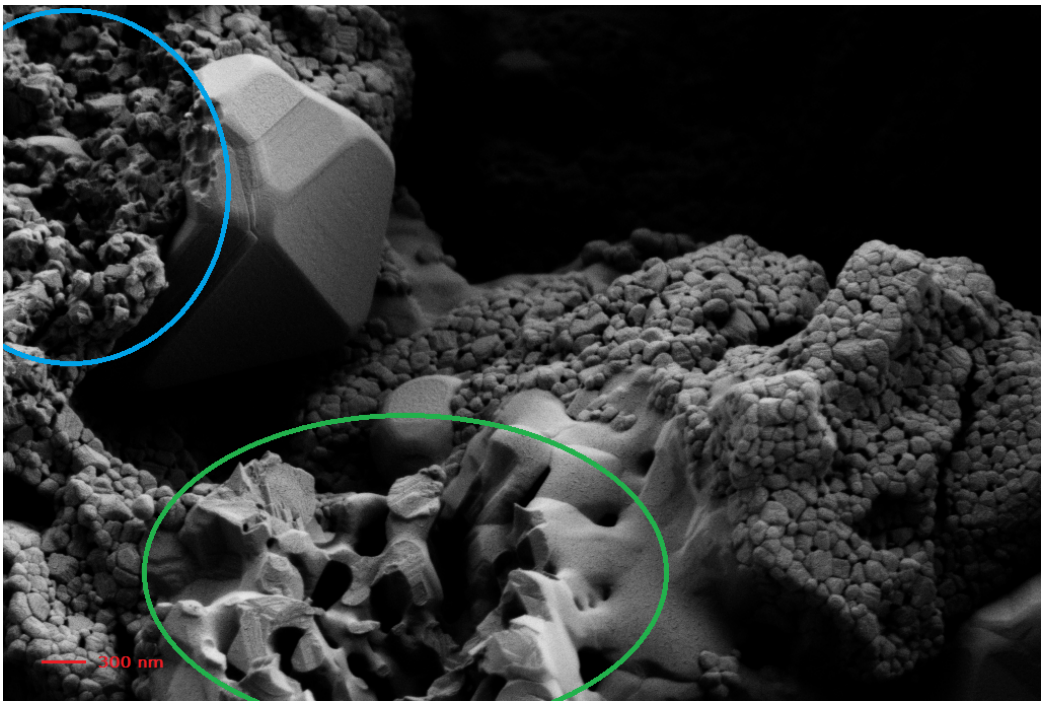


Figure 5.22: Fractured surface of a sintered copper aluminate after reduction with regions of brittle fracture circled in green and regions of ductile fracture circled in blue.

aluminate using FESEM revealed the formation of micron sized particulate. While extensive elemental mapping was not included in this study, electron backscatter imaging indicates the particulate is not the same composition as the bulk of the material, suggesting it is alumina decoration. This mirrors findings of nano-sized alumina decoration reported by Driscoll et al. [60]. This evidence supports the claim that aluminate spinels reduce in a similar fashion, indicating possible viability as SOFC anode precursor materials.

CONCLUSION

Pertinent Results

The exploration of resiliency enhancement of SOFC anode materials has led to the use of aluminum titanate to both stabilize detrimental electrochemical processes and increase mechanical strength in the Ni/YSZ cermet anode system. The basis of these effects was the formation of secondary phases from the constituents of ALT and the components of the cermet. The formation of nickel aluminate spinel reduced the effects of nickel coarsening, carbon coking from carbonaceous fuels, and degeneration from redox cycling. The mechanical strength enhancement, on the other hand, was derived from the formation of titanium zirconate. Transferring these mechanisms to other anode systems would not only prove their existence but also their viability for implementation in the fuel cell industry. To further evaluate the effects of ALT on SOFC anodes, each cermet component was exchanged with other commonly used SOFC materials. The ion conductor, YSZ, was exchanged with GDC while the aluminate spinel class of materials was explored for copper and cobalt.

While investigating ALT doping of Ni/GDC anodes, detrimental effects were immediately observed. Indentation fracture resistance measurement found little to no effect from the addition of ALT. Electrochemical tests revealed a two-fold increase in the rate of degradation in ALT cells, as well as, a marked drop in peak performance. However, a new mechanism was discovered in this system. During performance evaluations, each of ALT doped cells, regardless of concentration, were able to recover nearly 100% of peak performance after 24 hours of operation. This phenomenon was discovered during post-operation V-I scans when the cells were being driven at nearly 0.01 V potential with no observable transport losses. When the cell was returned to normal operating conditions, the current output doubled. A consecutive V-I scan

revealed the performance had returned to near peak output. Despite the deleterious outcomes discovered within this system, the fracture resistance results confirmed the theorized mechanical strength enhancement from the solid solution of titania and zirconia.

Given that the exact role of titanium was unknown in the Ni/GDC anode system, it was removed from the equation to better explore the mechanisms involved with nickel aluminate. Further indentation fracture resistance measurements of NiO/GDC doped with 5 and 10w% alumina showed a 40% and 60% increase, respectively. This far exceeds the same effects for ALT doped NiO/YSZ anode precursors reported by Kent, McCleary et al. and Driscoll et al. [3,4,7]. Concentrations around 1w% alumina reduced degradation rates by 100% while high concentrations (> 10w%) of alumina more drastically reduced degradation, even achieving less than 0.25%/hour after 20 hours of operation. Alumina was observed to have little to no effect on the activation and ohmic losses associated with fuel cell operation kinetics but was shown to almost entirely eliminate transport losses at peak performance in low concentrations. This effect was not observed for high concentrations of alumina. Peak power outputs were between 70 and 80 W/cm^2 for low concentrations and between 65 and 78 W/cm^2 for high concentrations. Obvious signs of a reduced effect of coarsening were observed in the anode microstructure, including a reduction in overall nickel particle size and a greater distribution of nickel particles throughout the system.

Evaluation of the cobalt and copper aluminate material systems revealed promise for the implementation of these materials in SOFC anodes, but much experimentation needs to be completed. Synthesis of the aluminate spinels was discovered to be relatively simple using common solid-state and co-precipitation methods. These processes are also affordable, using only oxide and metallic salt components, respectively. Cobalt and copper aluminate were shown to reduce readily

at nominal SOFC operating conditions and particulate decoration was observed in copper aluminate, similar to reports by Driscoll et al. for the nickel aluminate system [60].

Future Directions

Extensive electrochemical tests confirm the mitigation of coarsening due to alumina inclusion in Ni/GDC anodes, but various other degradation mechanism are yet to be explored. As was performed for ALT doping of Ni/YSZ anodes, an evaluation of the effects of coking and redox, cycling should be performed on alumina doped Ni/GDC anode materials. A more extensive assessment of mechanical strength could be performed to confirm the results of indentation fracture resistance measurements. Elemental analysis of ALT doped NiO/GDC anode precursor materials could elucidate the exact mechanisms behind the deleterious effects witnessed only in this specific system.

The evidence of aluminate spinel reduction mechanisms gives promise to the use of these materials in SOFC anodes, but the evaluation of various properties of these materials must still be completed, including; mechanical strength, electrical and ionic conductivity, hydrogen and carbonaceous fuel catalytic activity, and chemical interactions with other SOFC component materials. With a better understanding of the their properties, the spinel materials may be implemented in SOFC anodes as both a stabilizing agent in trace amounts, as well as a primary component.

REFERENCES CITED

[1] S. S. D. Driscoll, C. Hunt, J. Muretta, "Thermally Stabilized Nickel Electro-Catalyst Introduced by Infiltration for High Temperature Electrochemical Energy Conversion," *ECS Transactions*, vol. 53, pp. 67–72, 2004.

[2] D. R. Driscoll, M. D. McIntyre, M. M. Welander, S. W. Sofie, and R. A. Walker, "Enhancement of high temperature metallic catalysts: Aluminum titanate in the nickel-zirconia system," *Applied Catalysis A: General*, vol. 527, pp. 36–44, 2016.

[3] D. R. Driscoll, B. W. Tokmakian, N. P. Johnson, C. D. Hunt, and S. W. Sofie, "Catalyst enhancing aluminum titanate for increasing strength of nickel-zirconia cermets," *Materials Letters*, vol. 209, pp. 307–310, 2017.

[4] M. McCleary and R. Amendola, "Effect of Aluminum Titanate (Al2TiO5) Doping on the Mechanical Performance of Solid Oxide Fuel Cell Ni-YSZ Anode," *Fuel Cells*, vol. 17, no. 6, pp. 862–868, 2017.

[5] C. D. Hunt, *Sintering in Ceramics and Solid Oxide Fuel Cells*. PhD thesis, Montana State University, 2017.

[6] C. Hunt, M. Zachariasen, D. Driscoll, S. Sofie, and R. Walker, "Degradation rate quantification of solid oxide fuel cell performance with and without Al2TiO5 addition," *International Journal of Hydrogen Energy*, vol. 43, no. 32, pp. 15531–15536, 2018.

[7] J. Kent, "FABRICATION AND ASSESSMENT OF ANODE SUPPORTED SOFCS," Master's thesis, Montana State University, 2019.

[8] M. M. Welander, M. S. Zachariasen, C. D. Hunt, S. W. Sofie, and R. A. Walker, "Operando Studies of Redox Resilience in ALT Enhanced NiO-YSZ SOFC Anodes," *Journal of The Electrochemical Society*, vol. 165, no. 3, pp. F152–F157, 2018.

[9] M. M. Welander, M. S. Zachariasen, S. W. Sofie, and R. A. Walker, "Mitigating Carbon Formation with Al ₂ TiO ₅ Enhanced Solid Oxide Fuel Cell Anodes," *The Journal of Physical Chemistry C*, p. acs.jpcc.9b00964, 2019.

[10] W. R. Grove, "On a new voltaic combination," *London and Edinburgh Philosophical Magazine and Journal of Science*, vol. 13, pp. 430,431, 1838.

[11] W. R. Grove, "On voltaic series and combination of gases by platinum," *London and Edinburgh Philosophical Magazine and Journal of Science*, vol. 14, pp. 127–130, 1839.

[12] W. R. Grove, "On the voltaic polarization of certain solid and fluid substances," *London and Edinburgh Philosophical Magazine and Journal of Science*, vol. 14, pp. 43–45, 1839.

[13] W. R. Grove, "On a gaseous voltaic battery," *London and Edinburgh Philosophical Magazine and Journal of Science*, vol. 21, pp. 417–420, 1842.

[14] A. B. Stambouli and E. Traversa, "Solid oxide fuel cells (SOFCs): A review of an environmentally clean and efficient source of energy," *Renewable and Sustainable Energy Reviews*, vol. 6, no. 5, pp. 433–455, 2002.

[15] "Fuel cells: Solid oxide fuel cells." website, 2004.

[16] G. F. McLean, T. Niet, S. Prince-Richard, and N. Djilali, "An assessment of alkaline fuel cell technology," in *Fuel Cell Compendium*, pp. 117–145, Elsevier, 2005.

[17] N. Sammes, R. Bove, and K. Stahl, "An assessment of alkaline fuel cell technology," in *Fuel Cell Compendium*, pp. 155–165, Elsevier, 2005.

[18] S. Romano and J. T. Larkins, "Georgetown university fuel cell transit bus program," *Fuel Cells*, vol. 3, pp. 128–132, 2003.

[19] A. L. Dicks, "Molten carbonate fuel cells," in *Fuel Cell Compendium*, pp. 147–153, Elsevier, 2005.

[20] A. Baldan, "Progress in Ostwald ripening theories and their applications in nickel-base super alloys," *Journal of Materials Science*, vol. 37, pp. 2379–2405, 2002.

[21] M. Rikukawa and K. Sanui, "Proton-conducting polymer electrolyte membranes based on hydrocarbon polymers," in *Fuel Cell Compendium*, pp. 375–410, Elsevier, 2005.

[22] S. Park, J. W. Lee, and B. N. Popov, "A review of gas diffusion layer in PEM fuel cells: Materials and designs," *International Journal of Hydrogen Energy*, vol. 37, no. 7, pp. 5850–5865, 2012.

[23] J. Wu, X. Z. Yuan, J. J. Martin, H. Wang, J. Zhang, J. Shen, S. Wu, and W. Merida, "A review of PEM fuel cell durability: Degradation mechanisms and mitigation strategies," *Journal of Power Sources*, vol. 184, no. 1, pp. 104–119, 2008.

[24] S. Litster and G. Mclean, "Pem fuel cell electrodes," in *Fuel Cell Compendium*, pp. 443–463, Elsevier, 2005.

[25] S. Park, J. W. Lee, and B. N. Popov, "Effect of PTFE content in microporous layer on water management in PEM fuel cells," *Journal of Power Sources*, vol. 177, no. 2, pp. 457–463, 2008.

[26] S. Latorrata, P. Gallo Stampino, C. Cristiani, and G. Dotelli, "Novel superhydrophobic microporous layers for enhanced performance and efficient water management in PEM fuel cells," *International Journal of Hydrogen Energy*, vol. 39, no. 10, pp. 5350–5357, 2014.

[27] C. Spiegel, "An introduction to fuel cells," in *PEM Fuel Cell Modeling and Simulation Using Matlab*, pp. 1–14, Elsevier, 2008.

[28] J. W. Fergus, "Oxide anode Materials for solid oxide fuel cells," *Solid State Ionics*, vol. 177, pp. 1529–1541, 2006.

[29] R. Walker, ed., *MTSI 502 - Advanced Material Science: Section 3 - Electrochemistry*, Montana State University, 2019.

[30] H. Gerischer, "Principles of electrochemistry," in *The CRC Handbook of Solid State Electrochemistry*, pp. 9–72, CRC Press, 1997.

[31] C. Sun and U. Stimming, "Recent anode advances in solid oxide fuel cells," *Journal of Power Sources*, vol. 171, pp. 247–260, 2007.

[32] N. Jaiswal, K. Tanwar, R. Suman, D. Kumar, S. Uppadhya, and O. Parkash, "A brief review on ceria based solid electrolytes for solid oxide fuel cells," *Journal of Alloys and Compounds*, vol. 781, pp. 984–1005, 2019.

[33] M. C. Williams, J. P. Strakey, and S. C. Singhal, "U.S. distributed generation fuel cell program," *Journal of Power Sources*, vol. 131, no. 1-2, pp. 79–85, 2004.

[34] A. Hamedami, Hodi, *Investigation of deposition parameters in ultrasonic spray pyrolysis for fabrication of solid oxide fuel cell cathode*. PhD thesis, Georgia Insitute of Technology, 2019.

[35] D. Ivers-tiffee, Ellen; Weber, Andre; Herbstritt, "Materials and technologies for SOFC components," *Journal of the European Ceramics Society*, vol. 21, pp. 1–5, 2001.

[36] I. Sreedhar, B. Agarwal, P. Goyal, and S. A. Singh, "Recent advances in material and performance aspects of solid oxide fuel cells," *Journal of Electroanalytical Chemistry*, vol. 848, p. 113315, 2019.

[37] F. S. da Silva and T. M. de Souza, "Novel materials for solid oxide fuel cell technologies: A literature review," *International Journal of Hydrogen Energy*, vol. 42, no. 41, pp. 26020–26036, 2017.

[38] R. H. Nielson and G. Wilfing, "Zirconium and zirconium compounds," in *Ullmann's Encyclopedia of Industrial Chemistry*, Wiley, 2010.

[39] C. Goulart and D. de Souza, "Critical analysis of aqueous tape casting, sintering, and characterization of planar Yttria-Stabilized Zirconia electrolytes for SOFC," *International Journal of Applied Ceramic Technology*, vol. 14, no. 3, pp. 413–423, 2017.

[40] C. Xia and M. Liu, "Microstructures, conductivities, and electrochemical properties of ce0.9gd0.1o2 and gdcni anodes for low-temperature sofcs," *Solid State Ionics*, vol. 153, 2002.

[41] B. Shri Prakash, S. Senthil Kumar, and S. T. Aruna, "Properties and development of Ni/YSZ as an anode material in solid oxide fuel cell: A review," *Renewable and Sustainable Energy Reviews*, vol. 36, pp. 149–179, 2014.

[42] N. Mary, C. Augustine, J. Shiney, and S. Heartson, "Dynamic modeling and fuzzy control for solid oxide fuel cell (sofc)," *International Journal of Advanced Research in Electrical, Electronics and Instrumentation Engineering*, vol. 5, June 2016.

[43] R. J. Gorte, S. Park, J. M. Vohs, and C. Wang, "Anodes for direct oxidation of dry hydrocarbons in a solid-oxide fuel cell," *Advanced Materials*, vol. 12, no. 19, pp. 1465–1469, 2000.

[44] P. Hofmann, A. Schweiger, L. Fryda, K. D. Panopoulos, U. Hohenwarter, J. D. Bentzen, J. P. Ouweltjes, J. Ahrenfeldt, U. Henriksen, and E. Kakaras, "High temperature electrolyte supported Ni-GDC/YSZ/LSM SOFC operation on two-stage Viking gasifier product gas," *Journal of Power Sources*, vol. 173, no. 1, pp. 357–366, 2007.

[45] T. Ishihara, T. Shibayama, H. Nishiguchi, and Y. Takita, "NickelGd-doped CeO2 cermet anode for intermediate temperature operating solid oxide fuel cells using LaGaO3-based perovskite electrolyte," *Solid State Ionics*, vol. 132, no. 3, pp. 209–216, 2000.

[46] V. A. Rojek-Wöckner, A. K. Opitz, M. Brandner, J. Mathé, and M. Bram, "A novel Ni/ceria-based anode for metal-supported solid oxide fuel cells," *Journal of Power Sources*, vol. 328, pp. 65–74, 2016.

[47] W. C. Chueh, Y. Hao, W. Jung, and S. M. Haile, "High electrochemical activity of the oxide phase in model ceria-Pt and ceria-Ni composite anodes," *Nature Materials*, vol. 11, no. 2, pp. 155–161, 2012.

[48] R. V. Wandekar, M. Ali (Basu), B. N. Wani, and S. R. Bharadwaj, "Physicochemical studies of NiO-GDC composites," *Materials Chemistry and Physics*, vol. 99, no. 2-3, pp. 289–294, 2006.

[49] T. Dey, D. Singdeo, J. Deshpande, and P. C. Ghosh, "Structural analysis of solid oxide fuel cell under externally applied compressive pressure," *Energy Procedia*, vol. 54, pp. 789–795, 2014.

[50] N. E. Dowling, S. L. Kampe, and M. V. Kral, "Fracture of cracked members," in *Mechanical Behavior of Materials: Engineering Methods for Deformation, Fracture, and Fatigue*, pp. 276–343, Pearson, 2019.

[51] H. Ashby, Michael Shercliff and D. Cebon, "Fracture and fracture toughness," in *Materials Engineering, Science, Processing and Design*, pp. 197–224, Elsevier, 2014.

[52] ASTM, *Standard Practice for Reporting Uniaxial Strength Data and Estimating Weibull Distribution Parameters for Advanced Ceramics*.

[53] ASTM, *Standard Test Method for Flexural Strength of Advanced Ceramics at Ambient Temperature*.

[54] G. D. Quinn, "Fracture Toughness of Ceramics by the Vickers Indentation Crack Length Method: A Critical Review," *Mechanical Properties and Performance of Engineering Ceramics II: Ceramic Engineering and Science Proceedings*, vol. 27, no. 2, pp. 45–62, 2008.

[55] M. S. Khan, S. B. Lee, R. H. Song, J. W. Lee, T. H. Lim, and S. J. Park, "Fundamental mechanisms involved in the degradation of nickel-yttria stabilized zirconia (Ni-YSZ) anode during solid oxide fuel cells operation: A review," *Ceramics International*, vol. 42, no. 1, pp. 35–48, 2015.

[56] D. Kennouche, Y. C. K. Chen-Wiegart, K. J. Yakal-Kremski, J. Wang, J. W. Gibbs, P. W. Voorhees, and S. A. Barnett, "Observing the microstructural evolution of Ni-Yttria-stabilized zirconia solid oxide fuel cell anodes," *Acta Materialia*, vol. 103, pp. 204–210, 2016.

[57] D. Simwonis, F. Tietz, and D. Stover, "Nickel coarsening in annealed Ni / 8YSZ anode substrates for solid oxide fuel cells," *Solid State Ionics*, vol. 132, pp. 241–251, 2000.

[58] A. Lussier, S. Sofie, J. Dvorak, and Y. U. Idzerda, "Mechanism for SOFC anode degradation from hydrogen sulfide exposure," *International Journal of Hydrogen Energy*, vol. 33, no. 14, pp. 3945–3951, 2008.

[59] F. Wang, W. Wang, R. Ran, M. O. Tade, and Z. Shao, "Aluminum oxide as a dual-functional modifier of Ni-based anodes of solid oxide fuel cells for operation on simulated biogas," *Journal of Power Sources*, vol. 268, pp. 787–793, 2014.

[60] D. D. Driscoll, ed., *Ceramic-Metal Joining on the Nanoscale: Engineered Interfaces for Robust Thermal Performance*, Montana State University, 2012.

[61] A. Morales-Marín, J. L. Ayastuy, U. Iriarte-Velasco, and M. A. Gutiérrez-Ortiz, "Nickel aluminate spinel-derived catalysts for the aqueous phase reforming of glycerol: Effect of reduction temperature," *Applied Catalysis B: Environmental*, vol. 244, no. July 2018, pp. 931–945, 2019.

[62] A. J. Reynoso, J. L. Ayastuy, U. Iriarte-Velasco, and M. A. Gutiérrez-Ortiz, "Cobalt aluminate spinel-derived catalysts for glycerol aqueous phase reforming," *Applied Catalysis B: Environmental*, vol. 239, no. July, pp. 86–101, 2018.

[63] Y. J. Wong, M. K. Koh, M. Khavarian, and A. R. Mohamed, "Investigation on cobalt aluminate as an oxygen carrier catalyst for dry reforming of methane," *International Journal of Hydrogen Energy*, 2017.

[64] I. Mindru, D. Gingasu, L. Patron, G. Marinescu, J. M. Calderon-Moreno, S. Preda, O. Oprea, and S. Nita, "Copper aluminate spinel by soft chemical routes," *Ceramics International*, vol. 42, no. 1partA, pp. 154–164, 2016.

[65] C. Ragupathi, J. J. Vijaya, L. J. Kennedy, and M. Bououdina, "Nanostructured copper aluminate spinels: Synthesis, structural, optical, magnetic, and catalytic properties," *Materials Science in Semiconductor Processing*, vol. 24, no. 1, pp. 146–156, 2014.

[66] A. Seko, F. Oba, and I. Tanaka, "Classification of spinel structures based on first-principles cluster expansion analysis," *Physical Review B - Condensed Matter and Materials Physics*, vol. 81, no. 5, pp. 1–7, 2010.

[67] Y. Chen, L. Yang, F. Ren, and K. An, "Visualizing the structural evolution of LSM/xYSZ composite cathodes for SOFC by in-situ neutron diffraction," *Scientific Reports*, vol. 4, 2014.

[68] P. Cousin and R. A. Ross, "Preparation of mixed oxides: a review," *Materials Science and Engineering A*, vol. 130, no. 1, pp. 119–125, 1990.

[69] L. Maoqiang, "Principles and synthesis of ceramic powder by means of wet chemical method," *Journal of the Chinese Ceramic Society*, vol. 1, 1994.

[70] D. J. Taylor, P. F. Fleig, and R. A. Page, "Characterization of nickel titanate synthesized by sol-gel processing," *Thin Solid Films*, vol. 408, no. 1-2, pp. 104–110, 2002.

[71] T. Guo, L. Zhang, X. Song, X. Dong, M. M. Shirolkar, M. Wang, M. Li, and H. Wang, "Influences of Gd2Ti2O7sintering aid on the densification, ionic conductivity and thermal expansion of Gd0.1Ce0.9O1.95electrolyte for solid oxide fuel cells," *Journal of Power Sources*, vol. 262, pp. 239–244, 2014.

[72] C. Heremans and H. Tuller, "Stability and mixed ionic electronic conduction in Gd2(Ti1-xMox)2O7 under anodic conditions," *Solid State Ionics*, vol. 94, pp. 75–83, 1997.

[73] L. Kong, D. J. Gregg, E. R. Vance, I. Karatchevtseva, G. R. Lumpkin, M. G. Blackford, R. Holmes, M. Jovanovic, and G. Triani, "Preparation of cerium titanate brannerite by solution combustion, and phase transformation during heat treatment," *Journal of the European Ceramic Society*, vol. 37, no. 5, pp. 2179–2187, 2017.

[74] W. T. Fu and D. J. Ijdo, "The structure of CeAlO3by Rietveld refinement of X-ray powder diffraction data," *Journal of Solid State Chemistry*, vol. 177, no. 9, pp. 2973–2976, 2004.

[75] Y. He, Y. Cao, H. Liao, and J. an Wang, "Preparation of porous cobalt aluminate and its chromogenic mechanism," *Powder Technology*, vol. 324, no. 3, pp. 95–101, 2018.

[76] D. Xiong, X. Zeng, W. Zhang, H. Wang, X. Zhao, W. Chen, and Y. B. Cheng, "Synthesis and characterization of CuAlO2 and AgAlO2 delafossite oxides through low-temperature hydrothermal methods," *Inorganic Chemistry*, vol. 53, no. 8, pp. 4106–4116, 2014.

[77] H. Kawazoe, M. Yasukawa, H. Hyodo, M. Kurita, H. Yanagi, and H. Hosono, "P-type electrical conduction in transparent thin films of cualo2," *Nature*, vol. 389, 1997.

[78] J. I. Goldstein, D. E. Newbury, P. Echlin, D. C. Joy, C. Lyman, E. Lifshin, L. Sawyer, and J. Micheal, "Electron beam-specimen interactions," in *Scanning Electron Microscopy and X-ray Microanalysis*, pp. 61–97, Springer, 2007.